AALBORG UNIVERSITY ESBJERG

Race Car Aerodynamic Design and Optimization via CFD and the Discrete Adjoint Method

M.Sc. Thesis

Process Engineering and Combustion Technology

PECT10-4-F18

7/6-18

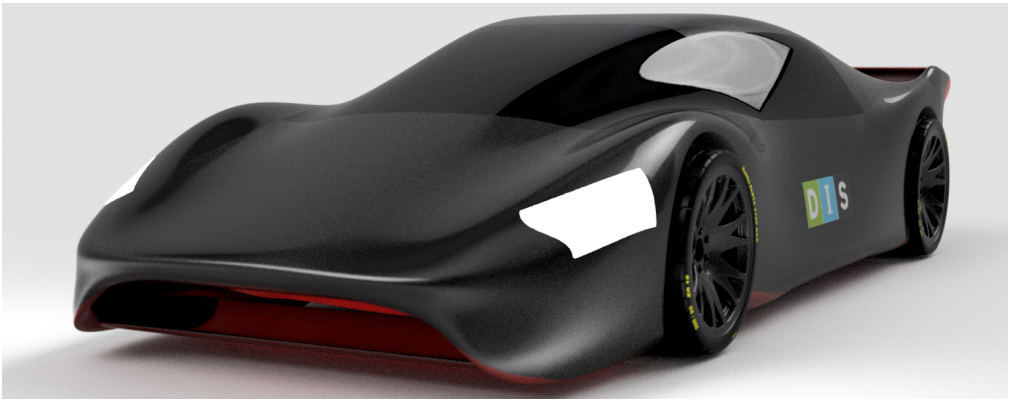

AALBORG UNIVERSITY
STUDENT REPORT

DIS innovative engineering

Institute of Energy Technology
Niels Bohrs Vej 8
DK-6700 Esbjerg
www.en.esbjerg.aau.dk

Title:
Race Car Aerodynamic Design and Optimization via CFD and the Discrete Adjoint Method

Project Group:
PECT10-4-F18

Members:
Christian Bach Rasmussen
cbra13@student.aau.dk

Lasse Mose Lund
lml12@student.aau.dk

AAU Supervisor:
Matthias Mandø
mma@et.aau.dk

DIS A/S Supervisor:
Emil Kennemann Christensen
ekc@d-i-s.dk

No. of Pages: 89

Completed: 07-06-2018

Abstract:

The DIS1 race car is a serial-hybrid electric race car. This study is aimed at designing a bodykit for this. The main requirements are the generation of 1200kgf of downforce at 280km hr^{-1}, while maintaining a drag, low enough for 280bhp to overcome at 280km hr^{-1}.
The design was analyzed with CFD in Ansys Fluent v. 19.0. An initial design was modified through two preliminary design iterations. The CFD model for these used the Realizable k-ϵ model with a tetrahedral mesh of approximately 6.9 million cells.
The initial design was improved with 173.98kgf of downforce through the preliminary design iterations. The power required to overcome the drag force was lowered 23.13bhp.
Fluid topology optimization via the discrete adjoint method was then applied. This optimization focused on the generation of downforce.
The fluid topology optimization further improved the downforce with 67.84kgf, while lowering the drag force with a force equivalent of 44.07bhp.
The final design is not able to generate the desired amount of downforce. The bodykit has a positive lift of 162.69kgf. The force to overcome the drag is well within the requirement, at 120.48bhp. A bodykit generating the desired amount of downforce would require fewer constraints to the development.

1. Executive Summary

Dansk Ingeniør Service A/S has set an ambitious goal to build a race car called DIS1. A prototype chassis has already been designed and constructed, taking the mechanical considerations into account. However, the design has not been considered from an aerodynamic point of view yet.
The purpose of this study was to take the aerodynamics into account. This meant, that a proposed bodykit for the DIS1 race car should be designed. The process initially included a literature study in order to identify the important aerodynamic considerations. Additionally, the specified performance goals were set in context with high performance cars from premium car manufacturers.
The design was developed through *Computational Fluid Dynamics* (CFD). Via CFD modeling, the performance of the bodykit could be evaluated. Lastly, the design was optimized via the discrete adjoint method. This enables small effective geometry changes to specific parts of the body.

Fluid topology optimization via the adjoint method has previously shown good results in improving vehicle aerodynamics. However, studies describing the development of the first bluff body design of the car was not found. This study was therefore made to act as a baseline for what considerations to be aware of. Additionally, it shows how CFD tools can be utilized to accelerate the design process compared to manual modifications.

The preliminary iterations were able to improve the performance with -173.98kgf of downforce at 280km hr^{-1} (9.80665N = 1kgf). Additionally, the drag force was reduced with a force corresponding to 23.13bhp at 280km hr^{-1}. These improvements were realized by resizing the front wing, adding a rear wing, and adjusting the diffuser.
The fluid topology optimization focused on the bodywork performance. This excluded modifications to the front and rear wing, as these were already based on high performance airfoils. The optimization used the discrete adjoint method and an automatic geometry morphing tool.
The geometry change is illustrated in Fig. 1.1a. The design before the adjoint optimization is marked with gray for the right half. The left half is marked with red to better visualize where material has been removed. Material has been added in the areas marked with brown.

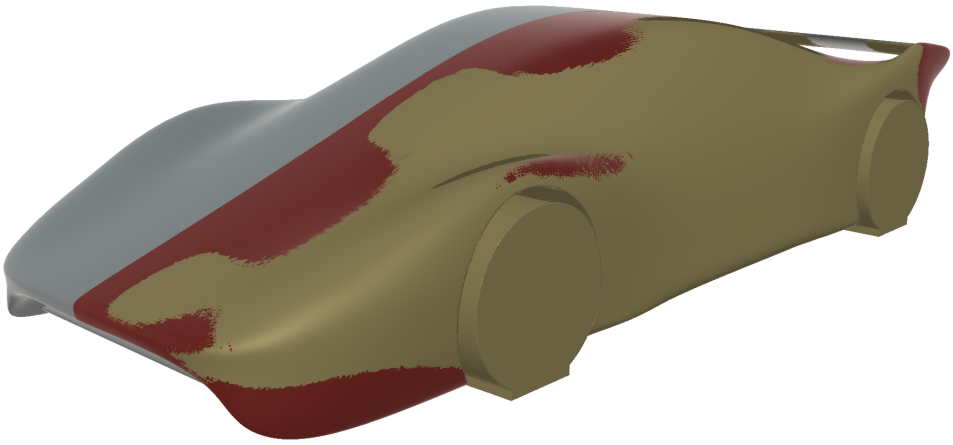

(a) Geometry change after fluid topology optimization.

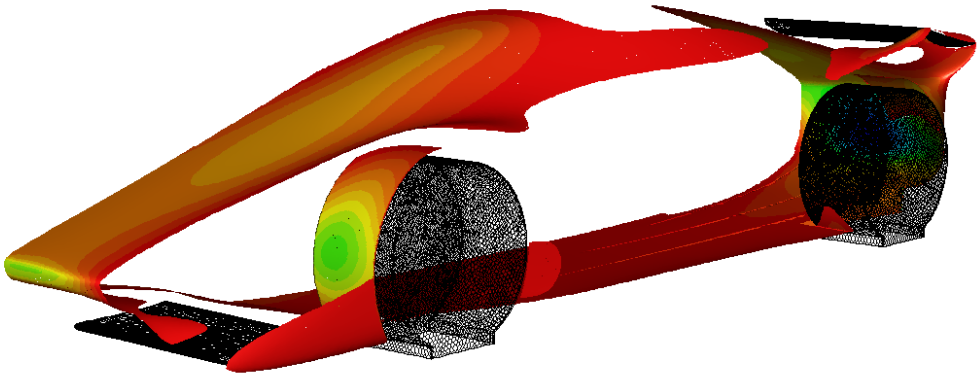

(b) Regions where material should be removed.

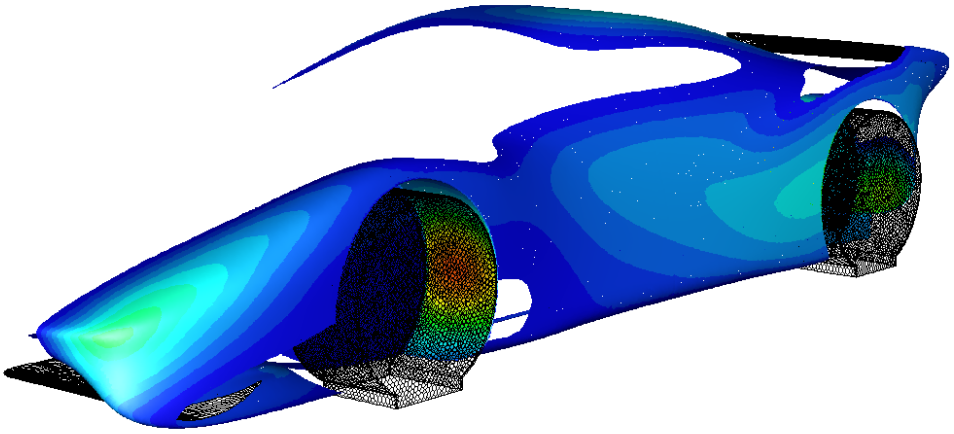

(c) Regions where material should be added.

Figure 1.1

The geometry modifications followed the calculated optimal normal displacements in Fig. 1.1b and 1.1c.
Fig. 1.1b shows where the downforce would improve by removal of material. Fig. 1.1c shows where the downforce would improve by adding material.
The optimization was performed over two adjoint cases. These amounted to a performance improvement of -67.84kgf at 280km hr^{-1}. The drag force improved by a force corresponding to -44.07bhp at 280km hr^{-1}. Additional cases would improve this further. However, the improvement found from each additional case decreases rapidly. E.g., the first adjoint case had an improvement of -43.03kgf, where the second adjoint case had an improvement of -24.81kgf.

The final bodykit generates a positive lift of 162.69kgf at 280km hr^{-1}. The drag generated can be overcome by 120.48bhp. The target of -1200kgf of downforce was therefore not met, while the drag force is significantly lower than the target of <280bhp. However, the current amount of drag leaves great potential of increasing the downforce before approaching the desired drag limit.
The streamlines across the final design are illustrated in Fig. 1.2.

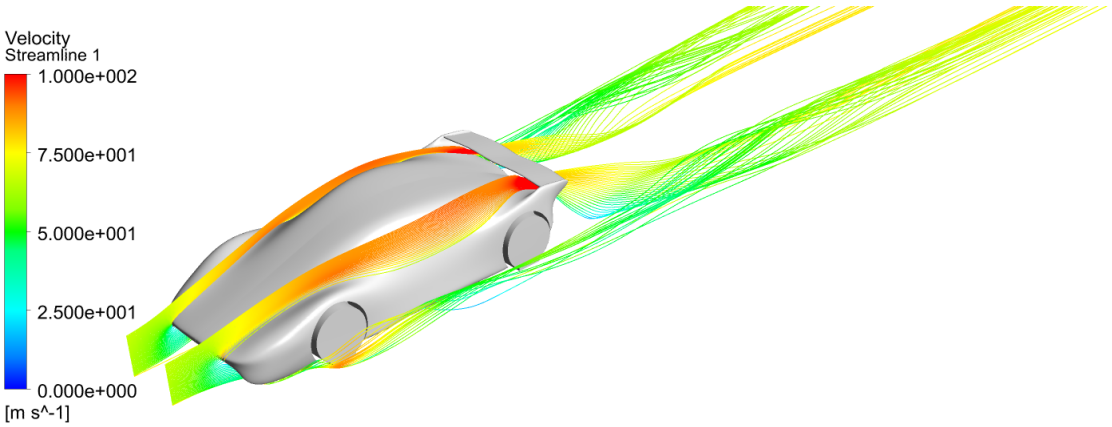

Figure 1.2: Streamlines over the final design.

Fig. 1.2 shows good flow attachment which is desired from a drag point of view.

The design choices have been constrained by the existing chassis, where it is currently difficult to further improve the aerodynamic performance. However, aerodynamic improvements can be easily implemented to this design. Although they do require modifications to the current chassis and more time to develop additional bodykit details.

For future design modifications, it would be desirable to alter the current chassis. This should be based on the knowledge gathered through the preliminary design study. E.g., the chassis should be modified to enable an earlier diffuser expansion. The point of expansion should be close to the center of gravity as the highest amount of downforce is generated here. This affects the downforce balance of the car greatly. Additional clearance between the road and chassis would also make it possible to create a larger venturi

effect. Furthermore, internal ducts for radiators, batteries, and the combustion engine should be considered.
Another interesting aspect to investigate, would be to implement multiple observable constraints. I.e., simultaneous lift and drag optimization, and/or weighting options for the adjoint optimization. This could in theory be used to balance the aerodynamic load of the car.

The current study provides a good reference for the initial considerations for race car body designs. It also illustrates the usefulness of the current commercial code implemented in *Ansys Fluent v. 19.0*. However, it should be noted, that the modeled drag and lift performance are only estimates. The study has been limited by computational resources, which has lead to compromises in terms of overall model resolution. The extend of how this affects the reported performance parameters has not been investigated. Further studies would need additional computational resources to better resolve possible flow detachment and reattachment zones on the surface. In addition, as more details are added to the design, larger meshes will be required.

It is concluded, that the adjoint optimization shows great potential for optimizing various fluid cases. Its ability to handle complex geometries, at relatively low computational costs, makes it ideal for the last steps of a bodykit design. Furthermore, the diverse possibilities in choice of observables makes it possible to take many different aspects into account simultaneously, e.g. reduction of vorticity strength, and a uniform flow condition for the wake etc.

Contents

Nomenclature

A	Area	m^2
C	Coefficient	–
C_r	Cross section	m^2
c_p	Specific heat capacity	J $kg^{-1}K^{-1}$
D	Diameter	m
d	Half of undertray width	m
F	Force	N
f	Friction factor	–
g	Gravitational acceleration	m s^{-2}
h	Convective heat transfer coefficient	W $m^{-2}K^{-1}$
h_r	Car ride height	m
k	Thermal conductivity	W $m^{-1}K^{-1}$
L	Length	m
m	Mass	kg
n_{tubes}	Number of tubes	–
Nu	Nusselt number	–
P	Pressure	Pa
P_o	Power	W
Pr	Prandtl number	–
Q	Heat transfer	J
Re	Reynolds number	–
r	Radius	m
T	Temperature	K or °C
t	Time	s
u_t	Frictional velocity	m s^{-1}
v	Velocity	m s^{-1}
y	Cell height	m
y^+	Non-dimensional wall distance	–

Special signs

Δ	Finite difference	–
ϵ	Emissivity constant	–
λ	Adjoint variable	–
ϕ	Design variable	–
ρ	Density	kg m^{-3}
μ	Dynamic viscosity	kg $m^{-1}s^{-1}$
ν	Kinematic viscosity	m^2s^{-1}
θ	Diffuser angle	$\circ$
τ	Shear stress	N m^{-2}
∂	Partial derivative	–

Superscripts

$\cdot$	Rate
$-$	Average

Subscripts

c	Cross sectional
co	Conical
D	Drag
diff	Diffuser
etd	Extreme temperature difference
F	Force
L	Lift
lat	Lateral
normal,avail	Available in normal direction
normal,req	Required in normal direction
s	Surface
w	Wall
∞	Free stream

2. Introduction

The world of high performance cars is fast-paced. Both in terms of the cars, and the innovations enabling their increasingly high performance. One of the fields important to controlling the cars is the aerodynamics. Good aerodynamics ensure, that the wheels are able to transfer the power to the road. Furthermore, it makes it possible to corner faster.
Having the fastest car has been a prestige project for several major premium car manufactures for years. *Dansk Ingeniør Service A/S* (DIS A/S) is no such car manufacturer, but an ambitious goal has still been set to build the DIS1 race car. The DIS1 project aims to achieve the fastest lap time on both the Top Gear test track and the Nürnburgring. Additionally, two time goals have been set. These are listed in Table 2.1, together with the current fastest lap times and record holders on the two race tracks.

Table 2.1: Specified time goals of the DIS1 race car [1].

	Record Holder	Current Record	Goal
0-100km h^{-1}	Grimsel, AMZ Racing	1.513s [2]	<2.0s
0-200-0km h^{-1}	-	-	<10.0s
Nürnburgring	Porsche 911 GT2 RS	6:47.3 [3]	<6:47.3
Top Gear test track	Pagani Huayra	1:13.8 [4]	<1:13.8

These four goals are all very ambitious, and they are therefore also most likely first possible to achieve at the very end of the combined DIS1 project. The participation at the first Sportscar Event in 2020 is the current deadline.
This study is focused on the design of an aerodynamic bodykit. The design process is carried out in different phases. Initially, several studies and premium cars have been investigated. This should give insight into the achievability of the specified goals. A rough bodykit is designed from common knowledge about aerodynamics. This design is then analyzed and modified via *Computational Fluid Dynamics* (CFD) in Ansys Fluent v. 19.0. After addressing the most obvious aerodynamic disadvantages the Ansys Adjoint Solver is utilized. This uses the discrete adjoint method to identify areas on the geometry, where changes should be made. A morphing tool is then able to modify the geometry in the most beneficial way. This modification should be constrained by design choices and goals specified by DIS Race Lab.

The study is structured in accordance with the guidelines for the completion of the master of science education of Process Technology and Combustion Engineering [5]. The study was carried out under the supervision of associate professor Matthias Mandø, from the Department of Energy Technology at Aalborg University Esbjerg.
Additionally, an external party has been involved. The study has been carried out at DIS A/S with company supervisor Emil Kennemann Christensen. Emil Kennemann Christensen is a part of DIS Race Lab, which is responsible of the development of DIS1.

About Dansk Ingeniør Service A/S

DIS A/S is an engineering consultancy company with 18 worldwide offices and around 500 engineers and project managers. The company focuses on engineering and development, with core competences in the fields of; mechanical, hardware, software, electrical, and automation engineering, as well as project management. DIS A/S is one of the frontrunners of the Industry 4.0 integration in Denmark and has been awarded as the best Gazelle company 6 times. [6]
DIS Race Lab is a volunteer project primarily composed of engineers, working on the project in their spare time. The project is financially supported by the company.

Acknowledgements

The authors would like to thank DIS A/S and DIS Race Lab for the possibility to cooperate on this study. Special recognition is given to Emil Kennemann Christensen for his help and guidance from the initial steps of the study to its completion.
Great appreciation is also given to supervisor Matthias Mandø for the possibility of using his workstation for the simulations. This both improved model resolution and decreased computational time significantly.

2.1. The DIS1 Project

Designing a race car is a multidisciplinary project and several different fields of engineering therefore have to cooperate. A chassis can therefore not be designed solely based on mechanical considerations, if good aerodynamic properties are desired. However, this is unfortunately the case for the chassis provided at the start of the study. Some modifications will therefore most likely be required. Additionally, components such as batteries, combustion engine, generators, and etc. requires cooling, which should also be considered when developing the bodykit.

The DIS1 race car is a serial-hybrid three seater. This number of seats has been chosen, as the car is intended to give multiple people a driving experience to raise money for charity.
The car is fitted with four electric motors, limited to a total output of 900whp (wheel horse power). This means, that the electric motors drives the wheels, while a combustion engine is used to recharge the batteries. The total potential of the electric motors is 1400whp, but this is limited due to the battery capacity. The power is distributed as 280whp and 620whp, with torques of 480Nm and 1000Nm, in the front and the rear, respectively [1]. The battery package is composed of 1000 MELASTA high drain LI-PO battery cells with a total capacity of approximately 20kWh. These are recharged by a 300bhp engine connected to two electric generators. A concept illustration can be seen in Fig. 2.1. This concept was the state of the DIS1 bodykit at the start of this study.
In addition to the overall performance goals in Table 2.1, several bodykit specific requirements have been set. These are listed in Table 2.2.

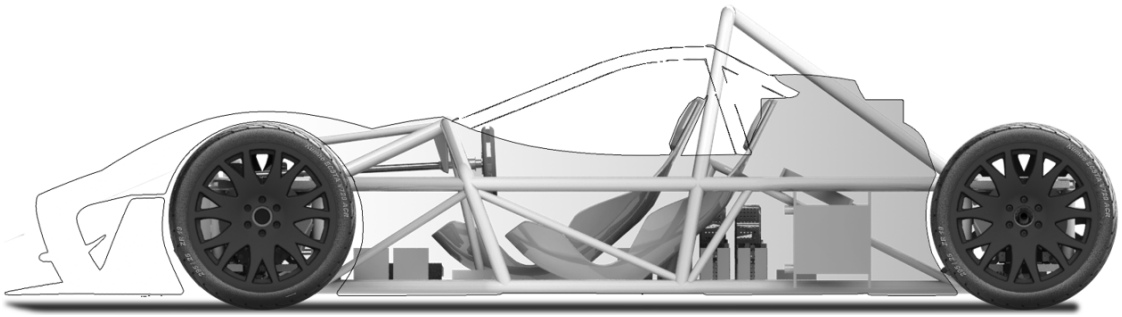

Figure 2.1: Concept drawing of DIS1 [1].

Table 2.2: Bodykit requirements [1].

Lift	-1200kgf at 280km hr^{-1}.
Drag	<280bhp at 280km hr^{-1}.
Clearing	Drive height of 50mm with 20-30mm compression.
Cooling	Brakes, generators, combustion engine, electric motors, converters, and batteries.

In order to satisfy the different cooling demands, the bodykit should have several different channels distributing air inside the vehicle. Additionally, the negative lift, also known as downforce, can not induce too much drag as this would render recharge of the batteries, at top speed, impossible. The top speed is expected to be around 280km hr^{-1}. Since the car is an electric-gasoline hybrid, it will also be required to have an air intake for the combustion engine.

It is not intended to design an open wheel bodykit in the style of Formula 1 (F1) cars. The initial design aim is a bodykit similar in style as premium high performance cars, and cars encountered in e.g. *Danish Touringcar Championship* (DTC) and/or *World Endurance Championship* (WEC) (see Fig. 2.2).

(a) Aston Martin Valkyrie [7]. (b) Audi R18 e-tron quattro [8].

Figure 2.2

2.1.1. Chassis

The chassis has been designed by mechanical engineers from DIS Race Lab to meet certain requirements regarding rigidity and safety. Furthermore, it is designed to fit around the different components. This means, that big changes can be difficult to implement. Furthermore, the three seater configuration makes it difficult to achieve a streamlined design, while also being aesthetically pleasing. Note that the Audi R18 in Fig. 2.2b only incorporates room for 1 driver, and thereby prioritizes race performance.
The chassis is illustrated in Fig. 2.3, with the driver and a passenger illustrated in the seats.

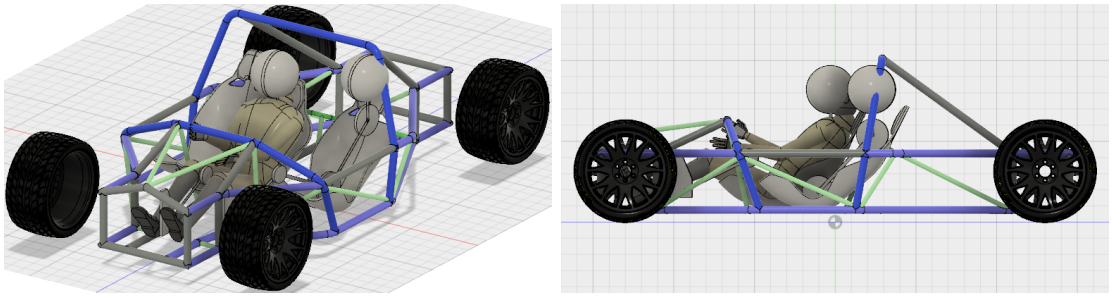

(a) (b)

Figure 2.3: DIS1 initial chassis design [1].

From Fig. 2.3b it is clear, that the car's highest point is located behind the center. This will have an effect on the angle on the rear part of the bodywork. Additionally, the total width of the chassis, with wheels, is 1.95m, where a maximum width of 2m is required. Besides this, the chassis floor is flat and has a road clearing height of 50mm. As this is the desired final road clearing, it excludes development of anything but a flat undertray. A crumple zone extending 0.7m from the front of the chassis is required for safety in the event of a front collision. The front therefore has to extend at least 0.7m out from the front of the chassis.
As Table 2.2 indicates, cooling has to be incorporated. Going into particular details with this is not included in this report. However, conservative estimates are made to give insight into estimated cooling requirements/performance for the radiators, brakes, and combustion engine. The inclusion of ducts is beyond the scope of this study.

2.1.2. Cooling

The components in need of cooling (see Table 2.2) are illustrated in Fig. 2.4. Not all components are marked with arrows, e.g. the brakes and electric motors are only marked in one end, even though they are present on all four wheels.

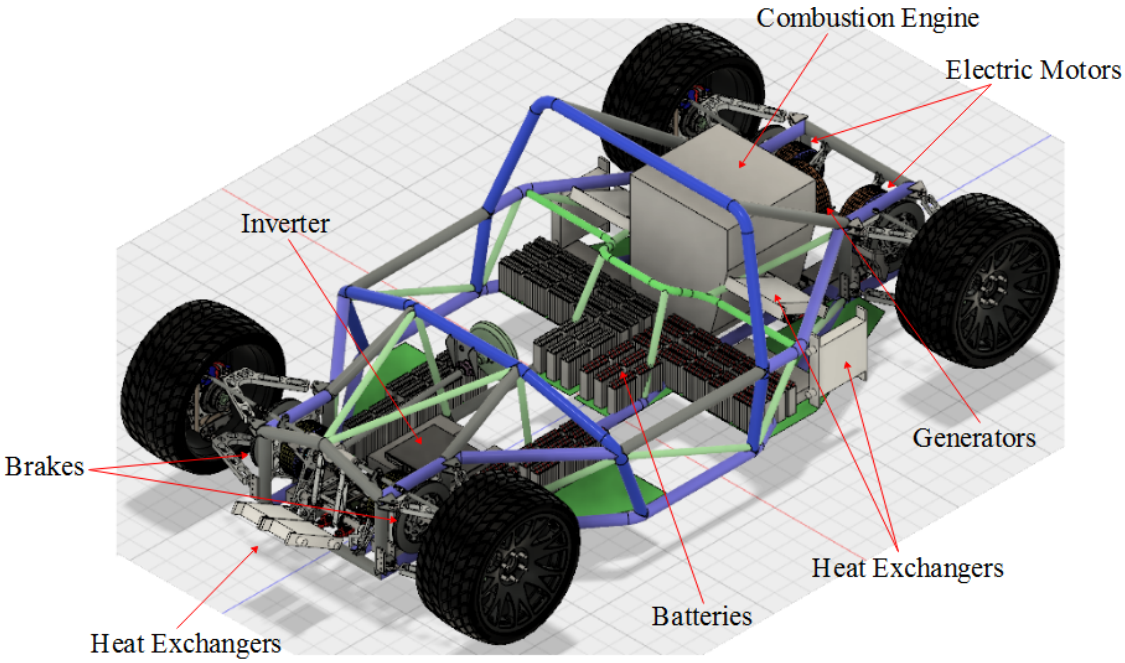

Figure 2.4: Components in need of cooling [1].

The components not marked by the arrows in Fig. 2.4 are; two inverters, two brakes, two electric motors and two heat exchangers. The two unmarked inverters are not visible in Fig. 2.4, as they are placed behind the combustion engine. All other unmarked components are visible.

3. Review of Race Car Aerodynamics

The purpose of this review is to gather multiple studies conducted on the subject of race car aerodynamics. Furthermore, it includes an investigation of the relevant techniques used to optimize and analyze the bodykit.

The aerodynamics of race cars can be compared to the aerodynamics of an airplane. Though opposite, since the purpose here is not to generate lift, but downforce. This downforce creates stability on the front and rear axles during high speed turns without increasing the overall weight of the vehicle.
Katz et al. (1995) [9] notes the two other main force considerations, besides downforce, that must be taken into account. The first force is the induced drag. This has a slowing effect and is therefore sought reduced by streamlining of the car bodywork. The second force, is the side force, normally induced by winds. However, this effect on the aerodynamic load is usually very low.
The overall design methodology for considering these factors is not very well established. Hucho (2003) [10] points out, that it usually starts with a low drag body in a wind tunnel. This is then developed into a car shape in a collaboration between engineers and designers. Therefore, no empirical approach exists, as the shape is a function of style, safety, comfort, handling, and performance. Lastly, it is also pointed out by Hucho (2003) [10], that much of the aerodynamic design of the car is to limit or fine tune the flow. This is normally done through experimentation or accelerated by using computer aided tools.
CFD can be used to both evaluate and optimize the aerodynamic performance of race cars. This can be done both manually and partly automatically.
Manually optimizing the design implies, that the design is analyzed via CFD and the results are used to make modifications. Such an approach often works for the major modifications.
The partly automatic optimization works by analyzing via CFD and then modifying the design by algorithms. This makes it possible to make modifications to smaller details than the manual approach.
The adjoint method is such a partly automatic method. This method reformulates the aerodynamic behavior into an expression, which is able to calculate the derivatives of desired parameters. This in turn means, that it is able to evaluate where a geometry change will have the largest effect. The second step is a geometry morphing, which can make the most effective changes to the geometry. Thus, changing the geometry where the derivative of the desired parameter is greatest. Using this method has a high potential for optimizing a certain geometry with only minor geometric changes [11].

In a study conducted by Karpouzas et al. (2016) [12] on the adjoint optimization of vehicle external aerodynamics, the authors implemented an adjoint optimization algorithm. This was done in an open source CFD solver with steady state *Reynolds Averaged Navier-Stokes* (RANS) solving. The algorithm successfully reduced the drag by 8% for an aerodynamic car model body. Additionally, a 0.2% improvement for the rear spoiler, and 7% for the side mirrors were achieved. The study also reduced the pressure loss by 60% in an s-bend duct ventilation system with this method. However, as the authors point out, the changes to the car body are not directly apparent when comparing the original geometry to the morphed one. The modifications are of a very small scale, which can have a restrictive effect during manufacturing.
A case study on the DrivAer Fastback by Frank et al. (2013) [13] performed car drag optimization via the adjoint method in Ansys Fluent. The study investigated four cases; 50km hr^{-1}, 70km hr^{-1}, 100km hr^{-1}, and 120km hr^{-1}. The drag coefficient was reduced from 0.259 to 0.251 for the slowest case, and from 0.256 to 0.247 for the fastest case. The improvements for all four cases were in the interval between 3.9% and 6.6% drag reduction. Only the rear corner of the car was allowed to be modified. A total of seven adjoint cases were used for all four cases and the simulated results matched with experimental data.
A study by Othmer et al. (2014) [14] used an adjoint solver developed for OpenFOAM to investigate the external aerodynamics of the Volkswagen XL1 concept car. This model found four areas, where design modifications could be made, in order to decrease the overall drag. The study confirmed, that all four sensitivity signs, given by the adjoint solver, resulted in decreased drag. Optimizing the spoiler shape reduced the drag by 2%, while the lift was decreased by 30%. The drag reduction is relatively small since the XL1 has already been developed to be very aerodynamic.
Tzanakis (2014) [15] used the Ansys Fluent adjoint solver to optimize the shape of several different air ducts. The minimization parameter was the pressure drop. For one duct the result was a 60% decrease in pressure drop over a total of 15 adjoint cases. Another duct had a 11% decrease over 23 adjoint cases. The geometry morphing was unrestricted between the in- and outlet. A cluster with 120CPUs was available for the study.
Montanelli (2013) [16] performed 2D shape optimization on a LS89 blade for use in turbo machines. This study's objective function was a minimization of the entropy generation rate. It is not concluded how much the objective function is minimized, but an improvement is clear. The study used a mesh of 153,482 cells with a computer with 4 quad-core Intel Xeon Nehalem 2.66GHz processors.

3.1. Review of Desired Bodykit Specifications

It is desired to evaluate whether the desired downforce specifications seem achievable or not. The six cars in Fig. 3.1, the Aston Martin Valkyrie in Fig. 2.2a, and the two current record holders (see Table 2.1) have been chosen as comparisons. All nine cars are high performance sports cars, designed to perform well on the track.

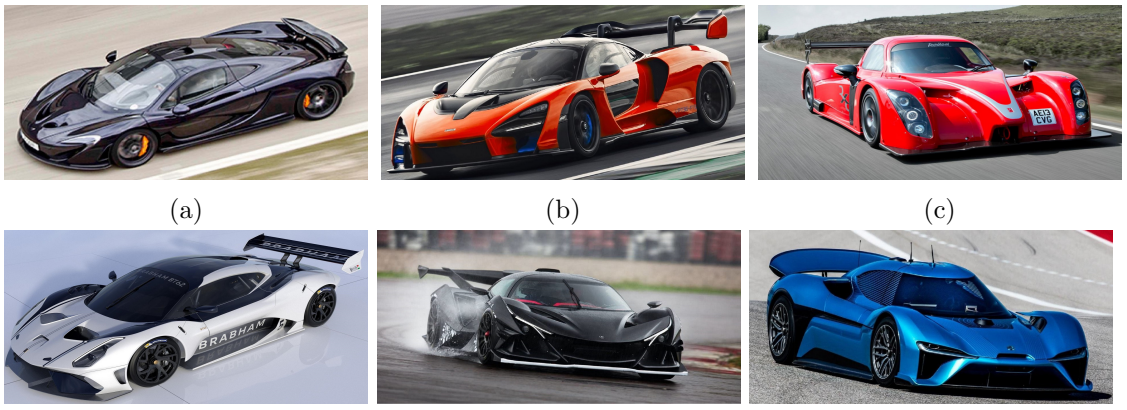

(a) (b) (c)

(d) (e) (f)

Figure 3.1: (a) McLaren P1 [17] (b) McLaren Senna [18] (c) Radical RXC 3.7 [19] (d) Brabham BT62 [20] (e) Apollo Intensa Emozione [21] (f) Nio EP9 [22].

The downforce generation of the nine cars are listed in Table 3.1.

Table 3.1: Stated downforce generation and maximum lateral acceleration of chosen cars.

	Downforce	Velocity	Max Lateral Acc.	
Porsche 911 GT2 RS	450kgf	340km hr^{-1}	-	[23]
Pagani Huayra BC	500kgf	250km hr^{-1}	1.50g	[24, 25]
McLaren P1	600kgf	257km hr^{-1}	2.00g	[17]
McLaren Senna	800kgf	250km hr^{-1}	2.20g	[18]
Radical RXC 3.7	900kgf	280km hr^{-1}	-	[19]
Brabham BT62	>1200kgf	-	-	[20]
Apollo Intensa Emozione	1350kgf	300km hr^{-1}	2.00g	[26, 27]
Aston Martin Valkyrie	1800kgf	-	4.00g	[28]
Nio EP9	2440kgf	240km hr^{-1}	2.53g	[22]

As Table 3.1 indicates, the downforce generation varies significantly between the different cars. The reason for this could be, that the values are evaluated at different velocities. The current record holder at the Nürnburgring, the Porsche 911 GT2 RS, generates the least downforce of the nine cars. Beating track records is thereby not only a matter of having the highest downforce. The Nio EP9 is the current record holder for fully electric vehicles at Nürnburgring. As Table 3.1 lists, this car generates a tremendous amount

of downforce. This high downforce has been achieved by significant CFD analysis and design iterations. The body underwent 170 design iterations through CFD [22]. Hence, generating such an amount of downforce, while keeping the drag minimal, is not trivial.

The lateral acceleration in Table 3.1 is expressed in total g's and is a measure of how well the car corners at specific speeds. The test for this, is usually done on a skidpad, which is a flat piece of pavement with a circle of a chosen radius. This is illustrated in Fig. 3.2.

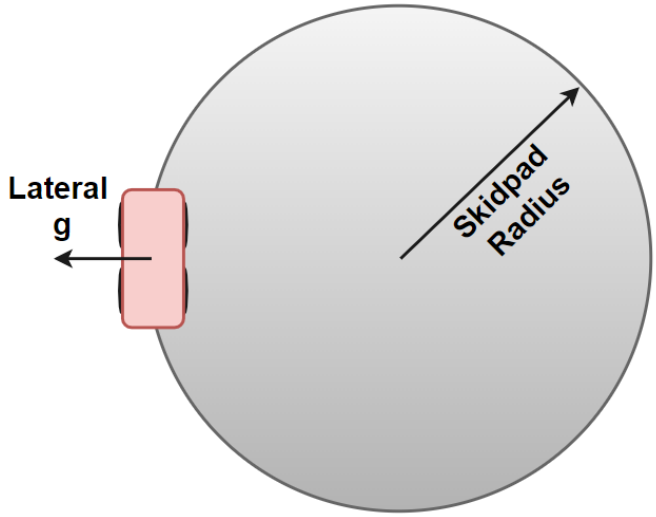

Figure 3.2: Skidpad illustration.

The car drives along the path while attempting to keep the center of the car on the line at all times [29].
The lateral acceleration in terms of g's is then obtained by [30]:

$$g_{Lat} = \frac{\left(\frac{v^2}{r}\right)}{g} \tag{3.1}$$

Here v is the cornering speed, and r is the skidpad radius.
A lateral acceleration greater than 1g is considered a high figure for many types of cars, and it requires high performance tires and chassis to achieve. As a comparison, typical road cars only reach around 0.7g's of lateral acceleration [29].

The required specification in terms of downforce for this car assumes, that the design is able to achieve 3g's of lateral acceleration. As an example to illustrate the forces considered here, it is assumed that the current car is tested on a skidpad with a radius of 60m which is a realistic size. [29]
The normal force acting down on the car to achieve the maneuver at 3 lateral g's, assuming a final car weight of 900kg, is calculated as [31]:

$$F_{Normal,req} = m_{car} g_{Lat} = 26.46kN \tag{3.2}$$

The normal force generated by the car weight itself is found by:

$$F_{Normal,avail} = m_{car} g \mu_{tire} = 11.47kN \tag{3.3}$$

Here g is the gravitational acceleration, and μ_{tire} is the grip coefficient of the tire. This is expected to be 1.3 in this case [1].
The required additional downforce to achieve the maneuver at 3 lateral g's is then obtained by [31]:

$$\text{Downforce}_{req} = \frac{F_{Normal,req} - F_{Normal,avail}}{g\ \mu_{tire}} = 1176.92kgf \tag{3.4}$$

Obtaining the velocity, from Eq. (3.1), gives a speed of $\approx$ 153km hr^{-1}, if the car is able to sustain 3 lateral g's. If the car was only being stabilized by its own weight, the car would only be able to do the cornering at approximately 100km hr^{-1}. This would result in a maximum lateral acceleration of about 1.29g's on the same track.

4. Preliminary Design Study

Besides the downforce, the design will primarily focus on the external drag and flow between the four major parts. The internal drag will not be taken into account, but the different cooling demands will be investigated. The complete bodykit is divided into four major parts, as illustrated in Fig. 4.1.

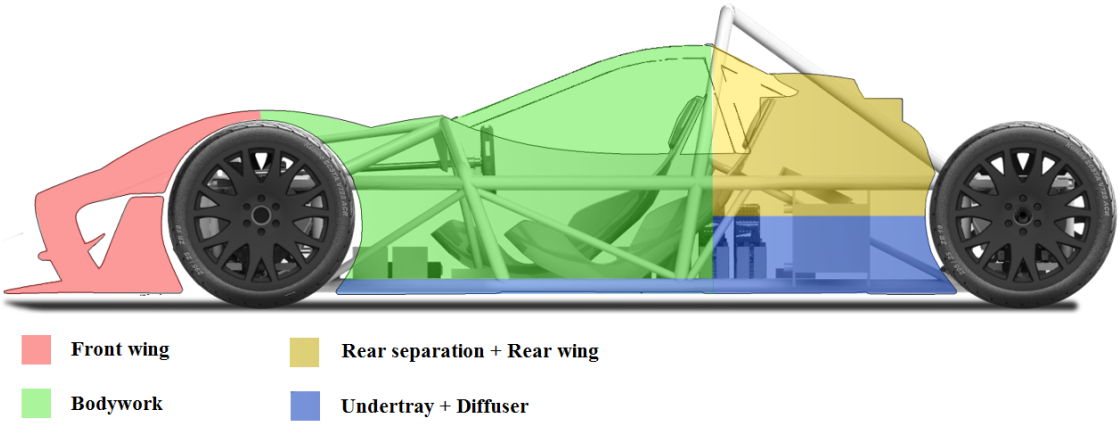

Figure 4.1: Major aerodynamic components.

The three parts; front wing, rear separation and rear wing, and undertray and diffuser are all downforce generating. The bodywork does not generate downforce, but has to ensure a beneficial flow for the rear downforce generating components. Furthermore, it should enable the required cooling, while minimizing drag.
It is difficult to establish any general lift and drag targets for the separate parts. This is highly dependent on the specific car. E.g., the rear wing performance depends on the front wing and bodywork design. Katz (2014) [32] does provide some typical data for closed wheel prototype cars, as encountered in the LMP1 class in WEC. These are listed in Table 4.1.

Table 4.1: Component lift and drag coefficients for closed wheel race car [32].

	C_L	C_D
Bodywork	0.54	0.20
Undertray + diffuser	-1.26	0.10
Front wing	-0.72	0.05
Rear wing	-0.36	0.05
Front wheels	0.00	0.05
Rear wheels	0.00	0.05
Total	-1.80	0.50

Additionally, former head of several F1 aerodynamic groups (Reynard, Benetton, Ferrari, BMW Sauber, and Sauber Motorsport AG) Willem Toet has provided the values in Fig. 4.2 for a 2009 F1 car.

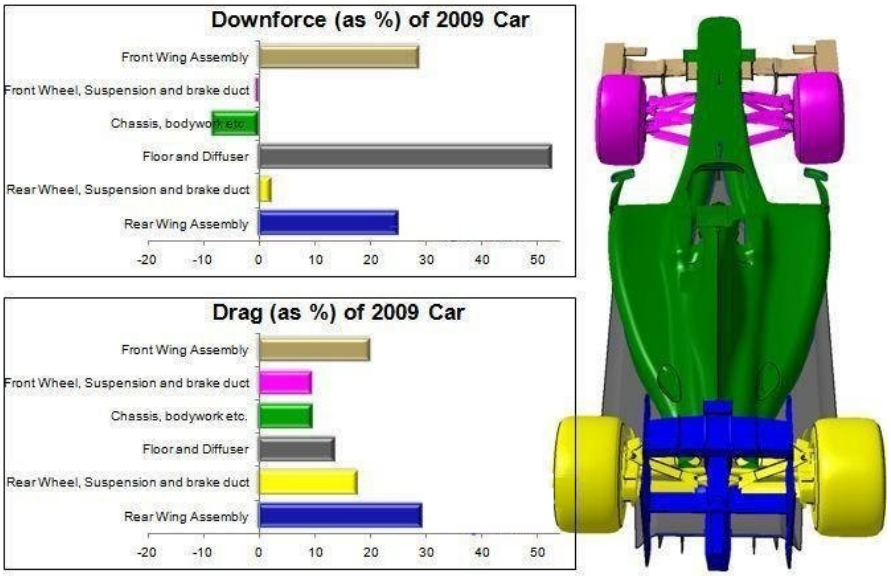

Figure 4.2: Aerodynamics of an F1 car [33].

It is clear from Table 4.1 and Fig. 4.2, that the undertray and diffuser are the primary downforce generating components. Additionally, the bodywork is generating lift for both cases, and has the highest drag contribution for the closed wheel race car.

The race car industry uses several different add-ons, which affects both the lift and the drag. Some of these are listed in Table 4.2.

Table 4.2: Add-on effects for closed wheel race car [32].

	ΔC_L	ΔC_D
Louvres	0.005	0.004
Cowl flaps	0.005	0.005
Dive plates	0.030	0.010
Cut out over wheel	0.004	0.002
Splitter plate (large)	0.009	0.010
Rear vertical fin	≈ 0	≈ 0

A more thorough investigation into the drag and lift are carried out in Sec. 4.1 and 4.2, respectively. The above observations mean, that the bodywork considerations will be presented in the drag part, while the remaining three major components are dealt with in the lift part.

4.1. Drag

The purpose of streamlining a race car body, is to minimize the overall resistance to forward motion. The most undesired resistance is the drag. The net drag force exerted by a fluid on the car body is a combined effect of both wall shear and pressure forces.
The drag contribution made from wall shear stress is referred to as the friction drag, while the pressure induced drag is referred to as the pressure drag. The latter has the largest contribution on race car drag. The pressure drag is highly dependent on the shape of the body. It becomes largest between the front and the wake, and additionally when the fluid is unable to follow the curvature of the bodywork, thereby creating separation.
The drag coefficients for friction and pressure drag are very similar and are defined as [34]:

$$C_{D,friction} = \frac{F_{D,friction}}{0.5\rho v_\infty^2 A} \quad \text{and} \quad C_{D,pressure} = \frac{F_{D,pressure}}{0.5\rho v_\infty^2 A} \tag{4.1}$$

Here F_D is the drag force, ρ is the density, v_∞ is the relative free stream air velocity, and A is the cross sectional area in the flow direction.
The friction contribution becomes dependent on the shear stresses generated in the boundary layer. This is very small for more blunt type bodies and continues to become more negligible as the Reynolds number increases. This is due to an inverse proportionality. But, as the bodywork is streamlined, the friction contribution increases, since the overall surface area increases. For laminar flow, this drag is also independent on surface roughness, but increases with the Reynolds number. However, it becomes a stronger function of roughness as the flow becomes more turbulent.
Typically, when both forces or coefficients are known, they are simply added together to produce the total drag coefficient and forces.
From a theoretical standpoint, the teardrop shape has the lowest total drag coefficient at approximately 0.1. However, this shape is not practical for road ready vehicles, where the shape typically increases the drag coefficient to around 0.3 for passenger cars. Though, it is possible to reduce the drag coefficient to 0.2 for race cars by streamlining the shape. Thereby approaching the theoretical limit of the tear drop shape [34].

4.1.1. Forebody

It is desired to avoid separation on the leading edge (the nose), as this increases the drag considerably. Once the front is designed in such a way, that the flow is attached, it is considered optimal.
The ideal front is approached as the upper horizontal and vertical leading edges are repeatedly smoothed. This means, that there are no sharp edges in the direction of the mean flow. This is illustrated in Fig. 4.3.
The position of the stagnation point is also important. The height of the stagnation point determines the portion of air, that is directed over and under the vehicle. This depends on the chosen design, but generally a lower stagnation point is favorable overall when it comes to passenger cars, due to the rough underside [10]. However, this is not the case for race cars which will need to have sufficient airflow underneath the car for the undertray and diffuser. +

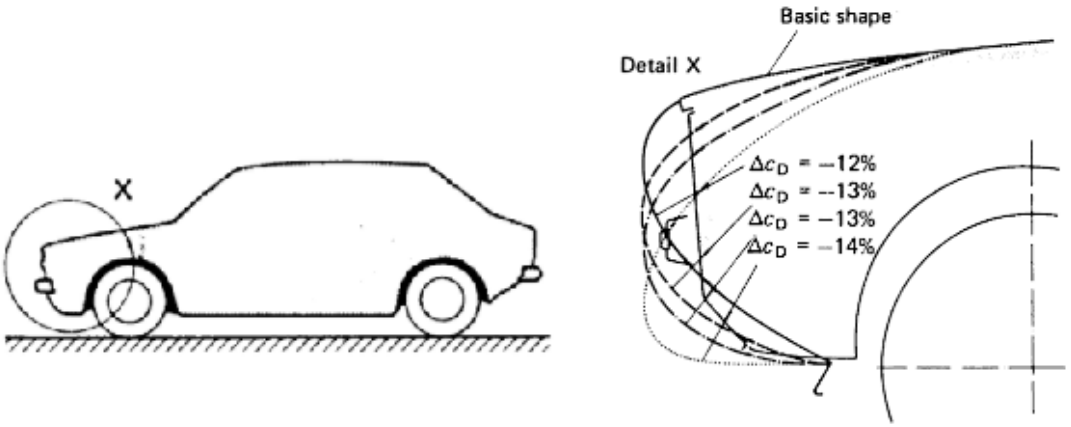

Figure 4.3: Change in drag with front smoothing [10].

4.1.2. Bodywork Streamlining

Intuitively, streamlining of the bodywork is done to reduce pressure drag. But, it should be noted, that the opposite effect occurs on the friction drag, since a larger surface area is introduced by this process. Therefore, both forces should be considered and minimized altogether [34].
The boundary layer on a car is normally only millimeters thick and laminar near the front. This can change to several centimeters and turbulent near the rear. This is illustrated in Fig. 4.4.

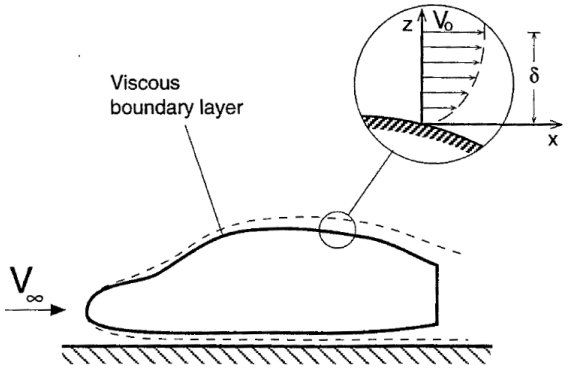

Figure 4.4: Boundary layer thickening on car body [9].

A target for race car designs is to have an attached laminar flow to reduce drag where possible, as the friction drag increases as the flow goes turbulent.
Higher air velocities decreases the boundary layer thickness, it also helps by delaying the occurrence of large pressure drag resistance from flow separation. However, even when large efforts are made to ensure mostly attached flow, design restrictions might give large curvatures, that could create detached flow [9]. The front of Fig. 4.5 is a good example of this.

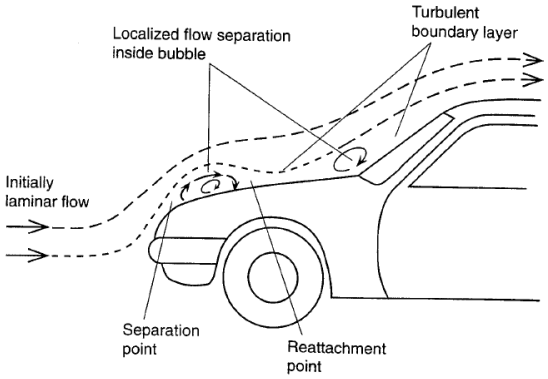

Figure 4.5: Occurrence of localized flow separation due to curvature [9].

The flow is initially laminar, but separates as it hits a large curvature. This flow may result in continuous reverse flow, a "bubble", enclosed by streamlines. This results in a large drag increase. However, this reverse flow typically only occurs at lower speeds, at Reynolds numbers between 10^4 and $0.2 \cdot 10^6$. It is therefore recommended to investigate whether a forced turbulent boundary layer in these regions can have drag benefits, when looking at the entire speed range of the car. A turbulent boundary layer has an overall tendency to be attached longer and delay flow separation. [9]

The inclination of the bonnet and the windshield of the car needs to have a certain steepness to keep the flow attached. The angles are shown in Fig. 4.6.

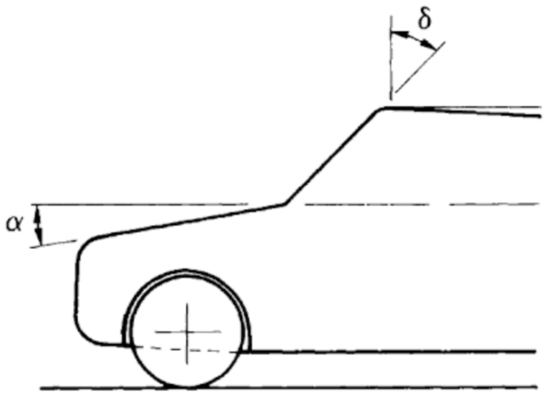

Figure 4.6: Hood and windshield angle [10].

In the study by Hucho (2003) [10], increasing the incline of the bonnet to approximately 10°, decreased the theoretical drag by approximately 12.5%, up until the slope became steep enough for the flow to stay attached. Further sloping beyond this, did not further reduce drag. In case of the wind shield, a change in angle from 35°-65° decreased the drag by approximately 7%.

Several basic body shapes for race cars have been conceptualized to represent a body which is able to create downforce while simultaneously not introducing a large induced drag force. One of these concepts are the *Basic Catamaran*, shown in Fig. 4.7.

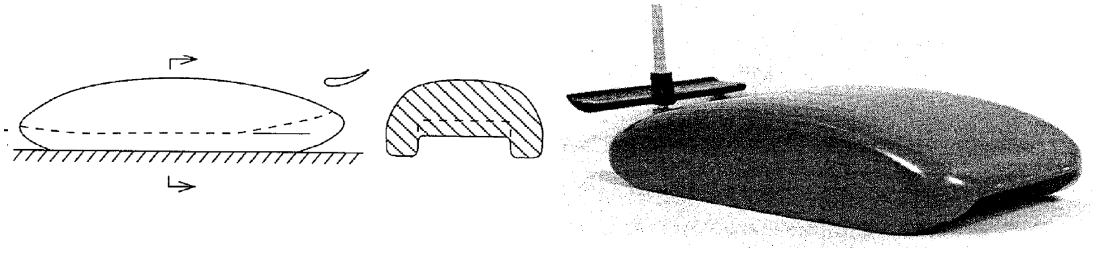

(a) (b)

Figure 4.7: Basic Catamaran body shape [9].

The basic shape covers the wheels and depicts a shape, with a central channel offset from the ground. This channel ends in a venturi with an upward rear slope. The body functionality allows for an undisturbed free stream under the car, whilst reducing the area of flow separation at the rear end. [9]
This configuration allows for low drag and high downforce, and it can be recognized in the design for the Aston Martin Valkyrie shown in Fig. 2.2a.

4.1.3. Rear Separation

In the rear end, the flow forms a wake with large pronounced vortices with the shape and magnitude being dependent on the chosen shape. Some conventional rear shapes and their respective vortice formations are illustrated in Fig. 4.8.

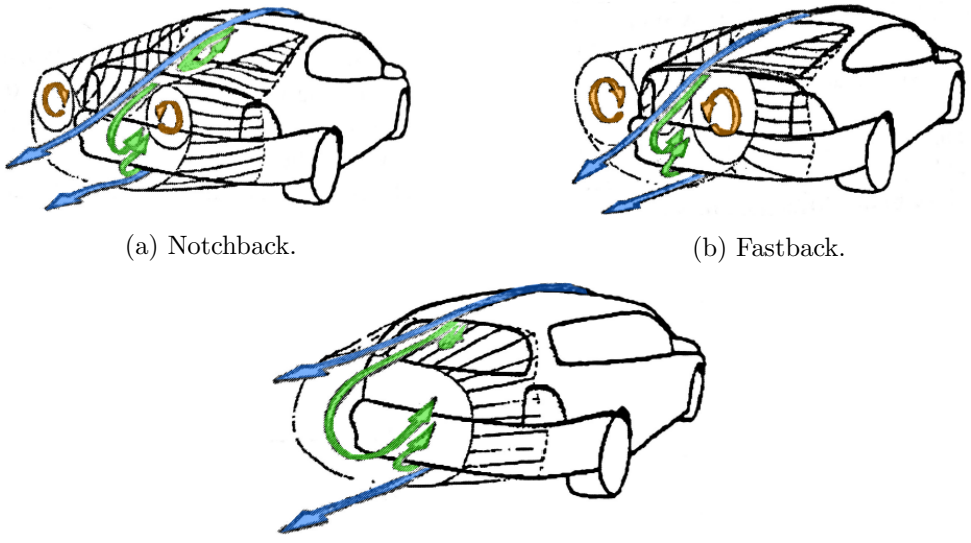

(a) Notchback.

(b) Fastback.

(c) Squareback.

Figure 4.8: Vortices induced by rear shape (modified from [35]).

Two primary types of vortices in the wake are considered here. The first is referred to as a *ring vortex* (marked with green). This type is generated at the sharp edges of the rear, running perpendicularly to the flow direction. These rotate around the axis parallel to the separation line. The second type is a *longitudinal vortex* (marked with orange). This type is horseshoe shaped, and rotates in the direction of the flow. These are created at the slanted edges compared to the direction of the flow. These vortices exist in pairs, and are associated with a large increase in drag.
The overall intensity of the vortices between rear geometries can be seen in Fig. 4.8.
The Notchback in Fig. 4.8a has a similar separation at the rear as the Squareback in Fig. 4.8c. However, the flow starts separating at the rear pillar, with longitudinal vortices rolling away and rotating inwards. This downward deflection has a tendency to create more rear lift compared to the Squareback. The magnitude of the downward deflection is caused by the intensity of the longitudinal vortices. The wake for the Notchback is seen as being smaller, which results in less drag.
The Fastback in Fig. 4.8b sees a separation at the sloping edges at the rear pillars. This forms longitudinal vortices rotating inward, dominating the overall pattern of separation. They also form a downward deflection similar to the Notchback. The difference is, that the longitudinal vortices have a larger downstream flow, and dissipate much later. These are associated with lower pressure, and therefore higher induced drag. Comparing the Notchback and Fastback, it is clear, that a larger slant angle of the rear creates more intense longitudinal vortices. Thus inducing more drag.
For an ideal square shaped geometry, a slant angle between 10-15° should generate less drag by forcing the vortices to begin to counteract each other. Increasing the angle to above 30° would result in the opposite effect, where the longitudinal vortices dominates, and generates the largest drag. [10, 35]

4.2. Lift

Creating negative lift (downforce) is a major part of enabling fast cornering, good high speed stability, and low tire wear and heating [32]. This is done by introducing more grip without adding additional weight. However, at long straight sections at high speed, too high downforce lowers the achievable top speed. The amount of downforce is therefore either a compromise, or active components are added to minimize it at high speeds. It is important to balance the downforce in such a way, that over or under steering is prevented. A front/rear axle balance of 40%/60% can e.g. be found for touring cars [32]. Such downforce distribution is the aim for this study.

The generation of downforce follows Bernoulli's equation, expressed as [34]:

$$\underbrace{P}_{Static} + \underbrace{\frac{1}{2}\rho v^2}_{Dynamic} + \underbrace{\rho g h}_{Hydrostatic} = \text{const.} \tag{4.2}$$

The Bernoulli equation is constant along a streamline. An increased local velocity will increase the dynamic pressure. Thus, decreasing the static pressure, assuming the hydrodynamic pressure change to be negligible. Fig. 4.9 illustrates the flow around an airfoil, generating positive lift.

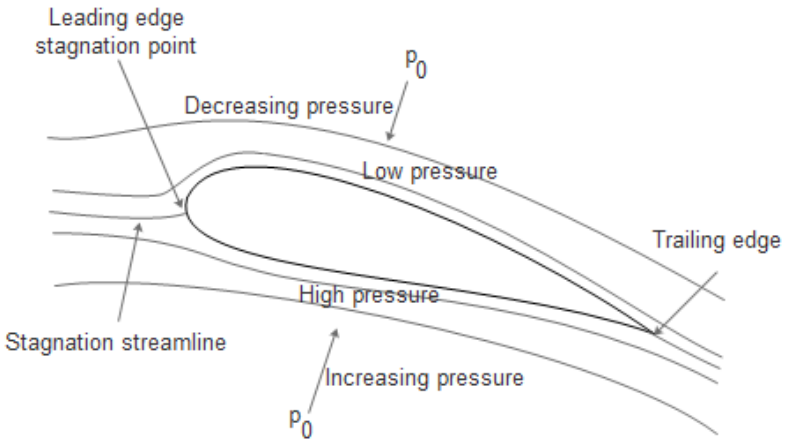

Figure 4.9: Flow around a generic airfoil [36].

The distance the air travels over the airfoil is greater than the distance for the flow going below it. This results in a velocity, and thereby pressure difference, below top and bottom.
When airfoils are utilized to generate downforce, the airfoils are turned upside down. This means, that the low pressure is created between the airfoil and the road.
The pressure difference can be altered by turning the airfoil, thereby changing the angle of attack. The effect of this is airfoil dependent, and is evaluated from lift plots and drag polars, as illustrated in Fig. 4.11.

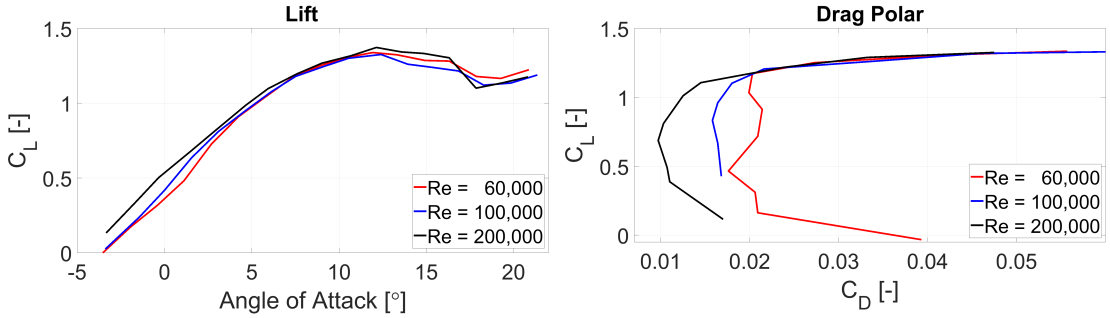

(a) Lift.

(b) Drag polar.

Figure 4.10: GM15 airfoil lift and drag (data from UIUC's airfoil database [37]).

As Fig. 4.10a shows, the lift coefficient for GM15 will increase almost linearly from an angle of attack from -4° to 12°. However, as the drag polar in Fig. 4.10b illustrates, an angle of attack of 12° is not beneficial. In fact, when the airfoil exceeds a lift coefficient of around 1.2 the drag coefficient will increase rapidly. The drag coefficient will more than double, while the lift coefficient will only increase by roughly 0.1. Hence, the most desirable operating point is where the C_L/C_D ratio is the highest.

4.2.1. Front Wing

A front wing implementation will increase the overall traction stability when cornering under high speeds. As indicated in Table 4.1 and Fig. 4.2, the downforce contribution from the front wing is the second most significant one. This is mainly due to the position of the wing, being the only major aerodynamic component in undisturbed air. All other aerodynamic components will be placed behind at least one prior obstruction. It means, that the air has been disturbed and might have some undesirable features, such as vortices. However, the wing in ground effect of the front wing has to be designed to work well with the following aerodynamic components. This means, that the airflow can be directed according to the other components' best performance.

Airfoil shapes are plentiful and their behavior is tuned for different fields of work. Choosing the airfoil for the wing is therefore an evaluation of several different airfoil designs. Initially it is important to find the Reynolds number at which the airfoil should work. However, this requires the chord length and a velocity. The exact chord length is unknown at this point, and the velocity is in a range from 0-280km hr^{-1}. Lastly, is requires lift and drag data at several different angles of attack to fully investigate the most suitable airfoil.
It was chosen to base the investigation on the airfoil data in the easily available UIUC airfoil database [37, 38, 39]. It should be noted, that this is a low-speed airfoil database. The experimental investigation therefore only includes Reynolds numbers up to 500,000. If the final front wing is assumed to have a chord length of 0.2m, the Reynolds number at 280km hr^{-1} would be around 1,000,000. The data does thereby not fit entirely with the expected conditions.

The feature investigated is the lift/drag-ratio, which should give the highest downforce, while inducing minimum drag. The investigation is carried out using MatLab 2017b. Not all airfoils from the database have been included. Only airfoils with data for Reynolds numbers of 400,000, or above, have been considered. It was chosen to omit variations of airfoils with different kinds of alterations from the standard. This means, that only airfoils denoted as *clean* by the sources have been included. The list of the included airfoils can be found in App. A. In total, 24 airfoils met the criteria and were evaluated. The MatLab script evaluates all 24 airfoils at angles of attack between 1° and 11°. The lift and drag coefficients at the specific angles are found from the data and used to calculate the ratio. The highest ratio is then identified.
The result was, that the airfoil SG6043 has the highest lift/drag-ratio, at an angle of attack of 4°. The behavior of this airfoil is illustrated in Fig. 4.11, with the expected operating point marked with the red cross.

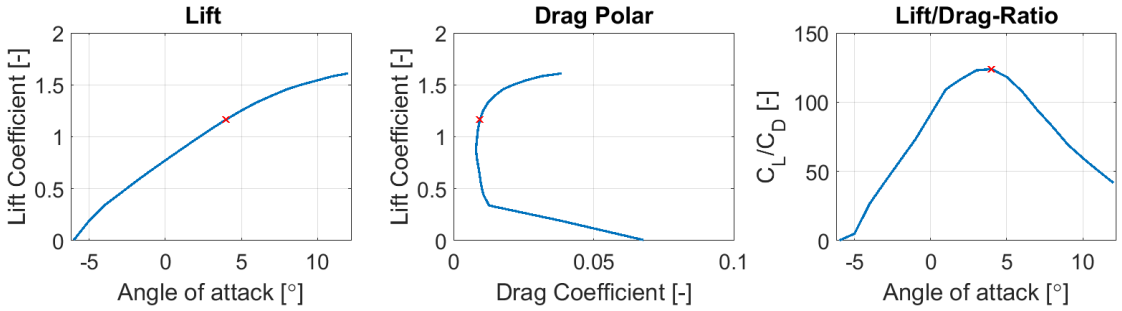

Figure 4.11: Lift, drag, and lift/drag-ratio for the chosen SG6043 airfoil.

The data in Fig. 4.11 are from an experiment at Re = 500,000.
It is important to ensure, that the chosen angle of attack is beneficial for the entire range of velocities. The behavior for all conducted experiments with the SG6043 airfoil are therefore plotted in Fig. 4.12.

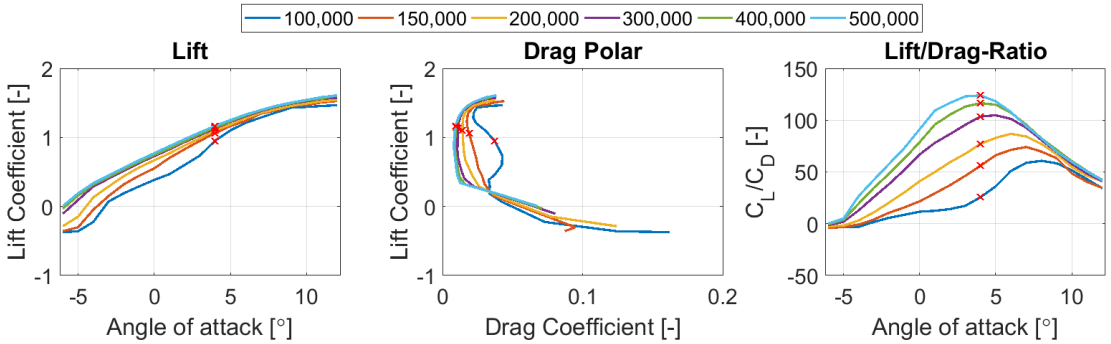

Figure 4.12: Lift, drag, and lift/drag-ratio for SG6043 at different Reynolds numbers.

Fig. 4.12 shows, that the chosen airfoil has a desirable behavior. As the Reynolds number increases, the lift coefficient will increase slightly. Simultaneously, the drag coefficient will decrease. This results in a very significant increase in the lift/drag-ratio, giving better grip at high speeds, while decreasing the drag.
The lift/drag-ratio in Fig. 4.12 also illustrates, that an active wing would increase the performance. This would make it possible to alter the angle of attack according to the velocity. Hence, having the maximum lift/drag-ratio all the time.

A finite wing will have leakage of air at the wing tips. This is air passing from the high pressure side to the low pressure side generated by the airfoil shape [40]. This will in turn decrease the performance of the wing and generate additional drag. The solution to minimize this problem is to install vertical endplates. Additionally, these endplates can be used to direct the flow around the rest of the car. E.g. outwash endplates directing the air around the front tires for F1 cars. This is primarily an issue for open wheel race cars. For closed wheel race cars, the ends will often be closed of by the bodywork.

4.2.2. Undertray and Diffuser

As it was made clear from Table 4.1, the undertray and diffuser combination generates the highest amount of downforce of all components. Historically the undertray has been regulated. This is due to the great expenses used by teams for the development of this specific part. This means, that flat plates are now mandated [32]. However, since the DIS1 race car will not participate in regulated racing, the limitation does not affect this undertray and diffuser design.
The principle of creating downforce via the undertray and diffuser uses two primary principles; the wing in ground effect, and the venturi tube. The wing in ground effect uses the principle described in Sec. 4.2. This means, that a higher velocity below the vehicle will create a low static pressure, thereby "sucking" the car down on the road. The ground effects are complex and includes both flow separation, vortex flow, and flow recirculation [41]. The investigation of these properties are often carried out on simple bluff bodies, such as variations of the Ahmed body illustrated in Fig. 4.13.

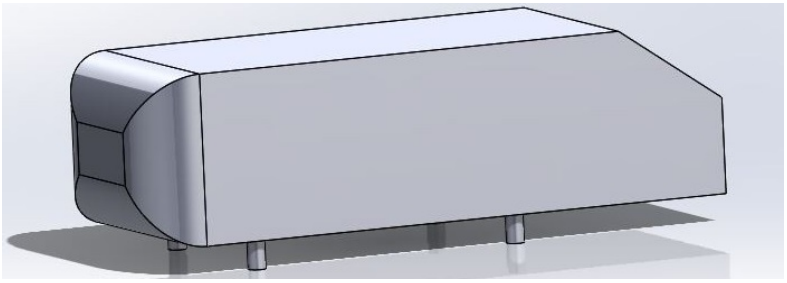

Figure 4.13: Ahmed body with 35° upper slant [42].

A diffuser with side plates are then added to the standard bluff body. This is typically investigated with an Ahmed body with 0° upper slant [41, 43].
Such a bluff body is used to evaluate the dependence of ride height on optimal diffuser angle, as well as finding the critical height, where the downforce decreases rapidly.

The linkage between the generation of downforce and the venturi tube can be illustrated by Fig. 4.14.
As the pressure coefficient plots illustrate, the behaviors are comparable. Though not as effective as the nozzle of the venturi tube, the undertray accelerates the flow. The highest negative pressure coefficient, and thereby downforce, is found just at the beginning edge of the diffuser. The diffuser then decreases the flow velocity, ideally enough to match the free stream velocity. This is to reduce the pressure gradient in the wake.

In order to avoid separation in an expanding rectangular duct an equivalent conical section is calculated. This is based on identical length, and in- and outlet areas to the rectangular duct. These dimensions are illustrated in Fig. 4.15.
The conical equivalent expansion angle must then normally not exceed 7° in order to avoid flow separation [44]. The equivalent conical expansion angle is obtained by [45]:

$$\Theta_{co} = tan^{-1}\left(\frac{C_{r2} - C_{r1}}{L_{diff}}\right) \tag{4.3}$$

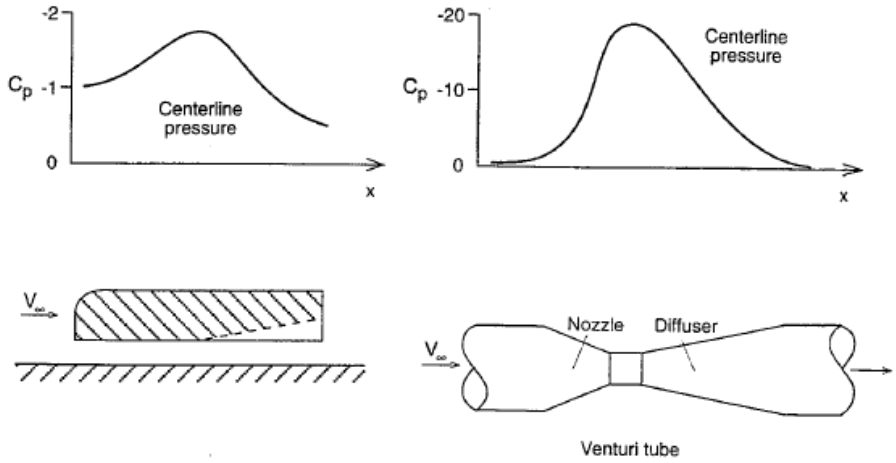

Figure 4.14: Pressure coefficient for modified Ahmed body and common venturi tube [9].

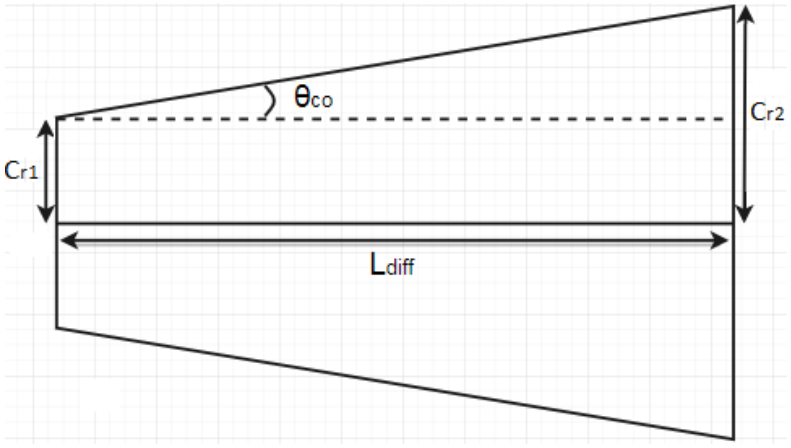

Figure 4.15: Illustration of equivalent conical angle for a rectangular duct.

Here C_{r1} is the cross section of the diffuser inlet, and C_{r2} is for the outlet. L_{diff} is the diffuser length.
However, racing diffusers can achieve attached flow with angles exceeding angles of 20° [46]. The high angle diffusers are used for cars with high ride heights, while diffusers with lower angles are used for lower ride heights.

From Eq. (4.2) it is clear, that a higher velocity will result in a higher local dynamic pressure. Hence, the local static pressure has to decrease. This also means, that a lower ride height will increase the amount of downforce. This can be compared to a venturi tube with a decreasing cross sectional throat area. However, this coherence only holds until a certain point, where the diffuser enters the downforce reducing zone.
The generated downforce is evaluated based on a ratio of the ride height, h_r, and half-width of the car's undertray, d. This is illustrated in Fig. 4.16 for a 17° diffuser on a bluff body.

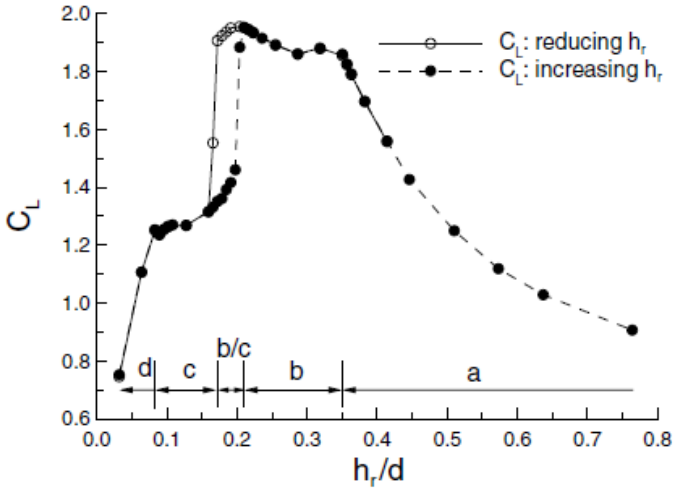

Figure 4.16: Downforce for 17° diffuser on Ahmed-like bluff body [47].

The downforce can be divided into five separate regions as illustrated in Fig. 4.16.

- a: Increasing downforce with decreasing h_r/d-ratio.
- b: Small change in downforce with change in h_r/d-ratio.
- b/c: Aerodynamic hysteresis.
- c: Decreasing downforce with decreasing h_r/d-ratio.
- d: Almost all downforce disappears.

The three flow visualizations in Fig. 4.17 shows the behavior of the flow.

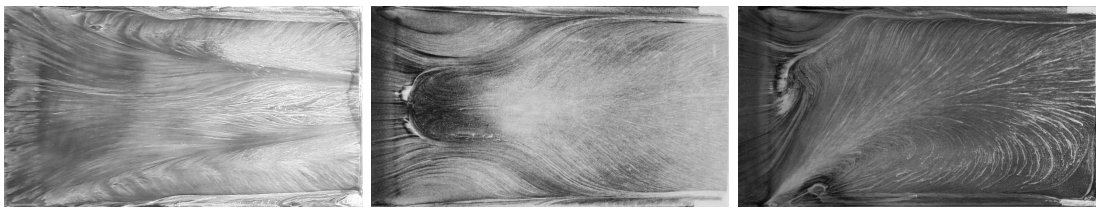

(a) Developing. (b) Ideal. (c) Lost.

Figure 4.17: Developing, ideal, and lost downforce flow visualization [48].

Fig. 4.17a shows the attached flow for the downforce increasing region, where decreasing h_r/d-ratio will lead to an increasing downforce. Fig. 4.17b shows the behavior at maximum downforce. The bubble in the middle shows separated flow, with symmetrical flow on both sides. Fig. 4.17c shows the sudden loss of downforce if the h_r/d-ratio is lowered further. It is clear from this, that the loss is due to one of the symmetrical sides "collapsing", thereby forming a recirculation zone. When this happens, it is necessary to increase the h_r/d-ratio in order to achieve downforce again. This is why Fig. 4.16 has two paths in the area of aerodynamic hysteresis.

Aerodynamic hysteresis covers the behavior around maximum downforce, where a small change in the h_r/d-ratio will have significant effect on the generated downforce. It appears at a h_r/d-ratio between 0.172 and 0.210 for the bluff body [47]. The diffuser angle, θ, giving maximum downforce can be found as

$$\theta = 0.7\frac{h_r}{d}, \tag{4.4}$$

with θ in radians [43, 48].
It is not beneficial to design a diffuser that is too close to the point of aerodynamic hysteresis. A certain margin of safety should be established to prevent the sudden loss of downforce.

An expected performance for the undertray and diffuser of this study can be estimated from Fig. 4.16. It can not be expected, that the car will have an entirely similar behavior, as the Ahmed-like bluff body used for Fig. 4.16. However, this will still give a good indication.
The chassis allows a road clearance of 0.02-0.05m and a half width of 0.6m. This places the undertray and diffuser in region d, with a h_r/d-ratio between 0.03 and 0.08. As illustrated in Fig. 4.16, this is the worst possible region. The target should be to have a ratio within region b.
If the clearance was increased to 0.15-0.18m, it would place the design in a h_r/d-ratio between 0.25 and 0.3. Doing so will theoretically more than double the lift coefficient. This would also ensure, that the area of aerodynamic hysteresis are avoided.

It is clearly visible from Fig. 4.17a, that there are vortices in either side of the diffuser. These vortices are also visible in Fig. 4.18a.

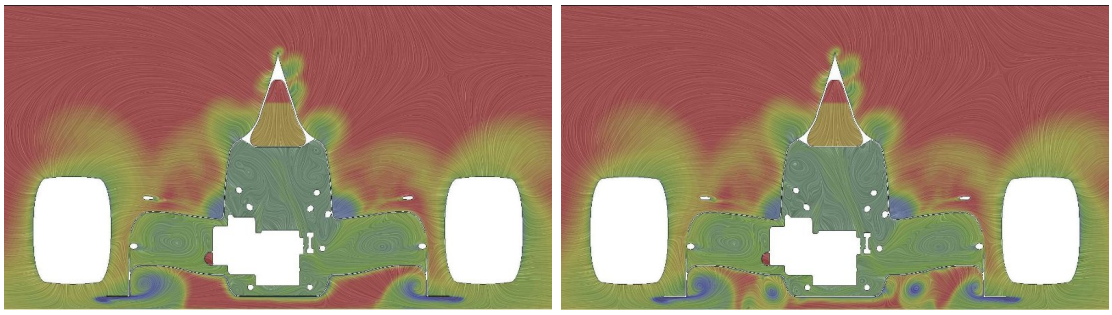

(a) (b)

Figure 4.18: CFD model of formula type car [46].

As Fig. 4.18a illustrates, there is still an energy potential in the middle of the diffuser [49]. This energy can be converted into extra downforce, by creating additional vortices as in Fig. 4.18b. This can be done either by e.g. vortex generators, or by splitting the diffuser into several smaller channels. Jowsey and Passmore (2009) [50] reported a 13% downforce increase by going from a single channel to multiple channels for angles around 16-19°.

4.2.3. Rear Wing

As the purpose of the rear wing is similar to that of the front wing, the same airfoil has been chosen. It is expected, that the rear wing will have a larger chord length, which will give a higher Reynolds number. The evaluation for the front wing should therefore also hold for the rear wing.
Endplates should also be installed on the rear wing to minimize the leakage of air.

The rear wing's low pressure zone can increase the performance of the diffuser if positioned correctly. This increase appears because the low pressure zone at the diffuser exit will accelerate the flow velocity within the diffuser. Thus, decreasing the pressure further within the diffuser, generating additional downforce.
The rear wing can be divided into two wings, each with their own purpose. One wing would then sit close to the diffuser exit, pumping air through it. The other wing would be positioned higher, generating downforce with the inverted airfoil.

4.3. Cooling of Electrical Components

The cooling of the electronic components are expected to be divided into several smaller networks. This means, that each electric motor and generator will have an individual network, with a heat exchanger and an *Insulated-Gate Bipolar Transistor* (IGBT).

4.3.1. Electric Motors and Generators

The two electric motors in the front will experience a continuous load of approximately 40-45kW. The electric efficiency is 80-98%, which means, that the each motor will generate 0.8-9kW of heat energy.
The generators and rear electric motors are identical. It is expected, that they will experience a continuous load of 85-95kW with the same efficiency as the front motors. This means, that each motor and generator will generate 1.7-19kW of heat energy.

4.3.2. Inverters

The car has three inverters, each constructed of two IGBTs, converting AC to DC. Two converters are located in the rear, for the generators and the rear electric motors, and one is located in the front. The continuous load for each IGBT is 110-115kW for the rear electric motors and generators, while it is 50-55kW for the front electric motors. A peak IGBT load of 290kW for the rear, and 125kW for the front can be experienced for periods of a couple of seconds.
It is known from the manufacturer of the IGBTs, that the maximum generated heat energy for each IGBT is 1.5kW [1]. However, the IGBTs' are rated for 480kW continuous and 960kW peak load. It is therefore expected, that the actual heat generation is significantly lower. It is assumed, that it will be maximum 0.5kW for the IGBTs in the rear, and maximum 0.2kW in the front. This is based on the difference between the expected and rated loads.

4.3.3. Heat Exchangers

From Sec. 4.3 and 4.3.1 it is clear, that the cooling networks in the rear have to have higher capacity than the two networks in the front. This fits well with the chosen different sized heat exchangers. The predetermined heat exchangers are two MOCAL 19Row 230mm -8JIC and four MOCAL 34Row 235mm -8JIC [1, 51]. The two smaller heat exchangers are for the front electric motors, while the four larger ones are for the rear electric motors and generators.
The expected flow rate within the networks is 0.13L s^{-1}, with a water-glycol mixture [1]. Mocal provides a graph for the heat dissipation per tube per degree extreme temperature difference (see Fig. 4.19). The data includes two oil per tube volume flows; 0.04L s^{-1} and 0.02L s^{-1}. The extreme temperature difference, T_{etd}, is the difference between the ambient temperature and the coolant inlet temperature.

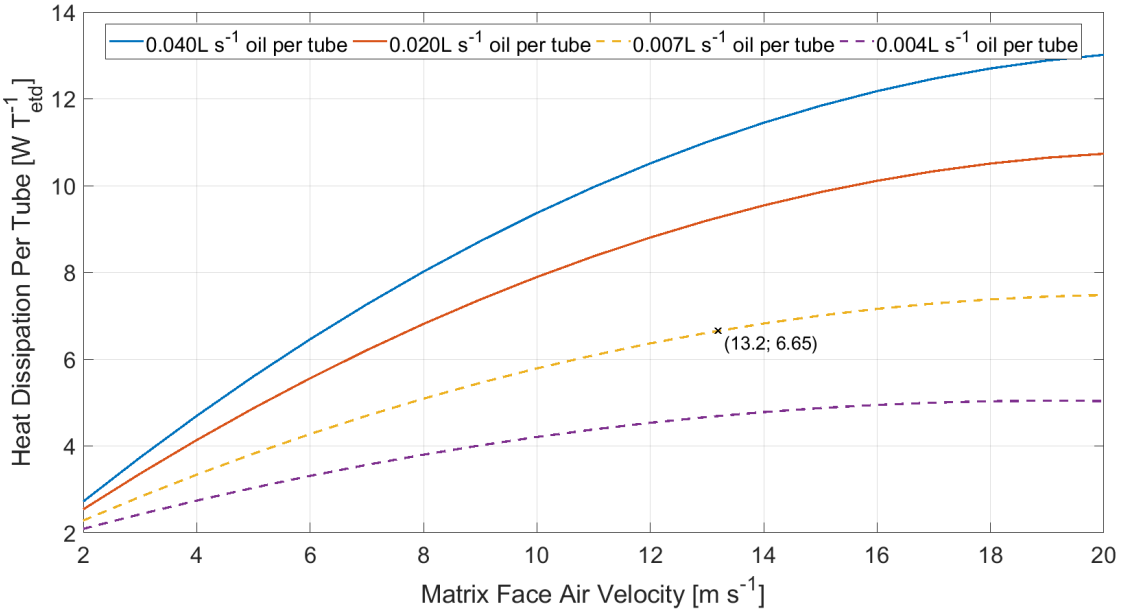

Figure 4.19: Heat dissipation to be expected for heat exchangers (data from [51]).

Unfortunately the coolant flow in the small heat exchangers only amounts to an oil flow of 0.007L s^{-1} in each tube, while it is only 0.004L s^{-1} for the large heat exchangers. The heat transfer at these flows are not known from the data from the manufacturer. It has therefore been assumed, that the change with lower oil flows are linear. Two lines for 0.007L s^{-1} and 0.004L s^{-1} have been plotted using this assumption.

In order to calculate the required matrix face air velocity, the required heat dissipation per tube has to be calculated.
The front heat exchanger networks each have to have a capacity of 9.2kW in order to cool both the IGBT and the electric motor. The rear heat exchanger networks each have to have a capacity of 19.5kW in order to cool both the IGBT and the electric motor/-generator.

When this is determined, the required heat dissipation per tube per T_{etd} can be calculated as:

$$\dot{Q}_{per\ tube\ per\ T_{etd}} = \frac{\dot{Q}}{n_{tubes} T_{etd}} \tag{4.5}$$

The result of this is, that the front heat exchangers have to dissipate 6.45W tube^{-1}K$_{etd}{}^{-1}$. The rear heat exchangers have to dissipate 7.65W tube^{-1}K$_{etd}{}^{-1}$.

From the plot in Fig. 4.19 it is concluded, that the front heat exchangers should have a matrix face velocity of approximately 13.2m s^{-1} (marked with x in Fig. 4.19). Here it is assumed, that the water-glycol mixture has the same heat transferring properties as the oil used to create the Mocal plot.
The flow rate in the rear heat exchangers is too small to have a readable matrix face air velocity with the required heat dissipation per tube in Fig. 4.19. However, it looks like the slopes are decreasing with an increasing matrix face air velocity. Having a matrix face air velocity higher than the 20m s^{-1} will therefore not be beneficial. It is therefore suggested, that the flow rate in these heat exchangers is increased to match the flow rate per tube in the front heat exchangers. This will require a total coolant flow rate of 0.24L s^{-1}.
It is assumed, that this will be implemented, which means, that the matrix air face velocity should also be 13.2m s^{-1} for the rear heat exchangers.

4.4. Brake Cooling

The proposed rotor brake kit for the car consists of the Ultralight 32 vane rotor, and the forged dynalite caliper brake pad from Wilwood [1]. The brake rotor is shown in Fig. 4.20.

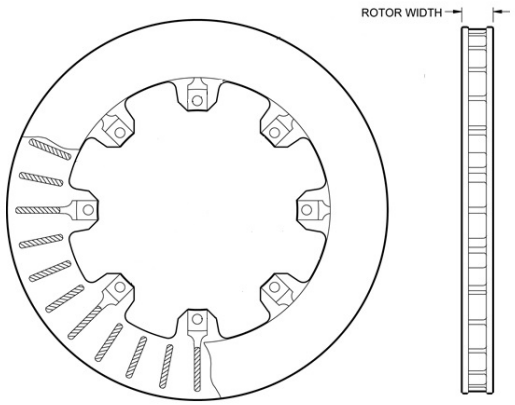

Figure 4.20: Illustration of brake rotor (modified from [52]).

The brake rotor is constructed of cast iron, with a rotor width of 20.5mm, and an outer diameter of 298.5mm. It weighs 3.6kg and has 32 vanes internally for heat management.

It is desired to decelerate the car from 250-50km hr^{-1} by approximately 2g, where the brake balance load should be distributed as 60/40% in the front and rear, respectively [1].
The largest energy put into a single front rotor, has been estimated to be 393.44kJ by DIS Race Lab [1]. Furthermore, it has been assumed that 90% of that energy is transferred to the rotor. This results in a temperature rise of around 207.42K.

The scenario considered here is, that the wheel is covered by the bodywork, except for the outward facing rim. This is exposed to the surrounding free stream air. It is assumed in this case, that there is a cooling channel, redirecting air to the rotor brake system. For this analysis, it is assumed that the velocity is at least equal to the chosen free stream velocity the car is supposedly traveling at. This is then investigated at four different velocities, ranging from 150km hr^{-1} to 210km hr^{-1}.
An analogy to forced convection over a flat plate is made. It is assumed, that both sides of the rotors are exposed to the free stream air. The properties of air for this calculation, are found at an average film temperature between the supposed maximum rotor surface temperature and a free stream temperature of 20°C. This gives an average film temperature of 123.71°C.
It is assumed, that the internal heat conduction is faster than the forced convection. This means, that the rotors can be modeled as lumped systems, where the temperature throughout is considered uniform, with no local temperature differences present within the metal.

When airflow is parallel to the side of the rotor, the Reynolds number at the end is calculated by:

$$Re = \frac{v_\infty D_{rotor}}{\nu_{air}} \tag{4.6}$$

This gives $Re \approx 6.04 \cdot 10^5$ for 150km hr^{-1}, which is greater than the critical Reynolds number ($5 \cdot 10^5$ [34]). This indicates, that there is a combined laminar and turbulent flow across the rotor. The average Nusselt number over the rotor surface, can be expressed as [34]:

$$Nu = \frac{hL}{k} = (0.037Re^{0.8} - 871)Pr^{1/3} \tag{4.7}$$

The convective heat transfer coefficient, h, can then be obtained from Eq. (4.7).
The rate of heat transfer due to convection is then obtained as:

$$\dot{Q}_{conv.} = hA_s(T_s - T_\infty) \tag{4.8}$$

This system will also transfer energy by radiation. The rate of heat transfer due to radiation is obtained as:

$$\dot{Q}_{rad.} = \epsilon\sigma A_s \left(T_s^4 - T_\infty^4\right) \tag{4.9}$$

This uses the Stefan-Boltzmann constant, σ ($5.670 \cdot 10^{-8}$W m^2K^4), and a dimensionless emissivity, ϵ, of 0.71 [34].

These rates of heat transfer can then be used to calculate the temperature change after one second, using Eq. (4.10).

$$\dot{Q}_{conv.} + \dot{Q}_{rad.} = m_{rotor} c_{p,iron} \frac{dT}{dt} \tag{4.10}$$

By doing so an *Ordinary Differential Equation* (ODE) appears. Thus, the expected temperature at any given time step can be calculated.
This has been done in MatLab until the rotor has been cooled to 50°C. The results are plotted in Fig. 4.21.

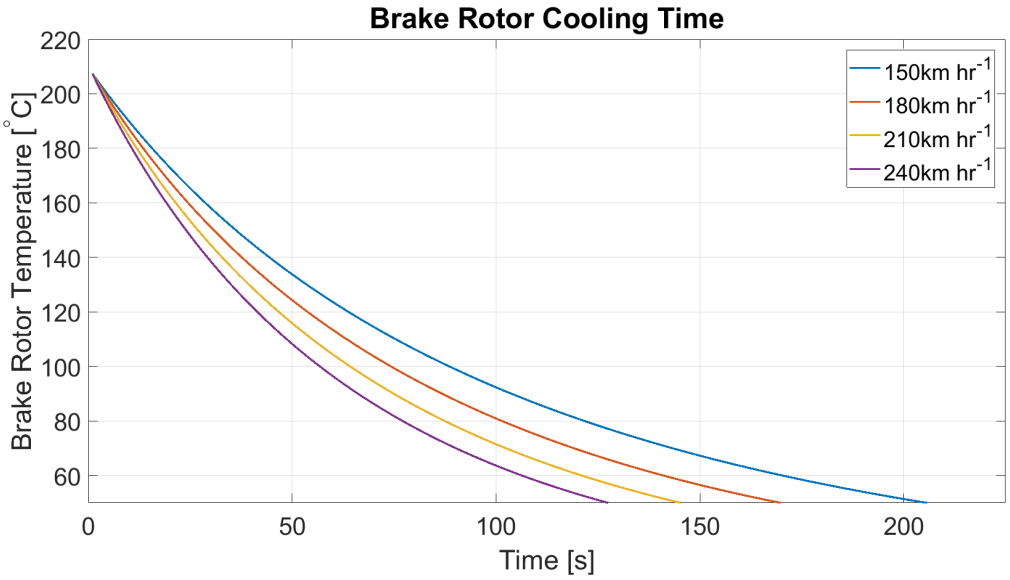

Figure 4.21: Cooling time for different free stream velocities.

The actual heat transfer should be faster than this illustrates. This is primarily due to the vanes in the middle of the rotor. The surface will increase substantially due to these. The cooling times in Fig. 4.21 are therefore conservative estimates.

4.5. Combustion Engine Cooling and Air Feed

The combustion engine has not yet been defined. It will therefore not be investigated in detail. However, it is possible to estimate both the required air intake and expected heat generation. This can be done from a combustion point of view.
Whether the combustion works in a fuel rich or fuel lean environment will not be evaluated. The investigation will be simplified to use stoichiometry.

Stoichiometry for gasoline is not trivial, as it is composed of more than 200 different hydro carbons [53]. Furthermore, the composition will vary depending on the source of the crude oil from which the gasoline was distilled. Hence, it is almost impossible to know the exact composition of the gasoline. An approximate composition of $C_{8.26}H_{15.5}$ is used [53].

The stoichiometric combustion of this gasoline mixture in atmospheric air follows the reaction expressed in Eq. (4.11).

$$C_{8.26}H_{15.5} + 12.135(O_2 + 3.76N_2) \longrightarrow 8.26CO_2 + 7.75H_2O + 45.63N_2 \tag{4.11}$$

The O_2 + 3.76N_2 is the approximate composition of atmospheric air.
From this, the air/fuel-ratio can be determined by:

$$(A/F)_{stoic} = \frac{4.76a}{1}\frac{MW_{air}}{MW_{fuel}}, \tag{4.12}$$

where the coefficient a is 12.135, which is obtained from Eq. (4.11).
This gives an air/fuel-ratio of 14.51, which means, that for every kilogram of fuel, the engine will require 14.51kg of air.

The thermal efficiency of an internal combustion engine, using gasoline, varies depending on several factors. E.g., engine rpm and load. The thermal efficiency of a gasoline engine is around 26-30% [34]. This means, that 70-74% of the energy is lost as heat somewhere in the system. The higher heating value for hydrocarbon fuels ranges from 43-55kJ/kg [53]. Using the average of this range, this means, that between 34.3kJ/kg and 36.26kJ/kg will be converted into heat for every kilogram of gasoline combusted.

4.6. Chassis Modifications

The provided chassis in Fig. 2.3 (also shown in Fig. 4.22a) did not take the aerodynamics into account. Several design changes were therefore proposed to the mechanical engineers responsible for the chassis. These changes aimed at; lowering the highest point of the roll cage, allowing the expansion of the diffuser, and allowing the diffuser inlet to have a low angle.

The roll cage on the initial chassis design and the modified chassis are illustrated in Fig. 4.22.

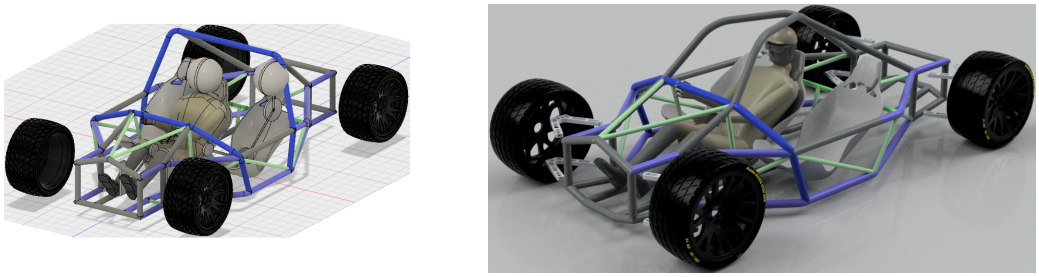

(a) (b)

Figure 4.22: DIS1 initial chassis design and modified chassis [1].

The new design does not cover the passengers, which means, that some kind of protection should be included before it is roadworthy. In order to facilitate this, the corners of the roll cage of Fig. 4.22a should therefore still be taken into account when developing the bodykit. The new roll cage meant, that the highest point was lowered approximately 5cm.

The expansion for the diffuser was made possible by introducing an angle on the lowest part of the chassis in the rear. The modified chassis rear is illustrated in Fig. 4.23a.

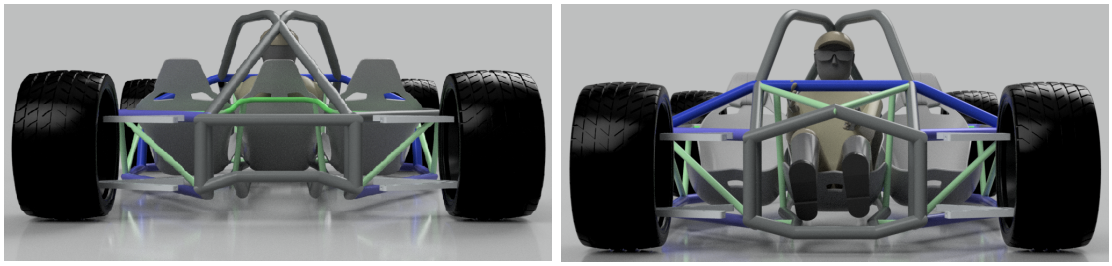

(a) (b)

Figure 4.23: Modified chassis front and rear [1].

The maximum change enabled an inclination of approximately 13° in the middle, and 11° in the sides, below the suspension. It was not possible to start the expansion near the car's midpoint as desired. Instead, the expansion starts at the rear axle, which will affect the downforce distribution significantly.
The front was sought angled in a similar fashion. It was only possible to do a minor change, since the gas and brake pedals are mounted at the lower bar. The modified chassis front is illustrated in Fig. 4.23b.

The chassis could still be refined in terms of adjusting for the aerodynamic components. However, the considerations regarding e.g. the combustion engine, batteries, generators, and electric motors are complex, and lengthy. The chassis in Fig. 4.22b and 4.23 is therefore the basis for this study, together with the width proposed by the preliminary chassis design's roll cage.

4.7. Preliminary Design Study Summary

The different criteria gathered in the preliminary design study are summarized here. These are the design guidelines and principles, governing how the first body should be shaped.

Forebody and front wing

- Front shall not have any sudden changes in inclination.
- Bonnet inclination should be at least 10°.
- The SG6043 airfoil is implemented as the front wing at an angle of attack of 4°.

Bodywork

- The bodywork shall be shaped to avoid abrupt changes in geometry to ensure flow attachment.
- The Basic Catamaran body, with a large opening for the diffuser inlet, would be beneficial to incorporate.

Rear separation and rear wing

- The rear body slant angle shall be between 10-15° to avoid large longitudinal vortices in the wake.
- Rear wing will use the SG6043 airfoil.
- Rear wing angle of attack shall be adjusted based on the rear body mean flow, to have the appropriate angle of attack of 4°.

Undertray and diffuser

- Expansion angle below 20°.
- Diffuser throat shall be placed as close to the car center as possible.

Several of these points can only be fully described by a thorough CFD model. They can therefore not be taken fully into account for the first design proposition.

Due to time constraints it has been chosen to not deal directly with the cooling demands. This is done to limit the extent of the study. The locations of the specific cooling duct in- and outlets will therefore not be evaluated.

4.8. Initial Design

The initial design proposal is denoted as the 0^{th} Iteration. The design is illustrated in Fig. 4.24, rendered in Autodesk Fusion 360.

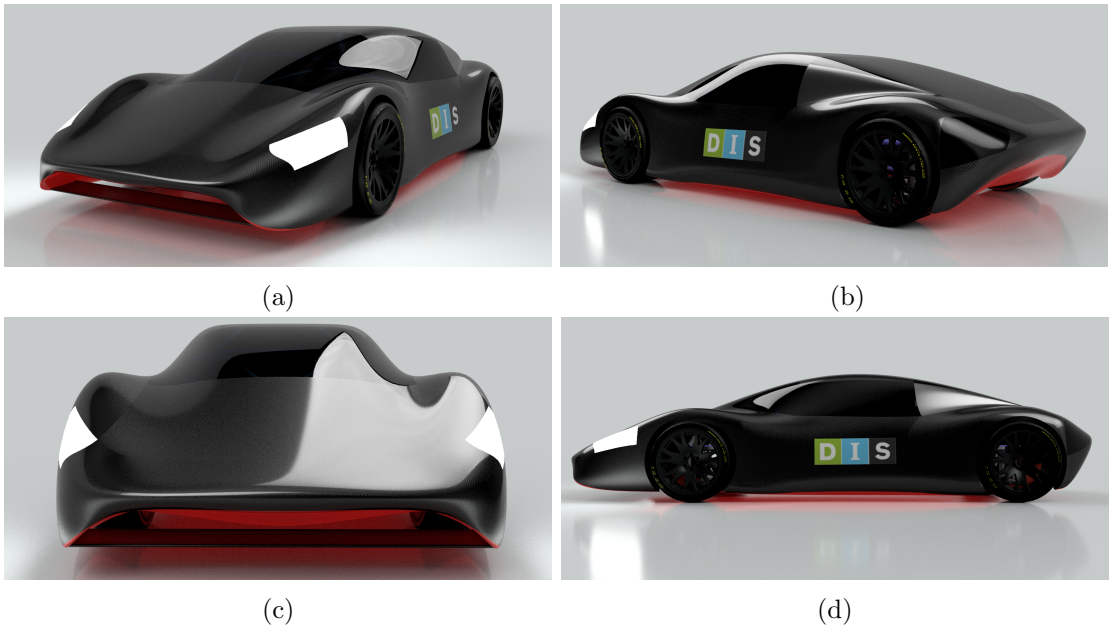

(a) (b)

(c) (d)

Figure 4.24: First design proposal (0^{th} Iteration).

Compared to the two cars presented in Fig. 2.2, the initial design resembles the Aston Martin Valkyrie the closest. This may be due to the fact, that this also has bodywork in the style of the Basic Catamaran (see Fig. 4.7).
As Fig. 4.24a and 4.24c illustrates, the front wing has been positioned in the diffuser inlet, far from the chassis front. This is done in order to help adjust the downforce balance, since the diffuser and rear wing downforce contribution will be applied behind the rear axle. The angle of the hood and the front windshield is 16.3°, on average, from the highest point of the roof, to the leading edge of the hood. The line between these two points is almost unbroken, to avoid recirculation zones.
The rear angle is 15.5° on average from the highest point of the roof, to the trailing edge of the rear. This angle is slightly higher than recommended, which might cause flow detachment. If this is the case, it will be visible early in the optimization process.
The diffuser has been designed as a single channel, without side vanes. This has been done to make it simple. Making an initial design very advanced might be a waste of time, since it is highly dependent on the flow after the front wing. However, it is expected, that the diffuser would at least benefit from side vanes.
The rear wing has been left as an add-on for a later iteration, since knowledge of the flow behind the vehicle's highest point will help determine the best location and the angle needed for the rear wing.

5. CFD

The shortcomings of the initial design should be reduced in the preliminary CFD study of the model. This should ensure, that the fluid topology optimization in Sec. 6 can focus on the minor, but effective, details.
First, the current design, illustrated in Sec. 4.8, is simulated to show the aerodynamic properties of that design with the included front wing, and simple diffuser. Then preliminary manual modifications to the design are made. This includes the determination if a rear wing or modifications to the underside of the car are necessary.
The model with the newly added manual modifications is then analyzed in the same manner, to investigate the effects made by these changes.
The process is then repeated for another design iteration, to reduce possible inadequate features of the modified design.

The CFD model is carried out using Ansys Fluent v. 19.0. The software is documented in a theory and a user guide [54]. These are used to describe the choices and the used methods unless cited otherwise.
The primary hardware used in this study is listed below:

- Processor: Intel® Core™ i7-4700MQ CPU @2.40Ghz.
- Cores: 4.
- Threads: 4.
- Ram: 12GB 1600Mhz dual channel.

The available resources are rather small for this type of study. They will therefore most likely be limiting in terms of model resolution. Due to the restrictions for the primary hardware, a higher powered workstation was made available by the AAU supervisor for a limited time. This computer had the specifications listed below:

- Processors: Two Intel® Xeon® CPU E5-2637 v4 @3.50Ghz.
- Cores: 4 (each) and 8 (total).
- Threads: 8 (each) and 16 (total).
- Ram: 256GB 2400Mhz.

This higher powered workstation, was primarily used for the fluid topology optimization in Sec. 6.
Several sources note the required number of cells to resolve the flow sufficiently. Ansys uses the study by Frank et al. [11, 13] as an example of a car aerodynamics case study. This uses a mesh with 42 million cells. A guideline by Fluent describes a mesh with 5.5 million cells as coarse, while a mesh with 11 million cells is fine [55]. It should be noted, that this guideline dates back to 2005, which means, that this definition most likely has changed due to increased computational resources. Casiraghi (2010) [56] describes a model size of 40-60 million cells. This typically utilizes a cluster.

It is clear from these different studies, that the mesh size in this study can be limiting due the computational resources available. This will affect the resolution and accuracy of the flow features.

The model simplifications and assumptions are summarized below:

Simplifications and assumptions

- Side forces are negligible.
- No internal flow within the car is present.
- The rotation of the wheels is not implemented.
- Fluid structure interaction of flexible components are omitted.
- Negligible surface roughness of the car body.

5.1. Expected Flow Features

As aerodynamics are very dependent on the geometry of each individual case, it is difficult to determine specific expected features. However, the car's slopes in both front and rear have been designed to avoid separation. It is therefore expected to have attached flow on the entire upper body.
The rear of the car does not represent either of the three common shapes illustrated in Fig. 4.8. This means, that the type of vortices in the wake is unknown. Though, it is expected that it will primarily have large lateral vortex pairs, due to the sloping of the back.

5.2. Model Preparation

The car model is converted from the CAD software, with a chosen number of surfaces to allow for better control of surface meshing in specific parts of the model. This is presented in Fig. 5.1a with the resulting converted 3D model illustrated in Fig. 5.1b.

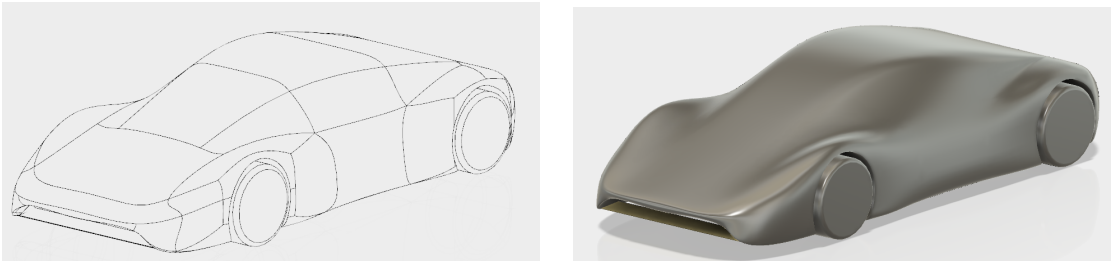

(a) Car converted surfaces.

(b) Resulting 3D model.

Figure 5.1

Simple cylinders are implemented to represent the wheels. The wheel suspension is omitted, and an air gap is present between the wheels and the bodywork.

Additionally, small wedges have been implemented, connecting the wheels with the ground, as illustrated in Fig. 5.2. This was done to avoid having a concave angle. Such angles are difficult to mesh with satisfactory quality.

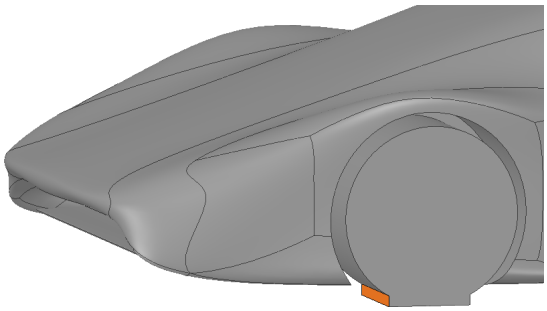

Figure 5.2: Wheel wedge.

The computational domain representing the wind tunnel, has to have a space in front of the car equal to at least 3 car lengths, and 5 car lengths behind [55]. The requirements for the height and width of the tunnel are not specified. It was chosen to extend the wind tunnel half a car length in these directions.
It is further recommended to create an internal domain, which can be used to control the meshing near the car. This is recommended to be at least half a car length in each direction, and about a car length in the wake [55]. However, this has been found to be problematic, since the resulting mesh would become insufficient in cell quality due to the limited available computational resources. It has therefore been chosen to narrow the box to a smaller size. The chosen size, has been established from a preliminary investigation of the flow field behavior. Through this investigation it was studied how far the effects, introduced by the car, would propagate into the flow field. The box was sized to the smallest possible size this would allow without interfering with these effects. The final dimensions of this internal domain are half a car length in front, half a car height from the top surface, a car length in the wake, and a half car width +0.5m to the side. The dimensions for the outer wind tunnel bounds have not been altered.
Lastly, symmetry is exploited, such that the entire domain is split in half, in order to reduce the computational requirement.
The model domain is shown in Fig. 5.3

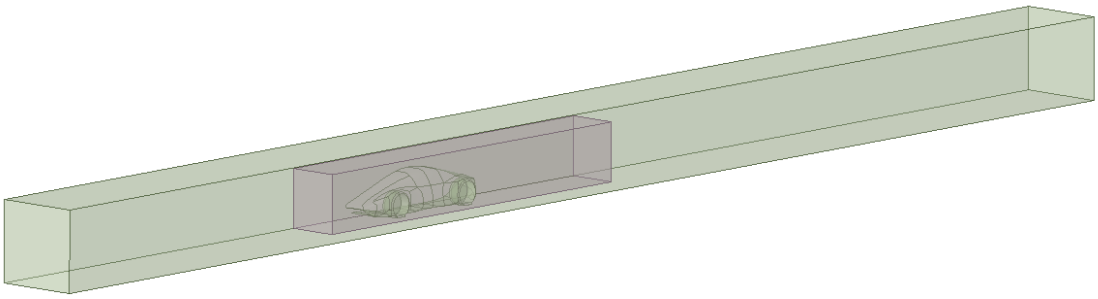

Figure 5.3: Model domain.

5.3. Governing Equations

The CFD model in this study uses two governing equations. In order to solve these, six transport equations are used. These are the velocity component in three directions, u, v, and w, the pressure, P, the turbulent kinetic energy, k, and the turbulent dissipation rate, ϵ.

The first governing equation, is the continuity equation, that governs the conservation of mass. It is written in the form for incompressible flow as in Eq. (5.1).

$$\frac{\partial \bar{u}_i}{\partial x_i} = 0 \tag{5.1}$$

The second governing equation is the steady state *Reynolds Averaged Navier-Stokes* (RANS) equation, expressed in Eq. (5.2). This describes the conservation of momentum in the three dimensions.

$$\underbrace{\rho \frac{\partial \bar{u}_i \bar{u}_j}{\partial x_j}}_{\text{Convection}} = \underbrace{-\frac{\partial \bar{P}}{\partial x_i}}_{\text{Pressure gradient}} + \underbrace{(\mu + \mu_t)\left(\frac{\partial^2 \bar{u}_i}{\partial x_j^2}\right)}_{\text{Stresses}} + \underbrace{\rho g_i}_{\text{Gravitation}} \tag{5.2}$$

The gravity term is applied in the y-direction:

$$g_i = \begin{pmatrix} 0 \\ -9.8 \\ 0 \end{pmatrix} \tag{5.3}$$

The turbulent viscosity, used to calculated the stresses in Eq. (5.4), is expressed as [54]:

$$\mu_t = \rho C_\mu \frac{k^2}{\epsilon} \tag{5.4}$$

The C_μ term is a function of mean strain and rotation rates, as well as angular velocity for the Realizable formulation of the k-ϵ turbulence model.
The k and ϵ terms are the turbulent kinetic energy and turbulent dissipation rate, respectively. These two terms are defined as expressed in Eq. (5.5) and (5.6) for the Realizable k-ϵ turbulence model.
The turbulent kinetic energy is expressed as [54]:

$$\frac{\partial}{\partial x_j}(\rho k \bar{u}_j) = \frac{\partial}{\partial x_j}\left(\left(\mu + \frac{\mu_t}{\sigma_k}\right)\frac{\partial k}{\partial x_j}\right) + G_k - \rho\epsilon \tag{5.5}$$

The turbulent dissipation rate is expressed as [54]:

$$\frac{\partial}{\partial x_j}(\rho \epsilon \bar{u}_j) = \frac{\partial}{\partial x_j}\left[\left(\mu + \frac{\mu_t}{\sigma_\epsilon}\right)\frac{\partial \epsilon}{\partial x_j}\right] - \rho C_2 \frac{\epsilon^2}{k + \sqrt{\nu\epsilon}} \tag{5.6}$$

In both of these expressions, the G_k term is the generation of turbulent kinetic energy due to mean velocity gradients. C_1 and C_2 are constants. Both σ_k, and σ_ϵ are the turbulent Prandtl numbers for the respective parts.
The Realizable model is stated to show large improvements over the standard formulation of k-ϵ in regards to streamline curvature, vortices, and rotation. This should make it ideal for identifying possible separation and reattachment of the flow over the car body. In fact, this model is recommended, as it has been shown to predict integral values (e.g. the drag coefficient) within a 2-5% error margin compared to wind tunnel experiments [55].
This statement is also supported by CFD studies conducted on external aerodynamic of cars, noting the strengths and ability of the model. A study by Ahmad et al. (2010) [57] confirmed a drag prediction, with a 4% error compared to wind tunnel experiments. Bordei and Popescu (2011) [58] conducted a substantial comparison between seven different turbulence models, on the efficiencies of drag, lift, and general aerodynamics. This was performed on a notchback race car with wings, across several codes, such as Ansys Fluent, CFX and OpenFoam. The comparison showed, that the Realizable model gave the second best consistent result overall amongst these parameters.

5.4. Boundary Conditions

The flow can be considered as incompressible even at top speeds of 280km hr^{-1}. This means, that a velocity inlet boundary condition is used. The air velocity in the wind tunnel is prescribed to 77.77m s^{-1} in the normal direction. The static temperature is set to default at 293.15K.
The outlet boundary at the end of the wind tunnel is set as a pressure outlet, with 0Pa gauge pressure, for atmospheric conditions.
A symmetry boundary condition is implemented, since the flow pattern is expected to have mirror symmetry.
The ground is a moving boundary with a transverse velocity of 77.77m s^{-1} in the flow direction, in order to avoid an unphysical boundary layer beneath the car.

5.5. Wall Conditions

In general, there are two approaches to attempt to model the effect of the near wall region of the car. One way, is to use semi-empirical formulas called wall functions, to bridge the region affected by viscosity to the fully turbulent mean flow region. This approach does not resolve neither the viscous sublayer nor the buffer layer.
The other approach is referred to as near wall modeling. This requires sufficient mesh resolution all the way to the wall in order to resolve the viscosity affected region. Thus, requiring a very large number of cells.
It is recommended to use non-equilibrium wall functions for external aerodynamic simulations, as this is sensitive to pressure gradients and local variation of the viscous sublayer thickness [55].
Using this function is also supported by the Ansys Fluent theory guide [54]. It states, that the function can be utilized to predict flows involving separation and reattachment. This should provide improvements when attempting to predict wall shear/skin friction.

According to the ERCOFTAC best practice guidelines [59], the prediction accuracy of the wall function depends on the lower limit of y^+. This is a non-dimensionless wall distance defined as Eq. (5.7).

$$y^+ = \frac{\rho u_t y}{\mu}$$
$$u_t = \sqrt{\frac{\tau_w}{\rho}} \tag{5.7}$$

Included in Eq. (5.7), is the frictional velocity, u_t, the distance to the wall, y, and the wall shear stress, τ_w.
During the meshing it should be ensured, that the lowest y^+ values are around 20-30, in order to resolve the boundary layer. If the y^+ values are below this, it enters the buffer and viscous sub layer, which is not resolved.

5.6. Computational Methods

Solving the transport equations requires a choice of discretization scheme.
Several different formulations are available in Ansys Fluent. The choices used in this study are listed in Table 5.1.

Table 5.1: Chosen computational scheme and methods.

Pressure-Velocity Coupling	
Scheme	SIMPLEC
Spatial Discretization	
Gradient	Least Squares Cell Based
Pressure	PRESTO!
Momentum	Second Order Upwind
Turbulent Kinetic Energy	Second Order Upwind
Turbulent Dissipation Rate	Second Order Upwind

SIMPLEC has been chosen for the pressure-velocity coupling, as it is recommended for turbulent flows with large pressure gradients. Furthermore, it should provide more flexibility as it allows for modifications to the pressure-correction under-relaxation factor, which may lead to more stability and faster convergence.
For the pressure, the standard scheme will be replaced with PRESTO! since it is recommended for high speed rotating flows, and for strongly curved domains.
Momentum, turbulent kinetic energy, and turbulent dissipation rate shares the use of the second order upwind method. Higher order methods exist, but they might not necessarily give a better result. It is stated that the second order upwind is sufficient for most cases [54].

5.7. Meshing Procedure

The accuracy of the calculated drag and lift is largely determined by the predicted pressure distribution, since the pressure drag is the most dominant contributor (see Sec. 4.1). It is therefore very important to resolve locations with flow separation or flow reattachment. This means, that great care should be taken when meshing the surface of the car. This should ensure, that all curves and geometric features are resolved properly.

A prism element inflation layer is desired on all car surfaces. The rest of the domain can be filled with tetrahedral elements. These layered inflation elements should ensure better alignment with the flow direction near the surface. Thus minimizing numerical diffusion, and provide lower skewness of the cells to better handle the viscous effects. It is recommended to have the prism layer's first cell aspect ratio at 5, with a geometric growth rate of 1.2 [55]. However, this configuration requires very small face sizes on the various surfaces of the car, which results in very large mesh sizes. For this reason, another approach was adopted, where the first cell height on different surface segments of the car is specified. This height is determined through trial and error as the near wall velocity varies over the car surface. The first cell height should be adjusted until the desired y^+ value of between 30-100 has been reached. The aim is to have the first five cells within the buffer layer, which ranges between 30 to 300.
The desired type of inflation layer is illustrated in Fig. 5.4.

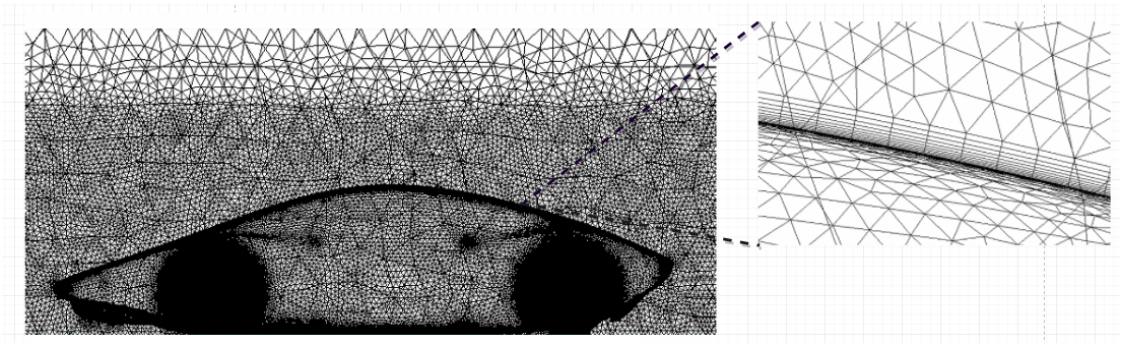

Figure 5.4: Mesh with prism inflation layer.

Unfortunately, this process results in stairstep mesh in some unidentified parts of the geometry. The simulation were therefore not able to converge. Due to the instability it was necessary to omit the inflation layer. This will in turn lower the precision of the calculated lift and drag.
The shortcomings of the current mesh will be considered when evaluating the final design for the preliminary iterations investigations. Furthermore, it might be necessary to adjust the mesh before the fluid topology optimization is carried out. This is dealt with in Sec. 6.4.

Even though it was established in the beginning of Sec. 5, that the mesh size is limiting, different mesh sizes should still be evaluated. This should show how much parameters such as the lift and drag coefficients change when the mesh is refined further.

Furthermore, it should also give insight to the statement, that the mesh is coarser than ideal.
This investigation is based on the 0^{th} Iteration design.

5.7.1. Mesh Quality

The two quality parameters; aspect ratio, and equiangle skew are used to evaluate the quality of the mesh. These have to be inside certain ranges for the case to be well meshed. The aspect ratio is a measure of how the cells are stretched to fit the geometry. It is favorable to avoid large aspect ratios in locations with large changes to the flow field. According to ERCOFTAC best practice guidelines [59], the upper acceptable range is between 20 to 100 in regions of interest.
The aspect ratio of the different mesh sizes are listed in Table 5.2.

Table 5.2: Cell aspect ratio with mesh refinement.

Meshsize (No. Cells)	Min/Max	Average
4,493,408	1.16 / 11.45	1.81
6,883,540	1.16 / 12.71	1.81
9,334,008	1.16 / 12.71	1.80
11,814,589	1.16 / 15.62	1.79
13,818,530	1.16 / 16.58	1.79

All meshes have an excellent aspect ratio quality.

The skewness analysis compares the angle of each cell to that of the ideal cell shape, i.e. all tetrahedral faces should appear close to that of an equilateral triangle. The equiangle skew is expressed as [60]:

$$\text{Equiangle skew} = \max\left[\frac{\theta_{max} - \theta_{ideal}}{180° - \theta_{ideal}}, \frac{\theta_{ideal} - \theta_{min}}{\theta_{ideal}}\right] \tag{5.8}$$

Here θ_{max} is the largest angle in a face or cell, and θ_{min} is the smallest angle. θ_{ideal} is the angle of an ideal cell, which is 60° for a tetrahedral.

The skewness quality between the mesh sizes is shown in Fig. 5.5

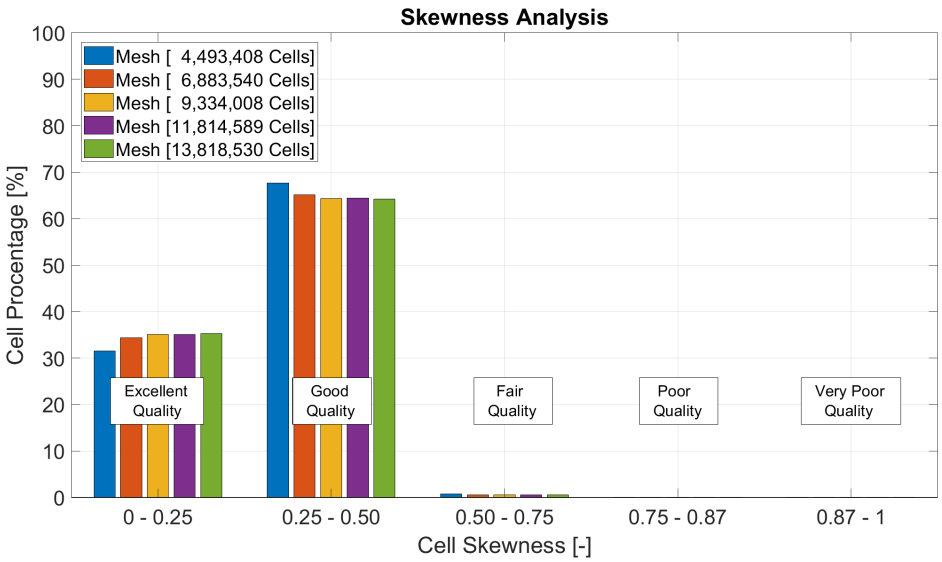

Figure 5.5: Skewness quality amongst meshes.

It is clear from Fig. 5.5, that the cells are of good quality. Neither of the meshes contain cells of very poor quality. Furthermore, the number of cells of excellent quality increases as the mesh is refined.

5.7.2. Mesh Independency Study

A mesh independency study is carried out, to illustrate the change as the grid is continuously refined. The total drag force on the car has been chosen as the parameter of comparison for this purpose. This should give insight to the possibility of the grid size being a limiting factor on the quantity of the resulting parameters in the model.
The change in the drag force parameter amongst the chosen mesh sizes shown in Table 5.2 is plotted in Fig. 5.6.

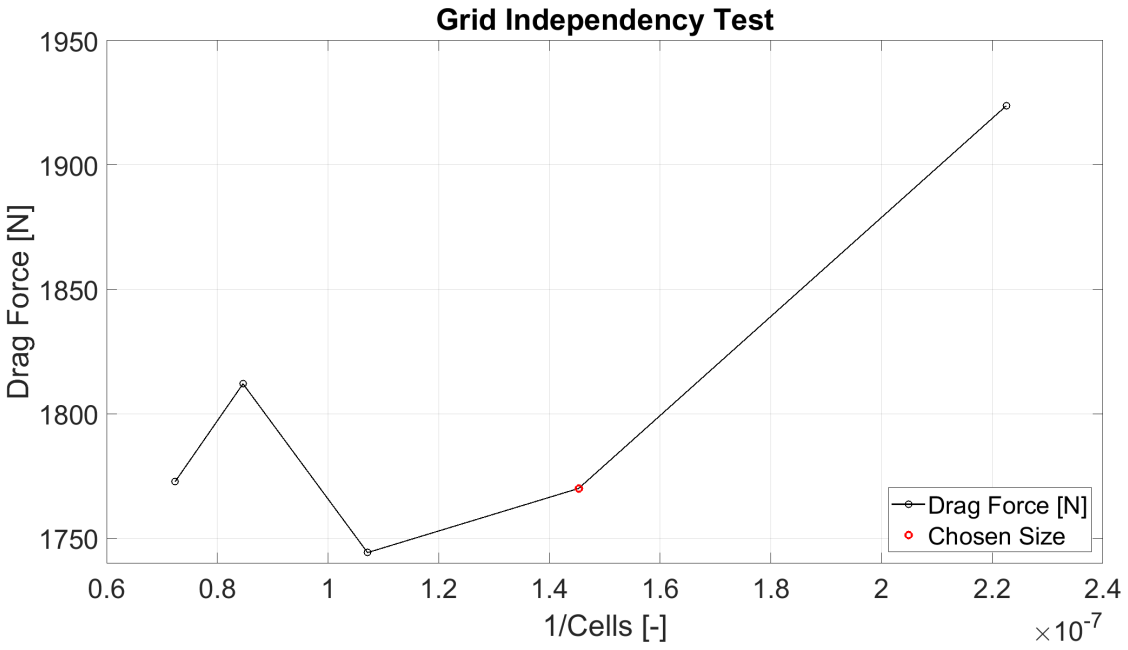

Figure 5.6: Change in drag force with mesh refinement.

The total drag force decreases rapidly by 8.01% when the grid is refined from 4.5-6.9 million cells (coarsest mesh to the second coarsest mesh). However, after this point, the drag force is a bit unsteady among the finer meshes. This seems to indicate, that larger meshes are required to find a value that is independent on further refinement. Unfortunately, as previously explained, this is not possible. The change from the second most refined mesh to the most refined mesh only results in a change of 0.15%. The increased cell count, from approximately 6.9 million to approximately 14 million, is therefore unnecessary. It is for this reason, that the preliminary CFD models will be simulated with a mesh of approximately 6.9 million cells as a compromise between simulation efficiency and accuracy.

5.8. CFD Results

The evaluation of the different design iterations primarily focus on the lift and drag coefficients. Furthermore, the flow behavior is assessed.

5.8.1. Iteration 0: Initial Design

Within the evaluation of the results of Iteration 0, the convergence should also be evaluated. The results from this investigation can then be used for the coming design iterations.

Convergence

The model was initially allowed to run for a total of 3000 iterations. The residuals for these iterations are shown in Fig. 5.7.

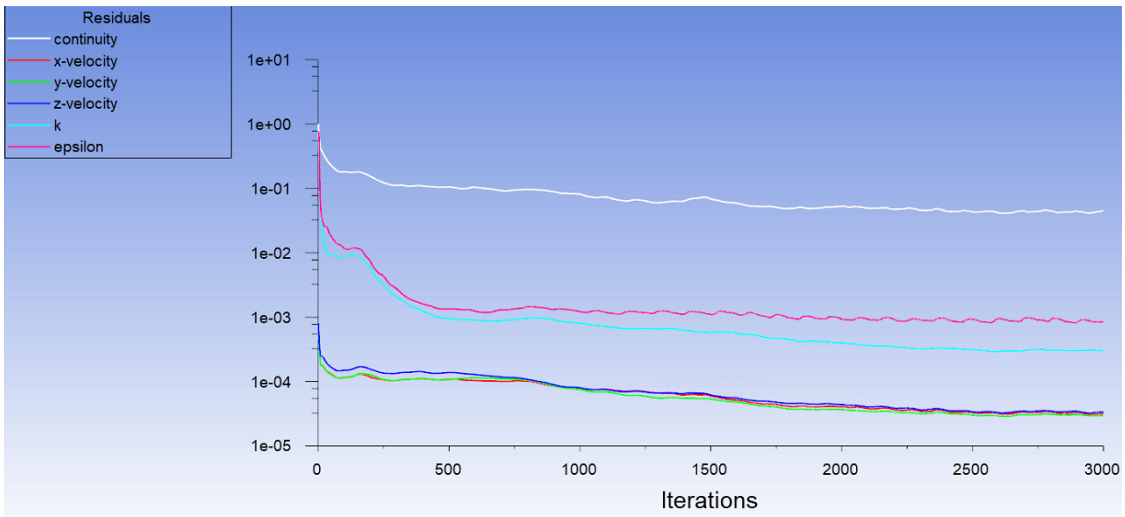

Figure 5.7: Simulation residuals for iteration 0.

Fig. 5.7 shows slow convergence, and it can been seen, that the residuals have not completely converged. However, the plot seems to have found a steady and slightly oscillating behavior. Extending the simulation with a further 5000 iterations continued to show this oscillation, as illustrated in Fig. 5.8.

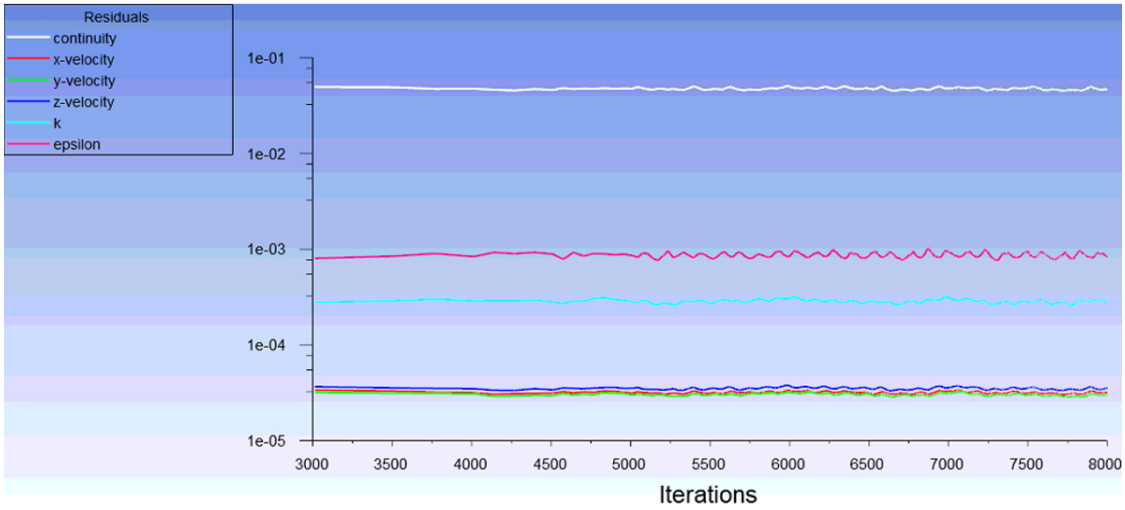

Figure 5.8: Extended simulation residuals for Iteration 0.

The wind tunnel outlet pressure has been monitored and plotted in Fig. 5.9 for every 500^{th} iteration.

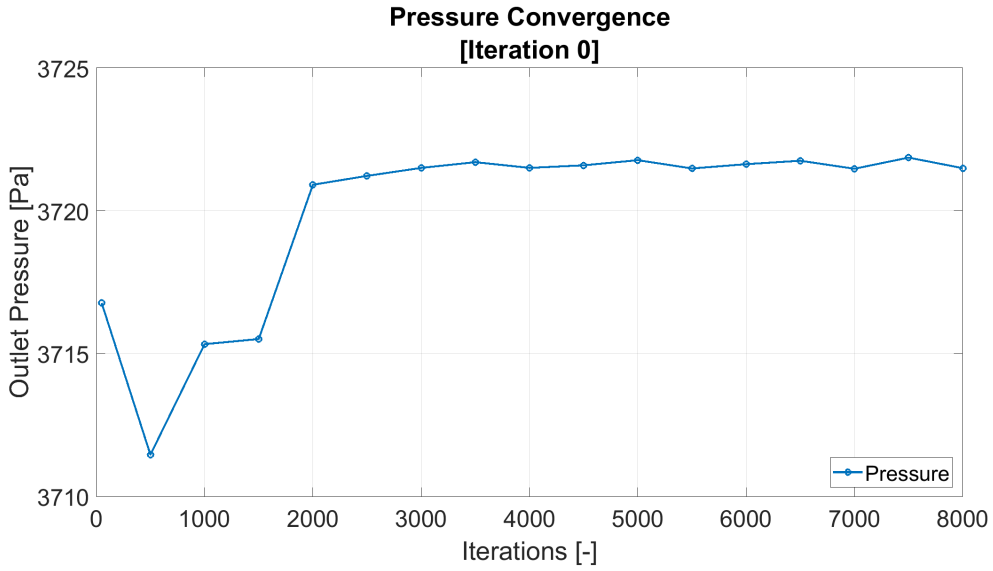

Figure 5.9: Pressure convergence.

As Fig. 5.9 shows, the outlet pressure has converged to a steady value after 3000 iterations. However, the change from 2000 to 3000 iterations is negligible.
The lift and drag coefficients are both plotted in Fig. 5.10 for a reference area of 1m^2.

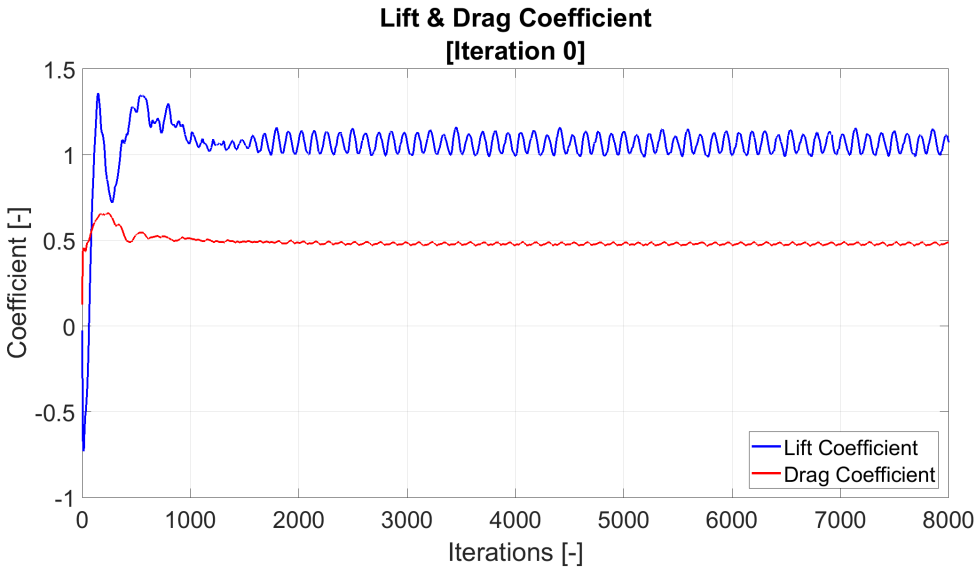

Figure 5.10: Lift and drag convergence.

As Fig. 5.10 illustrates, the solution for both coefficients seems to have trouble converging to a fully stable value. Both oscillates within a small interval after 2000 iterations. It is expected, that these oscillations are due to the flow generated in the wake.

Flow Behavior

The flow streamlines across the car are shown in Fig. 5.11.

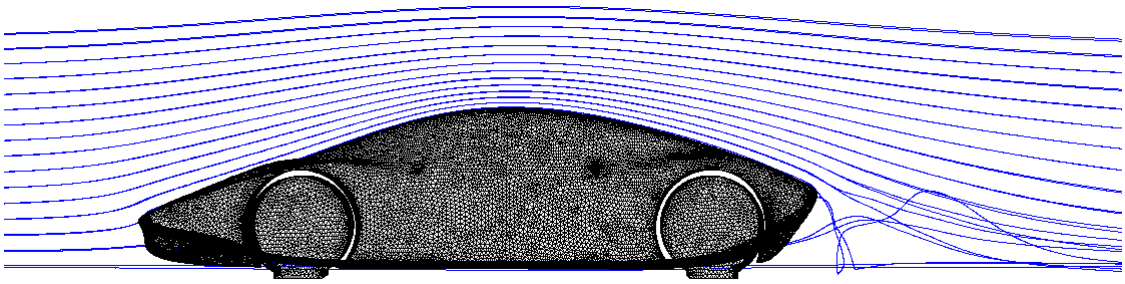

Figure 5.11: Streamlines at the symmetry plane.

Fig. 5.11 shows the desired attached flow across the upper bodywork. The expected vortices are also visible in the wake of the car. These are expected to be the source of the oscillating behavior of the residuals.
The size of the vortices in the wake is easier to assess from Fig. 5.12.

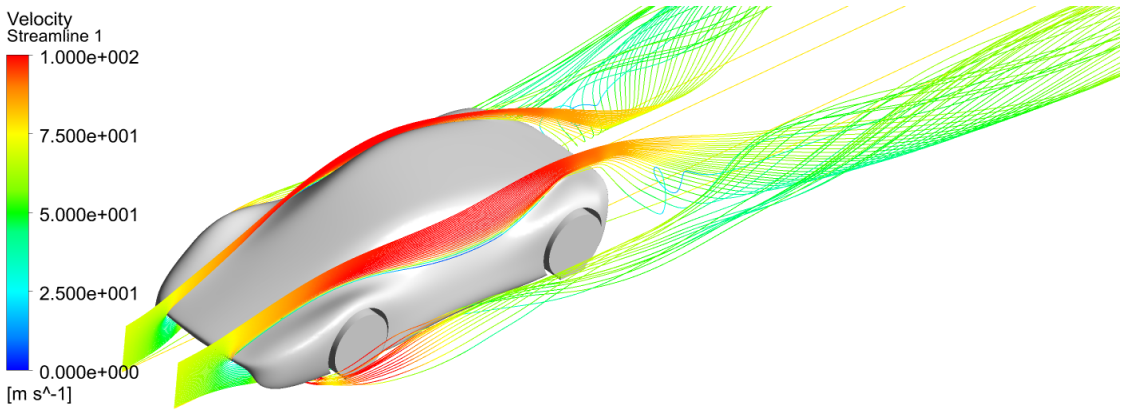

Figure 5.12: Velocity magnitude across the car.

The wake is very large and the dominant behavior is two longitudinal side vortices. This is beneficial, as it should create less rear lift than when they are not present (see Sec. 4.1.3). However, the wake extends far behind the car, leading to increased drag. This could indicate, that the current diffuser expansion angle is too steep.
Fig. 5.12 also shows an acceleration across the top part of the car which generates positive lift.
The result of the body streamlining is visible on the static pressure contour plots in Fig. 5.13.

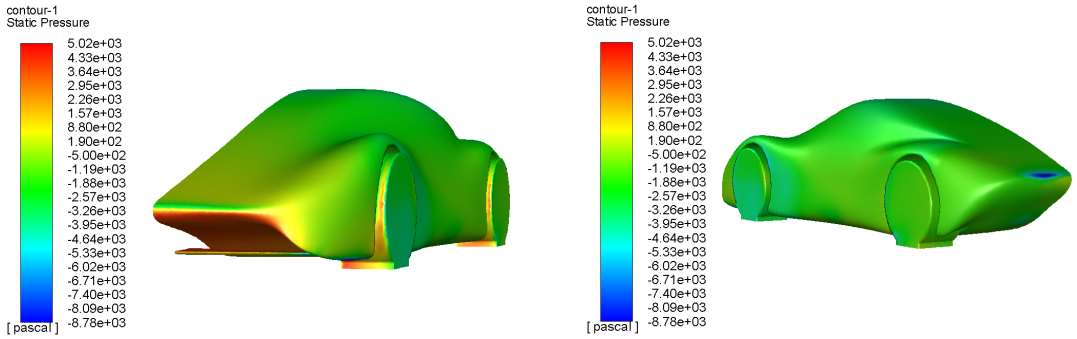

(a) (b)

Figure 5.13: Static pressure contour.

The contours illustrate, that the bodywork mostly has uniform negative static pressure. This indicates, that neither recirculation nor reattachment are present across the body. Furthermore, this supports the attached flow in Fig. 5.11. The contours also illustrate, that the static pressure beneath the nose area is quite high. This will give a positive lift.

Drag

The drag and lift coefficient reported in Fig. 5.10 uses a default reference value of 1m^2 for Eq. (4.1). To get a representative drag value for the car, this area has to be changed.

The area is found with the projected area function for a front/rear view. This gives an area of 0.92m^2. The drag coefficient can then be found to be 0.53 for the current design.

The requirement for the drag was to be able to overcome it with 280bhp, at a speed of 280km hr^{-1}. The drag force therefore has to be converted into bhp. The power required to overcome the drag can be found with Eq. (5.9) [40].

$$P_o = \frac{\rho A C_D U^3}{2} \tag{5.9}$$

This result can then be converted from watts to bhp with the knowledge, that one bhp equals 745.7W [34].
The current design requires an effect of 139.95kW, which is equivalent to 187.68bhp.

Lift

The lift coefficients for Iteration 0 is found with a projected area for a top/bottom view. This gives an area of 4.03m^2, giving a lift coefficient of 0.27.
The lift force can then be found with Eq. (4.1) with the lift coefficient instead of the drag coefficient. This gives a lift force of 3966N.
The positive lift was expected at this stage from the information stated in Table 4.1. The closed wheel race car, used for reference, experiences a positive lift coefficient of 0.54 for the bodywork [32]. The reason is, that the distance the air has to travel above the car is greater than the distance below the car. This will accelerate the air flow on the top. Hence, the car will start working as an airfoil, and thereby generate lift. The acceleration over the top was also visible in Fig. 5.12.
The behavior of the front wing is illustrated in Fig. 5.14.

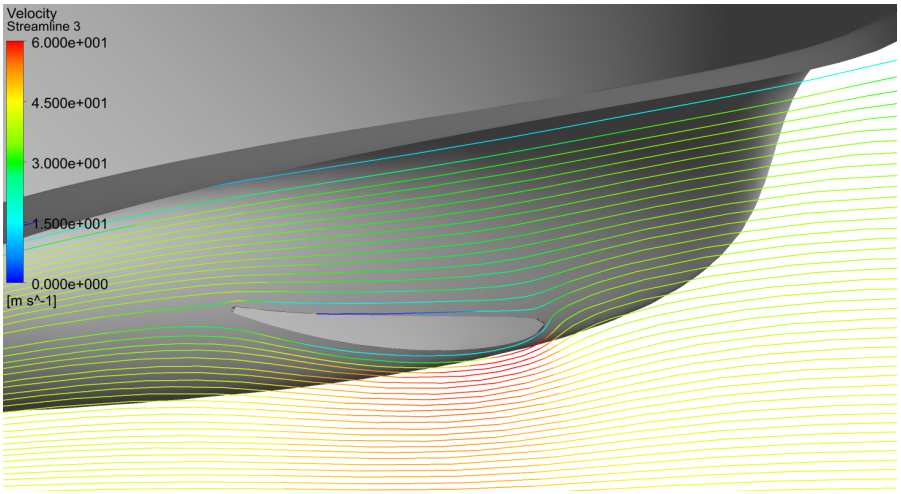

Figure 5.14: Velocity streamlines across the front wing airfoil.

The flow accelerates across the bottom part, thus generating of downforce of -254N. The location of the foil seems satisfactory, and the next step should be to increase the overall size.

The current force balance of the car is compared with the downforce requirement of -1200kgf. As stated in Sec. 4.2 this should be distributed as 40% in the front and 60% in rear of the car. The conversion from the force from Eq. (4.1) to kgf uses 9.80665N kgf^{-1} [34]. This gives 404.51kgf.
A comparison between the current and the required downforce is shown in Fig. 5.15.

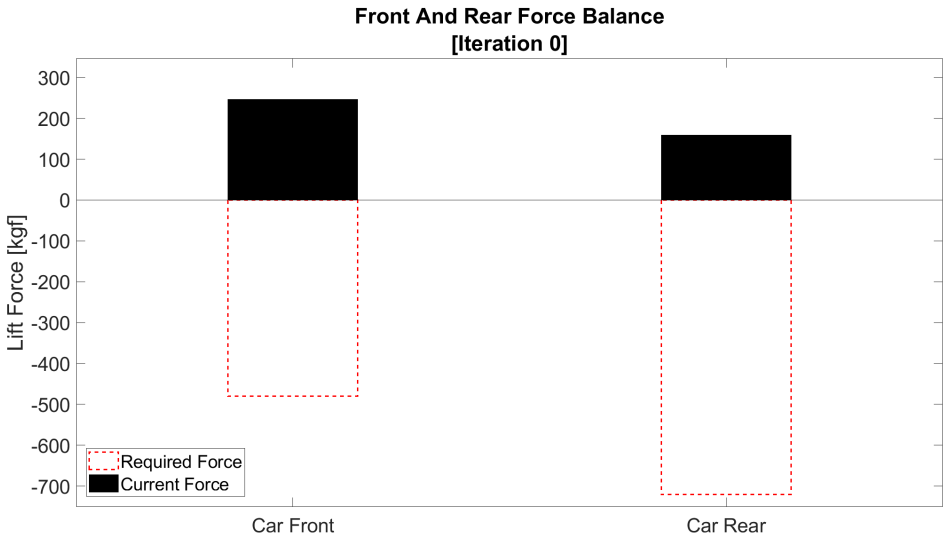

Figure 5.15: Front and rear force balance.

It can be seen, that the current design requires additional downforce generating components to achieve the target.
A current issue is also, that the air escapes out through the sides. The desired acceleration is therefore not achieved and downforce is not generated.

Iteration 0 Evaluation

The results from the Iteration 0 design indicate, that modifications are necessary in order to overcome the positive lift associated with the bodywork itself. The modifications are added from front to rear, as the front components will affect the rear components. The purpose here is to visualize the effects of the added components. Modifications to the bodywork are therefore kept to a minimum, and are left for the fluid topology optimization in Sec. 6 to deal with. This also means, that the nose will not be altered even though this currently presents a problem.
The main focus areas for the next iteration will therefore be limited to the front wing, and the problem associated with the air escaping from the underside of the car. The wake pattern of the car will be considered later, since the introduction of side vanes should alter the flow behavior upstream of the diffuser, and thereby also the behavior of the wake.

The lift and drag properties for the current design are presented below. Furthermore, the modifications to be made for the next iteration are summarized:

Lift and drag for Iteration 0

- Lift: 404.51kgf ($C_L = 0.27$, A = 4.03m^2)
- Drag: 187.68bhp ($C_D = 0.53$, A = 0.92m^2)

Design modifications for Iteration 1

- Increased airfoil size to generate more downforce in the front.
- Implementation of side vanes at the underside of the car in order to limit the amount of air escaping through the sides.

5.8.2. Iteration 1: Resizing of Front Wing and Inclusion of Side Vanes

For Iteration 1, the front wing size has been doubled. This is the largest size that is able to fit within the nose of the current bodywork. Though the new size required it to be relocated slightly. Furthermore, side vanes have been added to the underside of the car. The side vane height is limited to 20mm, based on the ride hide and maximum compression listed in Table 2.2.
The side vane design is illustrated in Fig. 5.16.

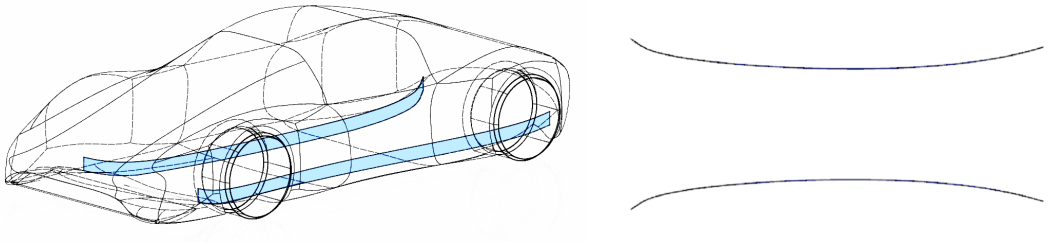

(a) Side vanes on the underside of the car.

(b) Side vanes' shape.

Figure 5.16

The vane shape pictured in Fig. 5.16b resembles a venturi pipe. By applying the venturi principle in this axis as well, it is possible to control where the throat of the undertray and diffuser is located. Due to the chassis this would not be possible if the venturi effect was only present between the undertray and ground.
The downforce produced by the front wing in Iteration 0 and 1 are listed in Table 5.3.

Table 5.3: Change in front wing downforce.

	Front Wing Downforce
Iteration 0	-25.9kgf
Iteration 1	-114.2kgf

Doubling the wing size and relocating it slightly has more than quadrupled the generated downforce.

The effect of the added side vanes are evaluated by investigating the amount of air escaping through the sides, as well as, the increased flow through the diffuser outlet.
The amount of escaping air is calculated from a surface plane between the front and rear wheels. The plane is positioned at the middle of the wheels.
The air flow through the diffuser is calculated at a surface plane normal to the flow direction, and positioned between the rear wheel and the symmetry plane. It is located at the middle of the wheel.
The difference in mass flow rate of the escaped air is shown in Table 5.4.

Table 5.4: Mass flow of air.

	Escaped Through Side	Diffuser
Iteration 0	0.31kg s^{-1}	2.35kg s^{-1}
Iteration 1	0.01kg s^{-1}	2.52kg s^{-1}

It is clear, that the problem with escaping air between the wheels has been almost completely eliminated. However, only 0.17kg s^{-1} of the decreased 0.31kg s^{-1} goes through the diffuser. The guide vanes do therefore not eliminate the air from escaping entirely in other places. For them to ensure this, they would have to seal the sides entirely, which is not possible.
The implementation of the side vanes increases the airflow going through the diffuser with 7.02%.

Iteration 1 Evaluation

The major modifications of the front part of the car bodykit is finalized at this point. This means, that attention should be given to the rear of the car for the next design iteration. As shown in Fig. 5.12, the diffuser creates an undesirable wake. This is most likely due to the diffuser expansion angle. This angle should therefore be adjusted with the inclusion of guiding vanes. The goal is to avoid separation, and expand to as close to free stream flow conditions as possible, in order to reduce drag.
Lastly, a rear wing should be implemented to increase the downforce. As explained in Sec. 4.2.3 this will use the SG6043 airfoil shape.

The lift and drag properties for the current design are presented below. Furthermore, the modifications to be made for the next iteration are summarized:

Lift and drag for Iteration 1

- Lift: 324.55kgf (C_L = 0.21, A = 4.03m^2)
- Drag: 179.57bhp (C_D = 0.52, A = 0.90m^2)

Design modifications for Iteration 2

- Adjustment of diffuser expansion angle with the inclusion of guiding vanes.
- Addition of a rear wing, using the SG6043 airfoil.

5.8.3. Iteration 2: Diffuser Adjustment and Addition of Rear Wing

The design concept for the rear wing is shown in Fig. 5.17, and the adjusted diffuser angle with guiding vanes can be seen in Fig. 5.17b.

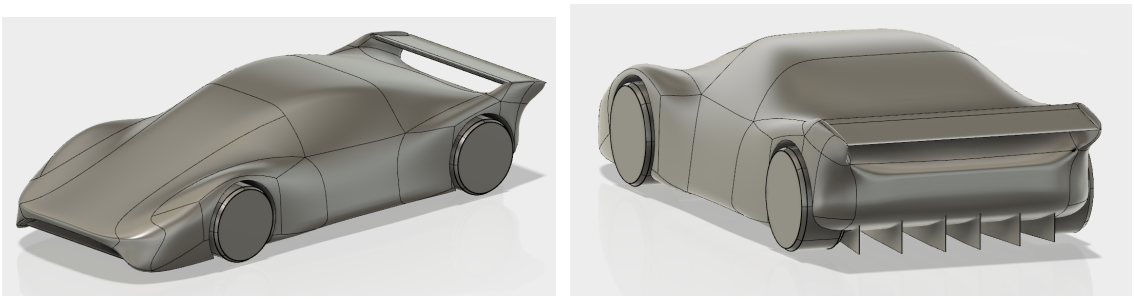

(a) (b)

Figure 5.17: Design after diffuser adjustment and the addition of a rear wing.

The result for the velocity magnitude streamlines across the body is shown in Fig. 5.18.

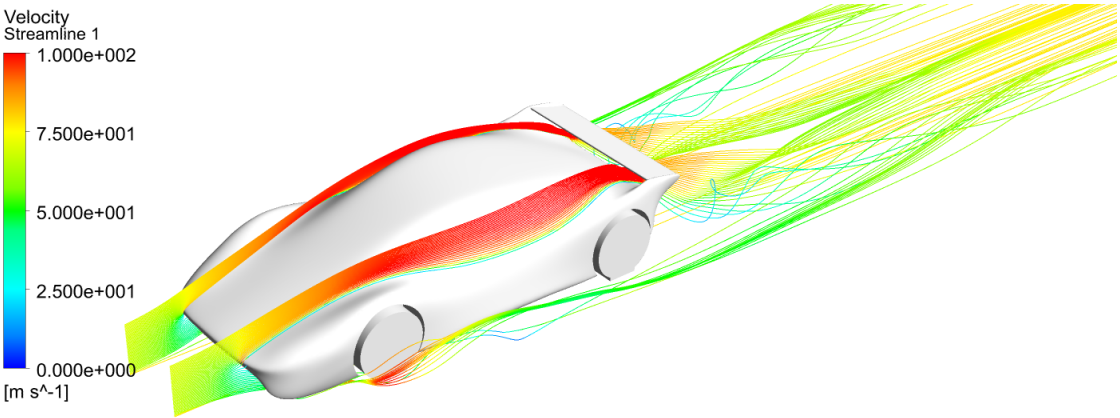

Figure 5.18: Velocity magnitude across the car.

The intensity of the large longitudinal vortices in the wake in Fig. 5.18 has been reduced compared to Iteration 0 (see Fig. 5.12).
This is also evident when directly comparing the streamlines from Iteration 0 and Iteration 2 in Fig. 5.19a and Fig. 5.19b, respectively. The kinetic energy is also lowered overall, as illustrated in Fig. 5.20. The vortices dissipate earlier in Iteration 2 than in Iteration 0. The introduction of larger counter rotating center vortices are one of the reasons for this.

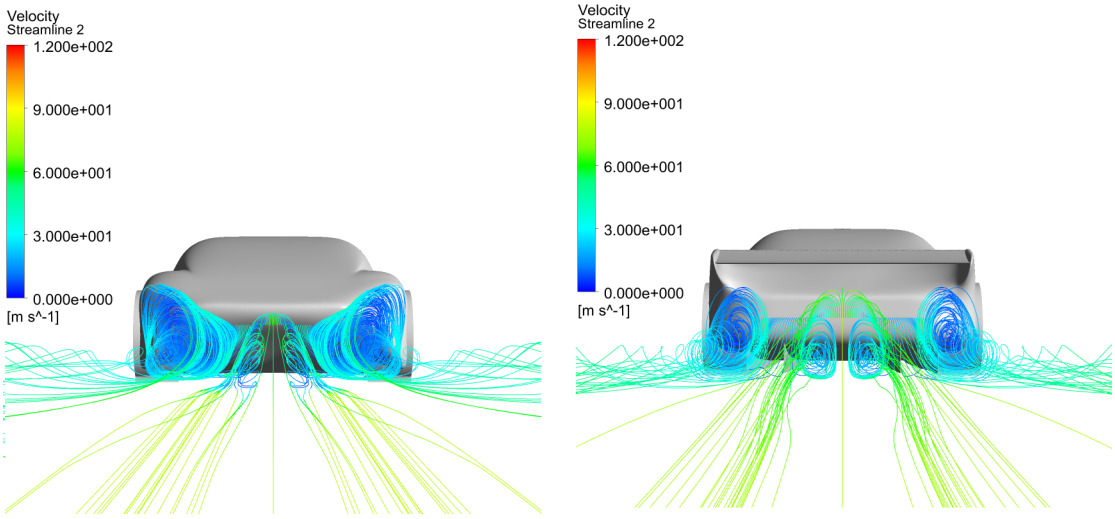

(a) Iteration 0. (b) Iteration 2.

Figure 5.19: Wake vorticity comparison.

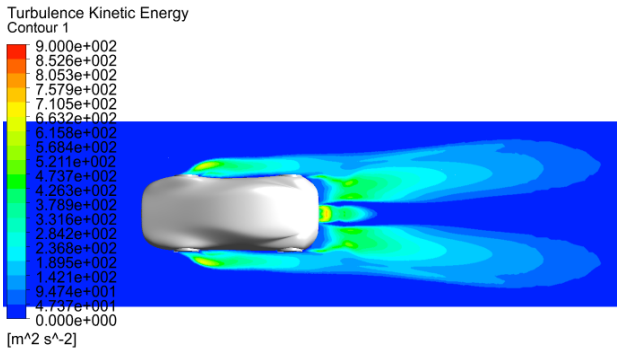

(a) Iteration 0.

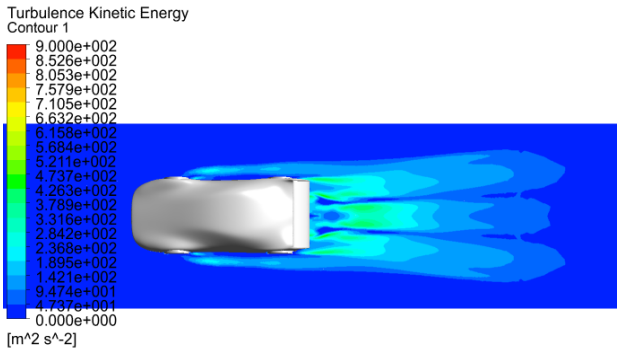

(b) Iteration 2.

Figure 5.20: Turbulent kinetic energy in the wake.

This has reduced the drag by 15.03% going from 0.53 to 0.46.
The rear wing generates -237.6kgf of downforce.
This corresponds to a lift coefficient for the wing of C_l = -1.81 for the projected area of A = 0.35m^2.

Iteration 2 Evaluation

Iteration 2 shows good improvements compared to the first two iterations of the design. However, even with these adjustment of the expansion angle of the diffuser, and the inclusion of a large rear wing, the car is still not achieving overall downforce.
The change in the magnitude of the lift force throughout the design stages so far is illustrated in Fig. 5.21.

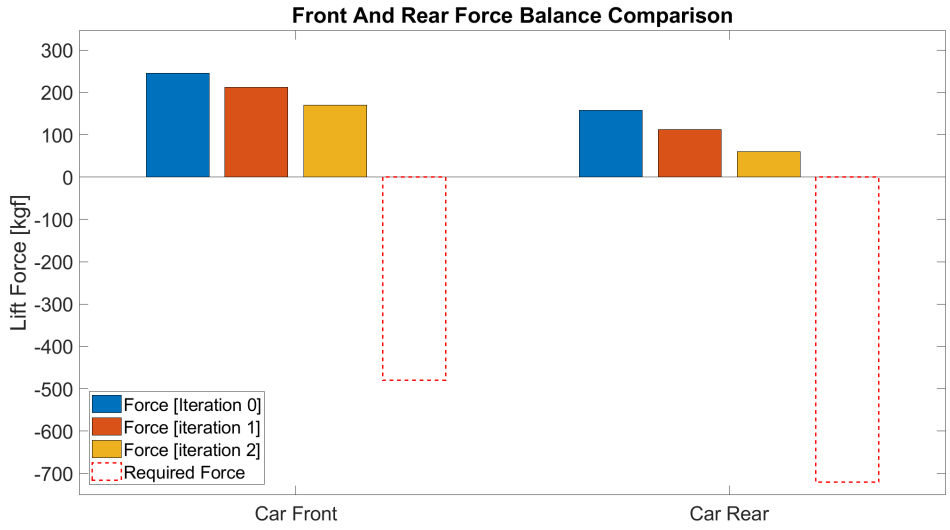

Figure 5.21: Lift force comparison between the iteration designs.

From a drag standpoint, the current design is very satisfactory, as the total drag force of 164.55bhp is well under the requirement of <280bhp. But, it is evident at this point, that the car will not achieve overall downforce without modifications to the bodywork itself. The body is currently too streamlined, and allows a large portion of air across the top. This accelerates the flow and makes the bodywork work as an airfoil.

The lift and drag properties for the current design are presented below:

Lift and drag for Iteration 2

- Lift: 230.53kgf (C_l = 0.15, A = 4.11m^2)
- Drag: 164.55bhp (C_D = 0.46, A = 0.92m^2)

The expected attached flow on the upper bodywork is achieved for all design iterations. This fits well with the used design guidelines listed in the summary in Sec. 4.7. However, the diffuser expansion angle was initially made too steep. This angle was therefore adjusted to avoid flow recirculation.
The initial front wing was under-dimensioned and it was therefore re-sized. As expected the car needed a rear wing as well. This was therefore fitted, and the angle of attack was adjusted based on the incoming air. The estimated lift coefficient for the rear airfoil is -1.8096. This is higher than the expected value of approximately -1.2 from Fig. 4.11. This indicates, that the flow around the airfoil is not sufficiently resolved. The value is over predicted, which is characteristic for too coarse meshes. The problem with the mesh resolution was also clear from drag forces in Fig. 5.6. This should therefore be kept in mind, when evaluating the lift and drag properties for the finalized design.
The rear lateral vortices were initially significant but this was corrected. This also decreased the drag significantly.

The design at this point has undergone the major changes. This means, that it is not expected, that entire components should be neither added nor removed. Hence, the bodywork's shape and the diffuser vanes are the last remaining parts to modify. The design should therefore be ready for the fluid topology optimization.

It should be recognized here, that several other major modifications such as e.g. louvres, dive plates, and cut-outs over wheels could be added (see Table 4.2). However, these add-ons are left for later studies, along with the different air intakes.

It should also be noted, that modifying the bodywork might not be sufficient to achieve the desired downforce. The downforce generation of the current design is very far from the specified target. Thus, it will not be considered a failure for the fluid topology optimization if it is not able to achieve the specified downforce. In such case, the constraints of the bodywork has to be discussed.

The expected bodywork modifications by the fluid topology optimization are listed below:

Expected areas affected by the fluid topology optimization

- Front leading edge height
- Hood shape
- Diffuser guiding vane shape
- Rear shape and height
- Rear wing supports

6. Fluid Topology Optimization

Fluid topology optimization is carried out using an adjoint method, which exist in both a continuous and a discrete version. Ansys Fluent uses the discrete adjoint method, as this offers greater stability compared to the continuous adjoint method [61]. Furthermore, the continuous adjoint equations are not unique and may change depending on subjective choices in their derivation [62]. The discrete adjoint method has a more systematic approach, which avoids such uncertainties.
Common for both adjoint methods is, that they are independent of the number of variables. Other possible approaches, for this type of optimization, are either finite differences or direct differentiation. However, these methods' computational costs will increase linearly with the number of design variables [63].

Several different studies were included in Sec. 3, each with a different number of so-called adjoint cases. Each iteration of geometry modifications through the adjoint method is commonly referred to as an adjoint case. This is done to distinguish them from the number of iterations used to converge to the adjoint solution.
The general approach and steps for an adjoint case is illustrated in the following flowchart:

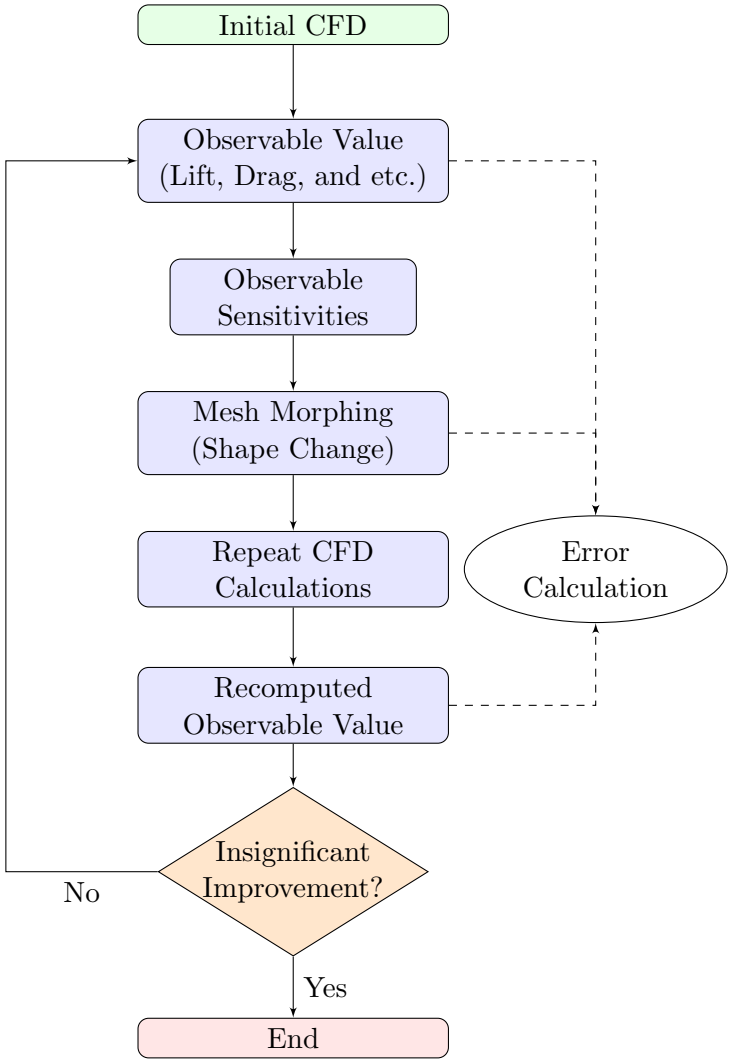

Each adjoint case requires the results from an initial CFD model. The observable of interest is then set. This could be e.g. the lift or the drag, which should be either maximized or minimized. The sensitivities can then be calculated with the adjoint solver. The sensitivities requires approximately the same computational effort as the initial CFD model.
When the model has converged, the user can seek an improvement in the mesh morphing tool. This can either be in total units (i.e. newtons for a force observable) or as a percentage. The mesh morpher will then modify the mesh to approach this improvement.
If the new geometry is satisfactory this can be used as the input for a new CFD model. The result from this might deviate slightly from the predicted change. This is due to the possible difference in calculation schemes between the flow solver and the adjoint solver. The error can be found as the difference between the predicted value, and the result obtained from the new geometry through the CFD model.
If the process shows significant change, the process is repeated for the new case. This can then be repeated until the change is deemed insignificant.

Neither of the investigated studies discuss the optimal number of adjoint cases required for their specific case. However, their cost function improvements show, that the first adjoint cases will have the largest effects. In the study by Montanelli (2013) [16], approximately 80% of the improvement was found within the first six adjoint cases. The study by Tzanakis (2014) [15] found almost 100% of the improvements within 11 adjoint cases for one of the investigated ducts. Another duct had almost 100% of the improvement within 19 adjoint cases. Frank et al. (2013) [13] used seven adjoint cases to find the final result. However, the plot of the cost function changes showed a possibility of further optimizing the geometry with additional adjoint cases.
As it can be seen, the optimal number of adjoint cases is highly dependent on the specific case. It should therefore be assessed simultaneously with the optimization process.

6.1. Discrete Adjoint Method

The aim of an optimization via the discrete adjoint method is to either minimize or maximize a given design parameter. The result is known as the optimal solution. The description of the discrete adjoint method is primarily based on the user and theory guides [61], while Duffy (2009) [62] and Faidon (2012) [63] have been used for clarifications of intermittent steps.
The general minimization problem can be formulated as:

$$\begin{aligned} \min \quad & J = J(u, \phi) \\ \text{subject to} \quad & N(u, \phi) = 0 \end{aligned} \tag{6.1}$$

This includes a cost function, $J = J(u, \phi)$, and a governing function, $N(u, \phi)$. Both of these functions include the state variable, u, and the design variable, ϕ. It is thereby desired to reduce the size of J, by altering ϕ to the most beneficial value. This should take the change in u into account. In this case ϕ is the shape of the bodywork, where a change will alter the aerodynamics of the car.

The method should assess where a change is most beneficial. Hence, where the smallest change has the largest effect. The derivative of the cost function, with respect to the design variable, is therefore the primary interest. This is derived from Eq. (6.1), applying the multivariable chain rule:

$$\frac{dJ}{d\phi} = \frac{\partial J}{\partial u}\frac{du}{d\phi} + \frac{\partial J}{\partial \phi} \tag{6.2}$$

This expression includes the sensitivity, $du/d\phi$. This can be found by calculating the derivative of the governing equation, from the minimization problem in Eq. (6.1). This is also differentiated with respect to ϕ, using the multivariable chain rule:

$$\frac{dN}{d\phi} = \frac{\partial N}{\partial u}\frac{du}{d\phi} + \frac{\partial N}{\partial \phi} = 0 \tag{6.3}$$

The sensitivity can then be found by rearranging Eq. (6.3):

$$\frac{du}{d\phi} = -\frac{\partial N}{\partial \phi}\left(\frac{\partial N}{\partial u}\right)^{-1} \tag{6.4}$$

Calculating Eq. (6.4) is the most time consuming part of the method known as Direct Differentiation. The sensitivities in Eq. (6.2) has to be calculated from Eq. (6.4) for all design variables. This in turn includes all state variables for each design variable. Thus, this step has to be refined in some way. This is the essence of the adjoint methods, as they reformulate this step into a system of adjoint equations.

The first step is to introduce the adjoint variables, λ, defined as:

$$\lambda = \left(\frac{\partial J}{\partial u} \left(\frac{\partial N}{\partial u} \right)^{-1} \right)^T \tag{6.5}$$

It is clear from this, that the adjoint variables reformulate all state variable dependent terms into a single term. T denotes a transposed matrix.
By introducing these variables, a direct relationship between the design variables and the cost function has been created. Thus, removing the state variables from the problem.
Finding these adjoint variables can be done with Eq. (6.6).

$$\left(\frac{\partial N}{\partial u} \right)^T \lambda = \left(\frac{\partial J}{\partial u} \right)^T \tag{6.6}$$

When this has been calculated, the gradient of the design parameter's effect on the cost function can be found as:

$$\frac{dJ}{d\phi} = \frac{\partial J}{\partial \phi} - \lambda^T \frac{\partial N}{\partial \phi} \tag{6.7}$$

When this equation has been calculated, it will be visible where changes to the design variable will have the greatest effect. It will also indicate whether material should be added or removed.

6.2. Cost Function Choice

As it was concluded in Sec. 5.8.3, that the downforce is insufficient at this point, this is chosen as the cost function. This is defined as an observable of the force type.
Ideally the cost function should be defined by the two forces; lift and drag. Then, in order to have a single cost function, the two forces should be combined to a ratio. This is of the operation type, with the lift observable as the numerator, and the drag observable as the denominator.
This approach should be adopted when the total lift of the car is negative.

6.3. Geometry Morphing

When the adjoint solution has been calculated, it is possible to specify a desired change in the cost function. Doing so will give a proposed new geometry of the body. This new geometry can then be used as the start of the next adjoint case. However, if the geometry morpher does not have any restrictions in this process, it is possible, that the new geometry cuts into the chassis. This can be avoided by introducing a bounded-by-surfaces constraint. It is therefore necessary to define an internal boundary, which limits the geometry change. This internal limit is illustrated in Fig. 6.1.

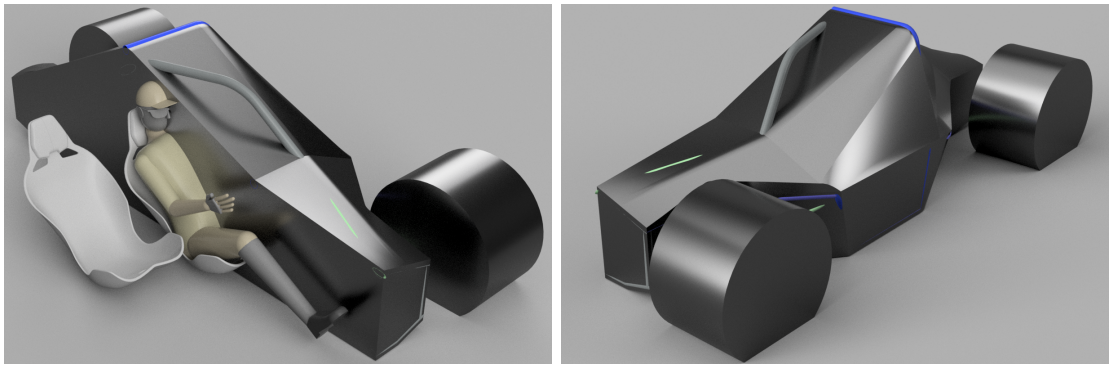

(a) (b)

Figure 6.1: Internal boundary for the adjoint geometry morphing.

The chassis used to create this inner boundary is a combination of the old and the new chassis (see Fig. 4.22). This is done to ensure, that the bodywork does not end up in the area, where the passengers' heads should be. It was chosen to omit a part of the upper roll cage from the new chassis from the internal boundary. This part of the chassis is still under consideration, and would put larger constraints on what can be modified on the top portion of the body.
The internal boundary also takes the wheels and wheel arches into account. These boundaries are flat in the bottom in order to fit with the external boundary.

The external boundary includes the ground clearance, and the maximum length and width of the car. This boundary is illustrated in Fig. 6.2.

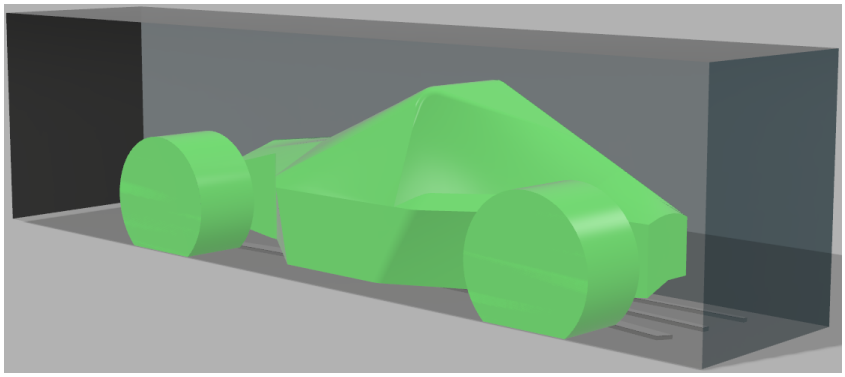

Figure 6.2: External boundary for ground clearance and maximum width and length.

The maximum width of the total car is 2m, while the maximum length is 5m. As there is no maximum height, this has been assumed to be 1.3m. The ground clearance is 50mm on most of the body. Small areas with a ground clearance of 30mm have been created around the diffuser side and guide vanes.

6.4. Mesh Preparation

The chosen mesh size in Sec. 5.7.2, is rather big for the adjoint method. Additionally, this mesh did not include an inflation layer. This means, that it is possible that separation and reattachment zones have not yet been identified. This was not a problem in Sec. 5.8.1 through 5.8.3, as these focused on the major components.
The mesh used for the preliminary iterations therefore has to be modified in order to work well with the adjoint method.

It was chosen to ensure, that the outer bounds of the wind tunnel was not too close. This concerns with the unknown sizes noted in Sec. 5.2 regarding the width and height of the tunnel. It was chosen to increase these values to 2.5 times the car length. The inner box dimensions were not altered. The increased number of cells is insignificant after this size increase, due to the large cell sizes in the outer parts.
As the fluid topology optimization is focused on the finer details of the bodywork, an inflation layer should be implemented. However, as noted in Sec. 5.7 the desired prism inflation layer makes the model unstable. An unstable flow model will make it impossible to achieve a converged adjoint solution. Hence, the desired inflation layer was not introduced. In place of this, a small box, just enclosing the car is introduced. The mesh within this box is then refined. Even though the cells are not aligned with the flow, the finer cells should still mean, that the flow is better resolved.
Adding this inflation box increases the total number of cells significantly (from 6.9 million to 30.1 million cells). It is therefore desired to find a method, which decreases it, without sacrificing too much precision. Such a method could be the conversion into polyhedrals. This decreases the cell count by 3-5 times [54].
The study by Frank et al. (2013) also uses this approach of converting the tetrahedral cells into polyhedrals [11, 13]. It is also stated, that a coarser mesh should have a stabilizing effect, and make it easier for the adjoint solution to achieve a converged result.

These three different changes to the mesh will each have an effect on the previously obtained lift and drag coefficients. In Fig. 6.3, the drag and lift coefficients are compared for the original mesh for Iteration 2 and the three changes.
From this it is clear, that the larger tunnel has a significant effect. The addition of the inflation box also has a small effect. Converting the tetrahedral mesh into polyhedrals decreases the drag coefficient slightly, while slightly increasing the lift coefficient.

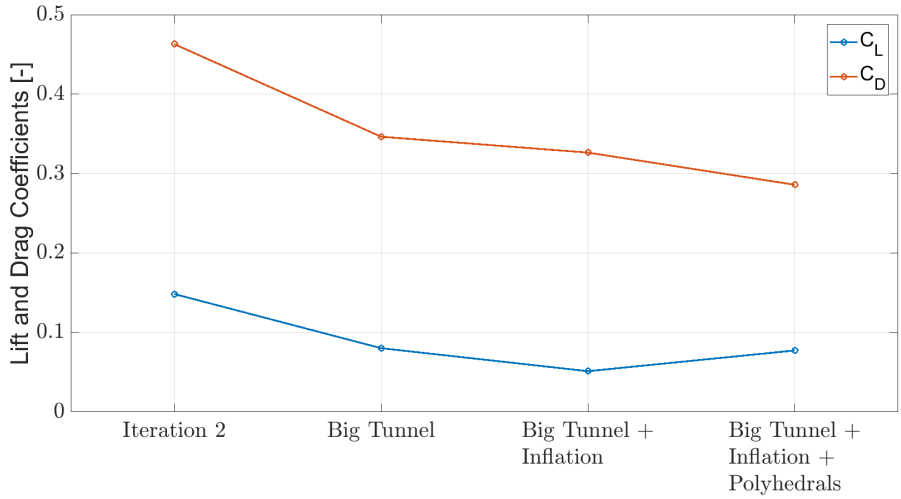

Figure 6.3: Change in lift and drag coefficients during the mesh development.

The new mesh can be seen in Fig. 6.4.

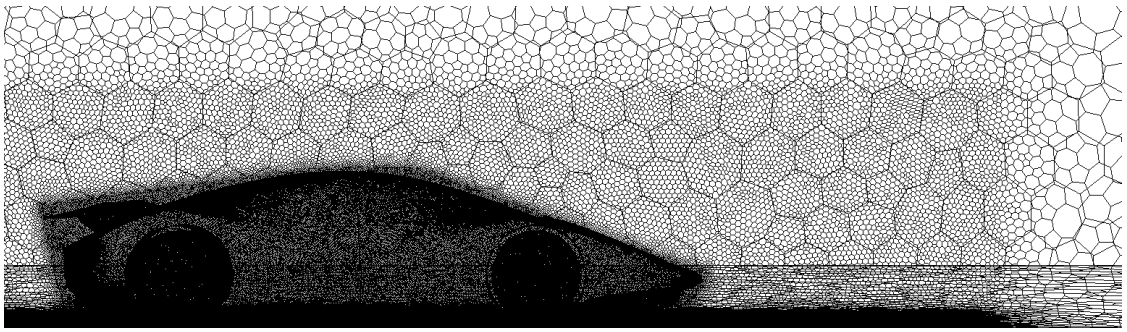

Figure 6.4: New mesh with inflation box and polyhedrals.

Fig. 6.4 both illustrates the small inflation box and the polyhedral mesh. The conversion from tetrahedrals to polyhedrals lowered the total cell count from around 30.1 million cells to 5.5 million cells. However, this mesh is not able to converge.

A lower cell count should make it possible to achieve a converged result [11]. The mesh was therefore coarsened down to the greatest size able to converge. This turned out to be a mesh with 8.4 million tetrahedral cells, reduced to 1.5 million polyhedral cells.

6.5. Adjoint Solver and Geometry Morphing Settings

The adjoint solver is decoupled from the choice of schemes for the flow solver. The settings for this solver therefore also has to be considered in order to achieve convergence. Additionally, the mesh morphing tool is a completely separate tool, which has its own settings. For the proposed geometry changes to have meaning, this also has to be controlled.

6.5.1. Adjoint Solver

Being a relatively new addition to the Ansys Fluent package, the adjoint solver has some restrictions in terms of the number of options. E.g., the pressure-velocity coupling only has the SIMPLE scheme available. The used schemes and methods for the adjoint solver are listed in Table 6.1.

Table 6.1: Computational scheme and methods for the adjoint solver.

Pressure-Velocity Coupling	
Scheme	SIMPLE
Spatial Discretization	
Pressure	PRESTO!
Momentum	Second Order Upwind

These settings are based on the recommendation, that they should match as closely to the flow case as possible, to get an accurate result.
Not using similar schemes for the adjoint solver might mean, that a small difference will appear. This means, that the expected change in the cost function after the mesh morphing might not be entirely correct.
Turbulence is not modeled, and the fluid topology optimization works with a frozen turbulence assumption. Therefore, such effects from possible changes are not taken into account when the sensitivities are calculated [61].

It was chosen to disable the solution-based controls initialization since this caused some instability. This initialization sets the advanced control parameters to values based on the initial state from the flow case. By disabling this, the algorithm starts with default values instead. It then gradually changes them according to the state of the adjoint solution as it goes through the iterations. This turned out to be a more stable approach for this case.
With complex geometries it is required to use a stabilization scheme to avoid divergence. The unsteadiness of the wake will also require stabilization. For this, the dissipation stabilization scheme was used with its default values. This is the available scheme with the lowest computational requirements [61]. It works by introducing a non-linear damping to the calculation domain. This tracks a marker, which is based on the adjoint solution state. If this marker's numerical value becomes large, damping is applied to the solution in the relevant regions.

6.5.2. Mesh Morphing

The default values for the mesh morphing did not give useable results. The morphing tool has settings for a constraint relaxation, a preconditioning, and a parameter relaxation. All three parameters can be varied between 0 and 1. The default values are 0.5. The default values ensure a balanced geometry change. A value of 0 for the preconditioning, and a value of 1 for the constraint relaxation will give the most aggressive morphing behavior.
The default values were not able to calculate a useable geometry change. The coefficients where therefore changed. The constraint and parameter relaxation were set to 0.05. The preconditioning was set to 0.95. This means, that the morphing behavior has been made less aggressive.

6.6. Adjoint Result

The fluid topology optimization on the design from Iteration 2 in Sec. 5.8.3 will be the adjoint case with the highest performance improvement. The improvement from the following adjoint cases will quickly decrease. This was seen in the studies by Montanelli (2013) [16], Tzanakis (2014) [15], and Frank et al. (2013) [13].
In order to achieve the correct adjoint solution, the adjoint solver has to converge. The convergence for the first adjoint case is illustrated in Fig. 6.5.

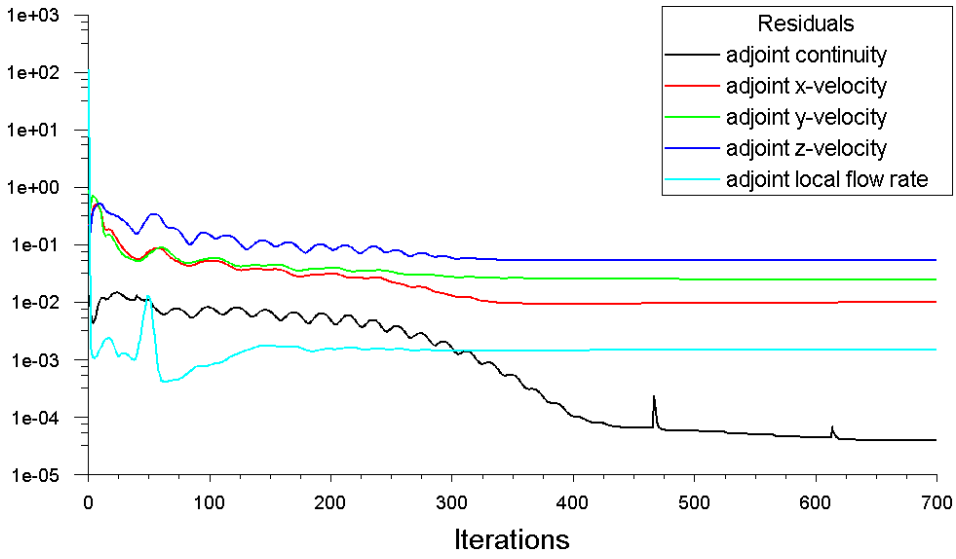

Figure 6.5: Convergence of adjoint solver.

When the adjoint solver has converged, it is possible to plot the sensitivities to the chosen cost function. The sensitivities are illustrated as normal optimal displacements, in Fig. 6.6. This shows where it would be beneficial to either add or remove material.

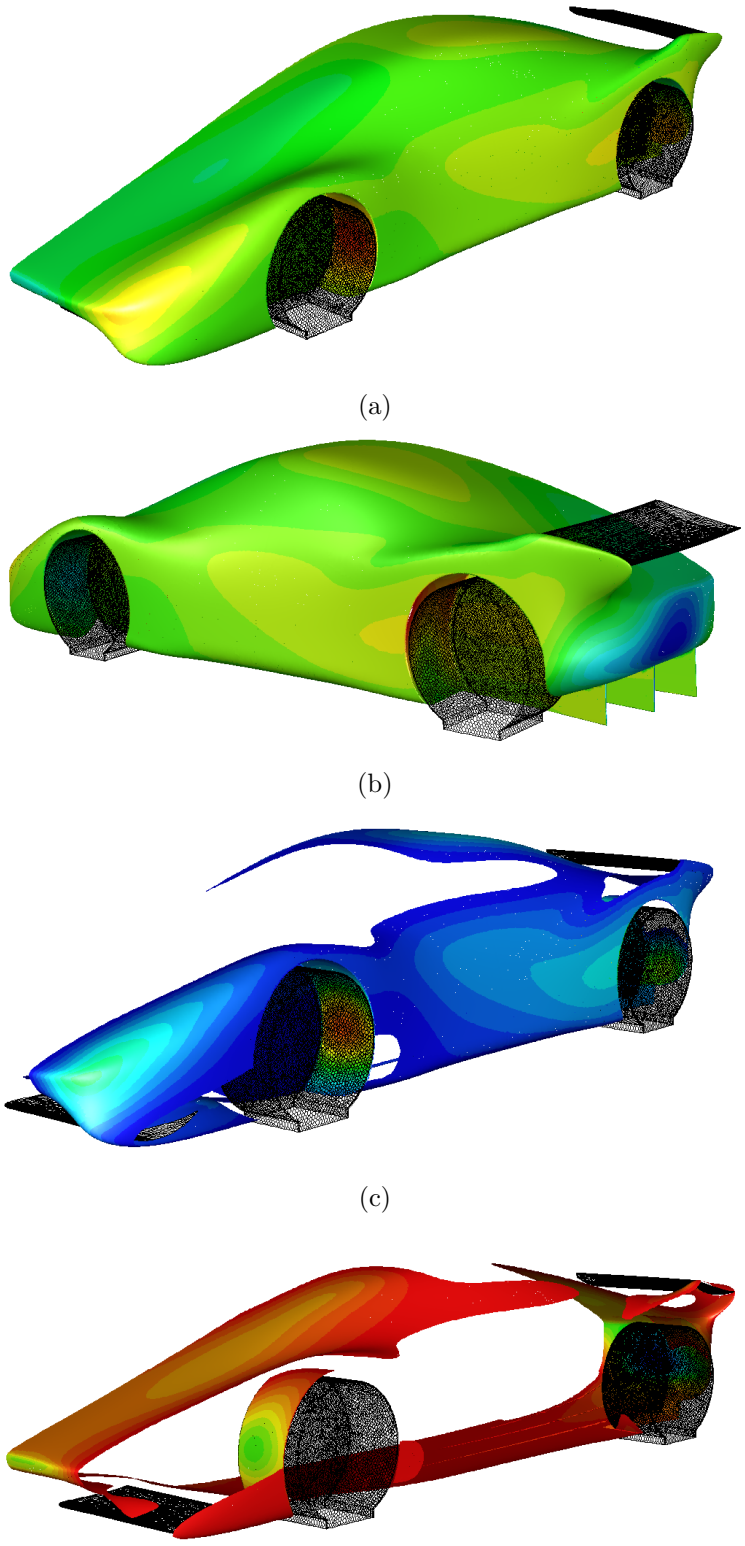

(a)

(b)

(c)

(d)

Figure 6.6: Normal optimal displacement.

The color scheme for Fig. 6.6 is RGB. Areas marked with the warm part of this spectrum will lead to improved performance by removing material. Areas marked with the cold part of this spectrum will lead to improved performance by adding material. This means, that the parts visible in Fig. 6.6c should have material added. The areas visible in Fig. 6.6d should have material removed.

As noted in Sec. 6.3, an unrestricted geometry morphing might cut into unwanted areas. The boundaries were therefore implemented in the manner described earlier. Fig. 6.7a illustrates the surface mesh view, when all boundaries have been included. Fig. 6.7b illustrates the direction of the internal surface constraints.

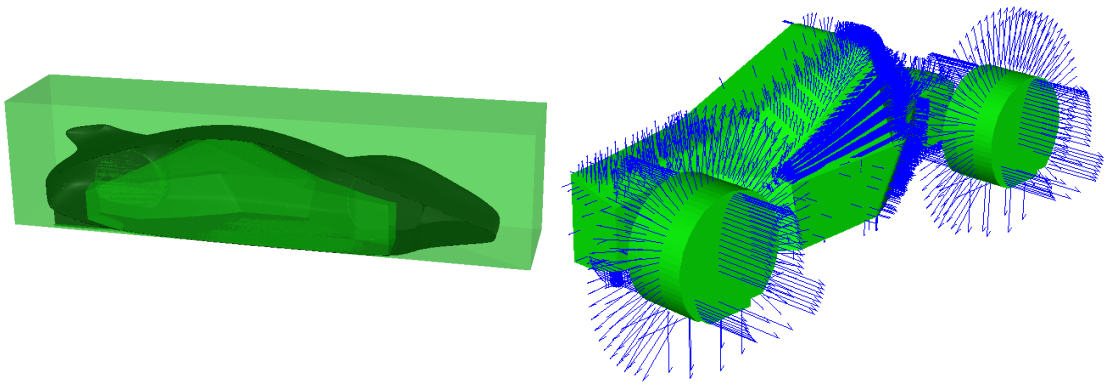

(a) Mesh morphing boundaries. (b) Internal surface constraints' directions.

Figure 6.7

The direction of the surface boundaries are outwards for the internal limit and the wheels. The external boundary should be directed inwards. This leaves an area in between, where the geometry morphing can take place.

The geometry morphing for the first adjoint case predicts a change of -521N for the positive lift on the bodywork. Both wings are excluded from the geometry morphing, as it was concluded that they might not be sufficiently resolved (see Sec. 5.9).
The geometry change is illustrated in Fig. 6.8.

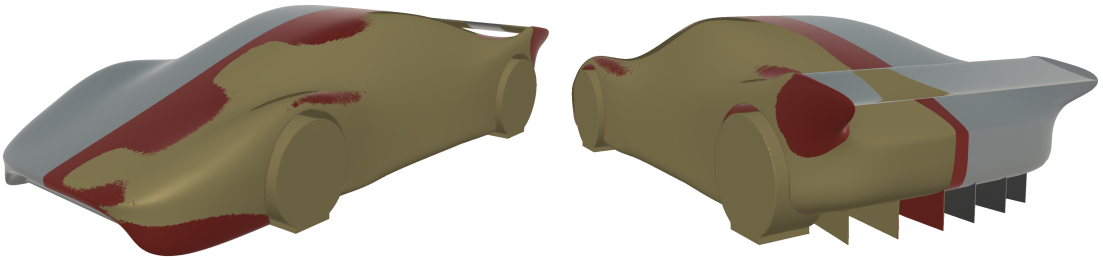

(a) (b)

Figure 6.8: Geometry change for the first adjoint case.

The red and gray areas in Fig. 6.8 shows the old geometry. This means, that areas in red has been morphed inwards. The left side of the old geometry has been colored red for better visualization. Comparing Fig. 6.8 with Fig. 6.6 it is also clear, that these were the areas most sensitive to a geometry change. The areas in brown have most likely had material added when comparing with Fig. 6.6c.

When the downforce for this new geometry is predicted by the flow solver, the change in total downforce amounts to -422N. This means, that the predicted change deviates with 19%.
It turns out, that almost the entire downforce improvement is found in the rear half of the body. The positive lift on this part is decreased from 2345N to 1805N. The geometry change causes the rear wing to lose some downforce. This has been changed from -2070N to -1931N. This shows, that the deviation of the predicted change might be due to the exclusion of the wings in this step.
Note, that the numbers for the performance of the Iteration 2 geometry has changed slightly (rear wing in Sec. 5.8.3 generated -2330N). This is due to the changed mesh and wind tunnel.

7. Final Aerodynamic Design

The fluid topology optimization via the discrete adjoint method included two adjoint cases. These two steps improved the downforce with a total of -67.84kgf. Simultaneously, the drag was improved by -44.07bhp, without including this in the cost function. The total expected change from the adjoint solver was -82.54kgf. The total deviation is thereby 17.81%.

The turbulent kinetic energy was also visibly decreased. This is illustrated in Fig. 7.1. By comparing with Fig. 5.20 it can be seen, that the wake is slightly less turbulent for the final design.

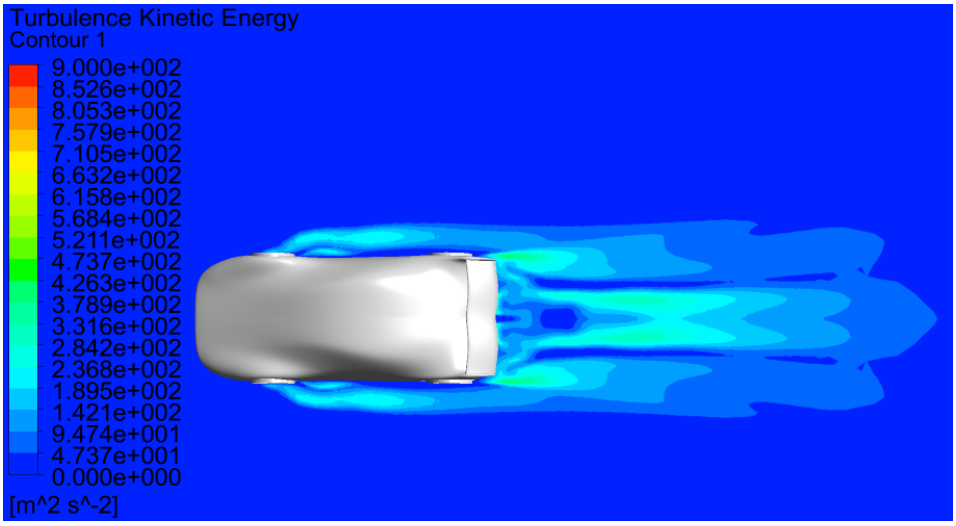

Figure 7.1: Turbulent kinetic energy for final design.

The geometry change from the initial design to the final design is illustrated in Fig. 7.2. The gray half represents the initial design, while the brown half illustrates the final design.

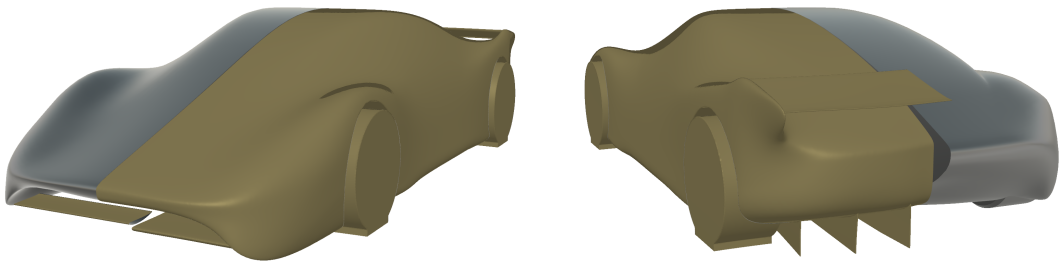

(a) (b)

Figure 7.2: Geometry change from initial design to final design.

Fig. 7.2a shows the bigger front wing. Additionally, it is clear from this, that it was necessary to lower its position slightly to fit. The bonnet modifications from the geometry morpher were presented in Fig. 6.8. These are not easily identified from Fig. 7.2a. This further underlines one of the great advantages with the adjoint optimization. I.e., its ability to make small effective geometry changes.
As clearly visible in Fig. 7.2b, the area in the rear has changed significantly. Both the addition of the rear wing and diffuser vanes adds to this. Additionally, the initial acute rear has been flattened.

The lift and drag improvements through the design process are listed in Table 7.1. The percentage improvements listed are based on the initial design.

Table 7.1: Lift and drag improvements.

	Lift	Lift Improvement	Drag	Drag Improvement
Initial design	404.51kgf	-	187.68bhp	-
Iteration 2	230.53kgf	-173.98kgf (43.01%)	164.55bhp	-23.13bhp (12.32%)
Final design	162.69kgf	-67.84kgf (16.77%)	120.48bhp	-44.07bhp (23.48%)

Most of the improvement for the lift was realized through the two manual iterations. This makes sense as the front wing was re-sized and the rear wing was added in these steps. However, it is interesting to see, that the total downforce improved a further 16.77%, just by making changes to the bodywork.
Even with the improvements in downforce, the final design is far from achieving the desired downforce of -1200kgf. If this value is to be achieved it requires changes to the constraints imposed on the bodywork design. This is both in terms of the undertray and diffuser design possibilities, as well as the drivers cabin. A chassis already at the minimum driving height leaves no possibility of designing the undertray. This was previously determined to be the single most downforce generating component. Hence, this is a great disadvantage. The diffuser would benefit from an earlier starting point. This would both give a better balance and a larger expansion. Furthermore, the three seater concept has the effect, that the cabin becomes wide. A more compact cabin would create less positive lift.

The drag force improved through the manual iterations. Though the change through the fluid topology optimization finds an even greater improvement. This improvement means, that the drag force can more than double, while still being below the required maximum. This will increase when cooling ducts, side view mirrors, suspension, rims, and etc. are added. If the current design was close to the drag limit, problems would most likely arise when these were added.

8. Discussion

The study demonstrates how a rough bodykit can be developed based on basic knowledge of car aerodynamics. Additionally, it shows the advantages of using CFD to further develop the design. This shows improvements in efficiency of the design in terms of both drag and lift. The study's findings confirm, that the discrete adjoint method can be used effectively to optimize the bodywork. The resultant shape optimization showed promising results. Furthermore, the performance improvements where found by altering the geometry in areas not directly obvious. The scale of several of these changes are small and would be difficult to perform manually. The performance improvements might become even greater if the geometry of the wings were allowed to change as well.
It was also discovered, that it was crucial to tune the mesh morphing settings to achieve meaningful geometry changes. Using the standard settings did not achieve any significant performance improvements. This might both be due to the complex geometry and the unsteadiness in the wake.
As expected, the expected performance change from the geometry morphing tool did not match with the following CFD model. This is most likely both due to the limited schemes available for the adjoint solver, and the frozen turbulence assumption.

The discrete method shows great potential for future iterations and investigations of the entire bodykit. The method is able to suggest a design change quickly. The resulting performance change is found in a much shorter time span, compared to the time it would take to achieve similar results through manual changes. Furthermore, CFD in general shows its value in the design phase. By using computer models it is possible to investigate several different designs before creating a scale model for wind tunnel tests.

All results of this study correlates well with prior studies by other authors. However, this study distinguishes itself by seeking a geometry change on almost the entire car. The investigated prior studies focus on fine details on specific parts of the geometries. E.g., the lower rear corner or the rear sill board. Furthermore, several studies concerns themselves with ducted flows.

The usefulness of the current bodywork is limited from a practical standpoint. This is mostly due to the missing considerations of inlets for cooling, and combustion engine air intake. Furthermore, components such as side view mirrors, area for the windscreen blades, and etc. are not included.
The final form was largely based on the restrictions caused by the chassis. This chassis was constructed before considering aerodynamics and introduced several difficulties. Hence, compromises had to be made to the design. Furthermore, the width caused by the three seats made it challenging to create an aesthetically pleasing design, while achieving the ambitious design specifications.

Further research on the subject should consider multiple observables simultaneously for the fluid topology optimization. This could include an optimization of the downforce, while decreasing the vorticity in the wake. Additionally, it could be sought to adjust the downforce balance in the front and rear by fluid topology optimization.

9. Conclusion

This study has presented methods for developing car aerodynamics, using computational fluid dynamics and the discrete adjoint method. The bodykit is based on initial requirements for an ambitious race car project. The approach has taken various important aerodynamic considerations and factors into account.

Improving vehicle aerodynamics using adjoint optimization, is not a novel idea. However, this study's considerations and development process creates a suiting reference for future design modifications. Furthermore, it shows the initial steps in designing the bodywork of a car. Prior studies most often deals with existing car designs.

The bodykit had a total improvement of 59.78% for the lift, and 35.80% for the drag throughout the design modifications.

The study's findings suggest, that optimizing with the discrete adjoint method has the potential of significantly improving aerodynamic performance. Though, not achieving the desired design specifications for this particular case. Further improvement will require modifications to the existing chassis design and the constraints imposed by this. This includes the width of the current passenger safety frame. Additionally, changes to the underside would be beneficial, to give more freedom to develop the undertray and diffuser.

It is concluded, that performance improvements can be found with great time savings compared to manual modifications by performing fluid topology optimization with the discrete adjoint method.

References

[1] DIS Race Lab. *Personal communication.* 2018.

[2] Guinness World Records. www.guinnessworldrecords.com/world-records/fastest-0-100-kmh-acceleration-electric-car (cited 08.02.2018).

[3] Road and Track. www.roadandtrack.com/car-culture/g6413/nurburgring-lap-records/ (cited 08.02.2018).

[4] BBC Worldwide Ltd. www.topgear.com/show/lap-times (cited 08.02.2018).

[5] The Study Board of Energy. Curriculum for the Master of Science Programme in Sustainable Energy Engineering. www.ses.aau.dk/digitalAssets/275/275544_cand_polyt_sustainable_energy_engineering_esbjerg_2017_ver1_final.pdf (online, cited 05.02.2018).

[6] DIS. d-i-s.net (cited 05.02.2018).

[7] CarBuzz Inc. The Aston Martin Valkyrie Will Spawn A New Range Of "Incredible" Cars. carbuzz.com/news/the-aston-martin-valkyrie-will-spawn-a-new-range-of-incredible-cars (cited 15.02.2018).

[8] Audi AG. www.audi.com/de/innovation/futuredrive/electric_motors.html (cited 15.02.2018).

[9] J. Katz. *Race Car Aerodynamics: Designing for Speed.* Bentley publishers, 1995.

[10] W. H. Hucho. *Aerodynamics of Road Vehicles: From Fluid Mechanics to Vehicle Engineering.* Elsevier, 2013.

[11] Ansys Inc. *White Paper: Shape Optimization for Aerodynamic Efficiency Using Adjoint Methods.* 2016.

[12] G. K. Karpouzas, E. M. Papoutsis-Kiachagias, T. Schumacher, E. de Villiers, K. C. Giannakoglou, and C. Othmer. *Adjoint Optimization for Vehicle External Aerodynamics.* International Journal of Automotive Engineering, vol. 7, pp. 1-7, 2016.

[13] T. Frank, B. Gerlicher, and J. Abanto. *DrivAer-Aerodynamic Investigations for a New Realistic Generic Car Model using Ansys CFD.* Conference paper, Automotive Simulation World Congress, 2013.

[14] C. Othmer. *Adjoint Methods for Car Aerodynamics.* Journal of Mathematics in Industry, vol. 4, 2014.

[15] A. Tzanakis. *Duct Optimization Using CFD Software 'Ansys Fluent Adjoint Solver'.* M.Sc. Thesis, Chalmers University of Technology, 2014.

[16] H. Montanelli. *Multipoint Shape Optimization With Discrete Adjoint Method for the Design of Turbomachine Blades.* M.Sc. Thesis, CERFACS, 2013.

[17] BBC Worldwide Ltd. www.topgear.com/car-news/supercars/road-trip-across-europe-903bhp-mclaren-p1 (cited 07.05.2018).

[18] BBC Worldwide Ltd. www.topgear.com/car-reviews/mclaren/2dr-auto/first-drive-0 (cited 07.05.2018).

[19] BBC Worldwide Ltd. www.topgear.com/car-reviews/radical/37-2dr/road-test (cited 07.05.2018).

[20] BBC Worldwide Ltd. www.topgear.com/car-news/supercars/brabham-bt62-ps12m-700bhp-track-only-supercar (cited 07.05.2018).

[21] Techeblog. http://www.techeblog.com/index.php/tech-gadget/apollo-intensa-emozione-gets-tested-on-the-track-is-a-real-life-batmobile (cited 08.05.2018).

[22] TopSpeed. www.topspeed.com/cars/others/2019-nio-ep9-ar177837.html (cited 07.05.2018).

[23] Road and Track. www.roadandtrack.com/new-cars/car-technology/a12499392/why-porsche-911-gt2-rs-is-so-fast-at-nurburgring/ (cited 07.05.2018).

[24] Digital Trends. www.digitaltrends.com/cars/pagani-huayra-bc-supercar/ (cited 07.05.2018).

[25] Auto Blog. www.autoblog.com/2011/01/25/pagani-huayra-makes-its-official-web-debut/?guccounter=1 (cited 07.05.2018).

[26] BBC Worldwide Ltd. www.topgear.com/car-news/supercars/evil-apollo-intensa-emozione-testing-public-roads-0 (cited 07.05.2018).

[27] Digital Trends. www.digitaltrends.com/cars/apollo-intensa-emozione/ (cited 07.05.2018).

[28] Road and Track. www.roadandtrack.com/new-cars/future-cars/news/a31192/the-am-rb-001-hypercar-generates-4000-pounds/ (cited 07.05.2018).

[29] F. Puhn. *How to Make Your Car Handle*. Penguin, 1976.

[30] R. A. Serway and J.W. Jewett. *Principles of Physics: A Calculus-Based Text*. Cengage Learning, 2012.

[31] W. F. Milliken and D. L. Milliken. *Race Car Vehicle Dynamics*. SAE International, 1995.

[32] J. Katz. *Automotive Aerodynamics*. Wiley, 2016.

[33] W. Toet. What Parts of a Formula 1 Car Generates the Main Aerodynamic Forces? www.linkedin.com/in/willemtoet1/ (cited 26.02.2018).

[34] Y. A. Çengel, J. M. Cimbala, and R. H. Turner. *Fundamentals of Thermal-Fluid Sciences*. McGraw-Hill, 4th ed., 2012.

[35] G. Mastinu and M. Ploechl. *Road and Off-Road Vehicle System Dynamics Handbook*. CRC press, 2014.

[36] M. O. L. Hansen. *Aerodynamics of Wind Turbines*. Routledge, 3rd ed., 2015.

[37] M. S. Selig, J. J. Guglielmo, A. P. Broeren, and P. Giguére. *Summary of Low-Speed Airfoil Data, Volume 1*. SoarTech Publications, 1995.

[38] M. S. Selig, C. A. Lyon, P. Giguere, C. Ninham, and J. J. Guglielmo. *Summary of Low-Speed Airfoil Data, Volume 2*. SoarTech Puplications, 1996.

[39] M. S. Selig, A. P. Broeren, P. Giguere, A. Gopalarathnam, and C. A. Lyon. *Summary of Low-Speed Airfoil Data, Volume 3*. SoarTech Puplications, 1997.

[40] B. R. Munson, T. H. Okiishi, W. W. Huebsch, and A. P. Rothmayer. *Fluid Mechanics*. Wiley, 7th ed., 2013.

[41] A. E. Senior and X. Zhang. *The Force and Pressure of a Diffuser-Equipped Bluff Body in Ground Effect*. Journal of Fluids Engineering, vol. 123(1), pp. 105-111, 2001.

[42] GrabCAD. grabcad.com/library/ahmed-body-4 (cited 21.02.2018).

[43] X. Zhang, W. Toet, and J. Zerihan. *Ground Effect Aerodynamics of Race Cars*. Applied Mechanics Reviews, vol. 59, pp. 33-49, 2006.

[44] S. Discetti and A. Ianiro. *Experimental Aerodynamics*. CRC Press, 2017.

[45] A. K. Saha, D. Das, R. Srivastava, P. K. Panigrahi, and K. Muralidhar. *Fluid Mechanics and Fluid Power Contemporary Research*. Springer, 2016.

[46] W. Toet. Race Tech Motorsport Engineering. Willem Toet Explains - Motorsport Diffusers. www.racetechmag.com/2017/08/willem-toet-explains-motorsport-diffusers/ (cited 23.02.2018).

[47] X. Zhang, A. Senior, and A. Ruhrmann. *Vortices Behind a Bluff Body With an Aft Section in Ground Effect*. International Journal of Heat and Fluid Flow, vol. 25, pp. 1-9, 2004.

[48] A. Ruhrmann and X. Zhang. *Influence of Diffuser Angle on a Bluff Body in Ground Effect*. Journal of Fluid Engineering, vol. 125, pp. 1-7, 2003.

[49] W. Toet. Race Tech Motorsport Engineering. Willem Toet Explains - Air Ducts. www.racetechmag.com/2017/08/willem-toet-explains-air-ducts/ (cited 23.02.2018).

[50] L. Jowsey and M. Passmore. *Experimental Study of Multiple-Channel Automotive Underbody Diffusers.* Journal of Automobile Engineering, vol. 224, pp. 865-879, 2009.

[51] Mocal. Oil Coolers. www.mocal.co.uk/products-oilcoolers.html (cited 16.03.2018).

[52] Wilwood. Disc Rotors ultralite 32 series. http://www.wilwood.com/Rotors/RotorProd.aspx?itemno=160-0471 (cited 30.04.2018).

[53] S. R. Turns. *An Introduction to Combustion - Concepts and Applications.* McGraw Hill, 3rd ed., 2012.

[54] Ansys Inc. *Ansys Fluent User Guide and Ansys Fluent Theory Guide v. 19.0.* Ansys inc., 2018.

[55] M. Lanfrit. *Best Practice Guidelines for Handling Automotive External Aerodynamics with FLUENT.* Fluent Deutschland GmbH, v. 1.2, 2005.

[56] C. Rasiraghi. *Race Car Aerodynamics.* Guest lecture, KTH - Royal Institute of Technology, 2010.

[57] N. E. Ahmad, E. Abo-Serie, and A. Gaylard. *Mesh Optimization for Ground Vehicle Aerodynamics.* Mechanical and Automotive Engineering Department. Coventry University, UK, pp. 54-65, 2010.

[58] S. Bordei and F. Popescu. *Aerodynamic Results For a Notchback Race Car.* University of Galati, 2011, pp. 159-178.

[59] European Research Community on Flow, Turbulence, and Combustion. *Special Interest Group on "Quality and Trust in Industial CFD" Best Practice Guidelines.* ERCOFTAC, v. 1.0, 2000.

[60] Y. A. Çengel and J. M. Cimbala. *Fluid Mechanics: Fundamentals and Applications Chapter 15: Introduction To Computational Fluid Dynamics.* McGraw-Hill, 2006.

[61] Ansys Inc. *Ansys Fluent Advanced Add-On Modules v. 18.0.* Ansys Inc., 2017.

[62] A. C. Duffy. *An Introduction to Gradient Computation by the Discrete Adjoint Method.* Florida State University, 2009.

[63] F. Christakopoulos. *Sensitivity Computation and Shape Optimisation in Aerodynamics Using Adjoint Methodology and Automatic Differentiation.* Doctoral dissertation, Queen Mary University of London, 2012.

Appendix

A. Included Airfoils

The airfoils evaluated for the front and rear wing are listed in Table A.1.

Table A.1: Airfoils included in evaluation.

Name	Reynolds number	Source
Avistar	400,000	[39]
BW-3	400,000	[39]
CG Ultimate	500,000	[39]
Clark-Y (B)	400,000	[39]
DH4009	500,000	[39]
E231	400,000	[39]
E387 (C)	460,000	[39]
E472	500,000	[39]
ESA	400,000	[39]
Falcon 56 Mk II	400,000	[39]
Goe 417a	400,000	[39]
PT-40 (A)	400,000	[39]
S8036	500,000	[39]
S8037	500,000	[39]
S8052	500,000	[39]
S823	400,000	[37]
SD7062 (B)	400,000	[39]
SG6040	500,000	[39]
SG6041	500,000	[39]
SG6043	500,000	[39]
Trainer 60	500,000	[39]
Ultra-Sport 1000	500,000	[39]
USNPS-4	400,000	[39]

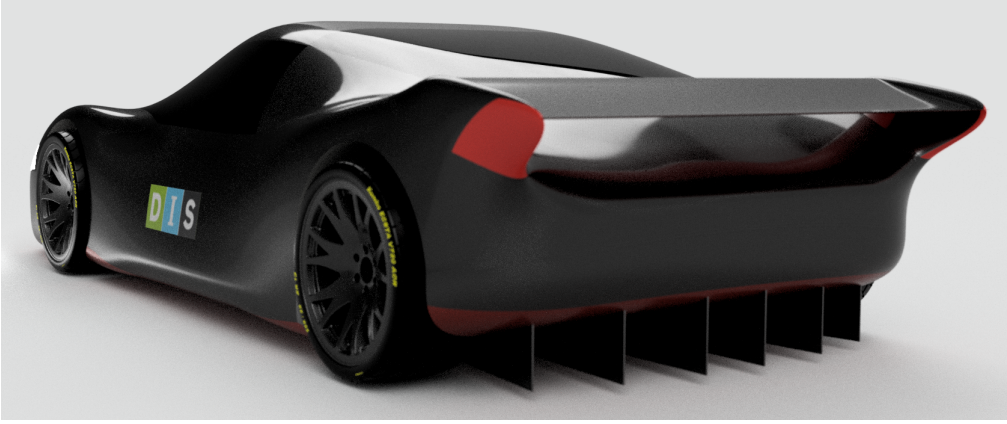

AALBORG UNIVERSITY
STUDENT REPORT

innovative engineering